



**CHARACTERIZING OPTICAL LOSS IN ORIENTATION PATTERNED III-V  
MATERIALS USING LASER CALORIMETRY**

THESIS

Dushyant A. Sadhwani, Lieutenant, USAF

AFIT-ENP-14-M-32

**DEPARTMENT OF THE AIR FORCE  
AIR UNIVERSITY**

**AIR FORCE INSTITUTE OF TECHNOLOGY**

---

---

**Wright-Patterson Air Force Base, Ohio**

**DISTRIBUTION STATEMENT A:**  
APPROVED FOR PUBLIC RELEASE; DISTRIBUTION UNLIMITED.

The views expressed in this thesis are those of the author and do not reflect the official policy or position of the United States Air Force, Department of Defense, or the United States Government. This material is declared a work of the U.S. Government and is not subject to copyright protection in the United States.

**CHARACTERIZING OPTICAL LOSS IN ORIENTATION PATTERNED III-V  
MATERIALS USING LASER CALORIMETRY**

**THESIS**

Presented to the Faculty

Department of Engineering Physics

Graduate School of Engineering and Management

Air Force Institute of Technology

Air University

Air Education and Training Command

In Partial Fulfillment of the Requirements for the

Degree of Master of Science in Applied Physics

Dushyant A. Sadhwani, BS

Second Lieutenant, USAF

March 2014

**DISTRIBUTION STATEMENT A.**

APPROVED FOR PUBLIC RELEASE; DISTRIBUTION UNLIMITED.

CHARACTERIZING OPTICAL LOSS IN ORIENTATION PATTERNED III-V  
MATERIALS USING LASER CALORIMETRY

Dushyant A. Sadhwani, BS

Second Lieutenant, USAF

Approved:

//signed//

\_\_\_\_\_  
Timothy Zens, Maj, USAF, PhD (Chairman)

\_\_\_\_\_  
Date

//signed//

\_\_\_\_\_  
Rita Peterson, PhD, AFRL (Member)

\_\_\_\_\_  
Date

//signed//

\_\_\_\_\_  
Michael Snure, PhD, AFRL (Member)

\_\_\_\_\_  
Date

//signed//

\_\_\_\_\_  
Michael Marciniak, PhD (Member)

\_\_\_\_\_  
Date

### **Abstract**

Several Air Force applications call for tunable laser sources in the mid-infrared (MIR) spectral range. Existing lasers with output in the near-infrared can be converted to more desirable MIR using nonlinear effects. Orientation patterned III-V materials like Gallium Arsenide (GaAs) and Gallium Phosphide (GaP) are promising nonlinear frequency conversion materials that can be used in high power, tunable laser sources in the MIR range for numerous Air Force applications. This research examines the optical loss in such orientation patterned III-V materials. Laser calorimetry technique was assembled to measure the absorption loss in GaAs, GaP and  $\text{Fe}^{2+}\text{ZnSe}$  samples. Three different methods are explained and utilized to calculate the absorptance value from the calorimetry data. Absorption coefficient values were found for three different samples of GaAs ranging from  $0.025 \pm 0.009 \text{ cm}^{-1}$  to  $0.80 \pm 0.08 \text{ cm}^{-1}$ , all within the sphere of published values for GaAs. A Complete Angle Scatter Instrument (CASI) was used to determine scatter at incident angles ranging from 0 to 55.5 degrees from two OPGaAs samples using an  $8.16 \text{ }\mu\text{m}$ , p-polarized incident laser light. Diffraction peaks were observed in the samples with high impurities, with domains in the material acting as diffraction gratings. FTIR measurements were conducted using a wire grid polarizer on the CASI samples to investigate transmission signal variations with change in incident polarization. Both patterned GaAs samples exhibited some polarization effect from the grating material. The amount of transmission detected varied by as much as 20% for both samples as they were rotated to change incident polarization.

## **Acknowledgments**

I would like to express my sincere appreciation to my faculty advisor, Maj. Zens, for his guidance and support throughout the course of this thesis effort. The insight and experience was certainly appreciated. I would, also, like to thank my committee members, Dr. Peterson, Dr. Snure and Dr. Marciniak, for helping me grasp the theoretical and experimental fundamentals needed in completing this thesis. I would also like to thank Dr. Nauyoks for assisting in collecting the CASI measurements. Applied Physics Department technicians, Gregory Smith and Michael Ranft helped immensely in setting up the FTIR experiments and devoting their time to make sure I had all the tools to successfully conduct the experiment. Finally, I would like to acknowledge the support my family has provided throughout my time here at AFIT. This thesis could not have been possible without their patience and confidence in me.

Dushyant A. Sadhwani

## Table of Contents

	Page
Abstract .....	iv
Table of Contents .....	vi
List of Figures .....	viii
List of Tables .....	xiv
 I. Introduction .....	 1
Motivation .....	1
Problem Statement .....	3
Research Scope .....	6
Overview .....	10
 II. Literature Review .....	 11
Nonlinear Processes .....	11
<i>Optical Parametric Oscillator</i> .....	12
Quasi-Phase Matching .....	16
Fabrication of III-V materials like GaAs .....	19
Laser Calorimetry Theory .....	22
Scattering Theory .....	25
<i>Rayleigh Theory</i> .....	26
<i>Diffraction</i> .....	28
 III. Methodology .....	 30
OPGaAs Samples .....	30
Laser Calorimetry Experiment .....	32
CASI Measurements .....	44
FTIR Measurements .....	46
Summary .....	48
 IV. Results and Analysis .....	 49
Chapter Overview .....	49
Laser Calorimetry .....	49
CASI .....	60
FTIR .....	72
Summary .....	78

	Page
V. Conclusions and Recommendations .....	79
Chapter Overview .....	79
Conclusions of Research .....	79
Recommendations for Action and Future Research.....	80
<i>Accounting for Surface Absorption:</i> .....	80
<i>Adopting a Different Wavelength</i> .....	80
<i>Diffraction from Sample Edge</i> .....	81
<i>Photothermal Deflection Technique</i> .....	81
Summary .....	82
Appendix A.....	83
Appendix B .....	92
Laser Calorimetry Experimental Setup Instructions (Do's and Don'ts) .....	92
<i>Minimizing Noise</i> .....	94
<i>Thermal Camera Images for a Different Sample Holder Configuration</i> .....	94
References.....	97



## List of Figures

	Page
Figure 1: Atmospheric transmittance windows of Air Force Interest.....	2
Figure 2: Transmission spectra comparison between LiNbO <sub>3</sub> and GaAs.....	6
Figure 3: Relationship between difference frequency generation and optical parametric oscillation.....	13
Figure 4: The gain associated with the process of optical parametric amplification gain used to construct the optical parametric oscillator (OPO).....	14
Figure 5: Comparison of the conversion efficiencies for different phase matching conditions.....	17
Figure 6: Sellmeier equation for GaAs..	18
Figure 7: Signal and Idler wavelengths from a GaAs OPO tuning curve.....	18
Figure 8: Modulation of the nonlinear coefficient to achieve QPM.using wafer bonding .....	20
Figure 9: OPGaAs growth process to produce modulation of the nonlinear coefficient to achieve QPM. ....	21
Figure 10: OPGaAs growth process..	21
Figure 11: Sample plot of calorimetry data set using a GaAs wafer. ....	23
Figure 12: Scattering of incident light from small particles. ....	26
Figure 13: OPGaAs samples observed under a Nikon Nomarski microscope..	31
Figure 14: Setup of incident laser source for calorimetry.....	32
Figure 15: Sample mount used for calorimetry experiment..	34
Figure 16: Styrofoam box enclosure used in calorimetry for better insulation. ....	35

	Page
Figure 17: Proof of thermal insulation provided by the Styrofoam box.....	35
Figure 18: ExcellINX computer software layout; used to record calorimetry data.....	36
Figure 19: Optics used in calorimetry experiment.....	37
Figure 20: Complete laser calorimetry setup. ....	38
Figure 21: A representative plot from the laser calorimetry experiment.....	39
Figure 22: Pre-measurement temperature normalization plot of the interior of Styrofoam box. ....	40
Figure 23: Initial stable temperature curves as a result of normalization wait time. ....	40
Figure 24: Gradient method technique to recover absorptance from calorimetry data. ..	41
Figure 25: Summation method technique to recover absorptance from calorimetry data	43
Figure 26: Saturation method technique to recover absorptance from calorimetry data.	44
Figure 27: AFIT's Complete Angle Scatter Instrument's mode of operation.. ....	45
Figure 28: FTIR setup used for the polarization dependent loss experiment. ....	47
Figure 29: Rotating sample mount used for FTIR transmission measurements.....	47
Figure 30: Plot of variation in recorded temperature with an idle calorimetry setup. ....	50
Figure 31: Plot representing a linear relationship between the absolute change in temperature of the sample and applied laser power.....	51
Figure 32: Absorption coefficient versus photon energy for Si and GaAs.....	52
Figure 33: Dominant role of free-carrier absorption for energies below the bandgap ....	53
Figure 34: Change in absorption with varying free-carrier doping levels of GaAs.....	54
Figure 35: Higher absorption found in ZnSe sample with increasing free-carrier concentration.....	55

Figure 36: Direct relationship between excessive dopants and absorption loss. ....	56
Figure 37: Calorimetry curves for an HVPE grown GaP sample and a GaP wafer. ....	57
Figure 38: Calorimetry curves for an extremely low loss GaAs sample. ....	58
Figure 39: CARY Spectrophotometer transmission measurement for GaAs and GaP samples. ....	60
Figure 40: OPGaAs domain orientations used in CASI measurements for each sample	61
Figure 41: CASI measurement collected with first orientation at $\theta_i = 0^\circ$ for OPGaAs sample # F 4-26-11. ....	63
Figure 42: CASI measurement collected with first orientation at $\theta_i = 18.5^\circ$ for OPGaAs sample # F 4-26-11.. ....	63
Figure 43: CASI measurement collected with second orientation at $\theta_i = 0^\circ$ for OPGaAs sample # F 4-26-11.. ....	64
Figure 44: CASI measurement collected with second orientation at $\theta_i = 18.5^\circ$ for OPGaAs sample # F 4-26-11. ....	65
Figure 45: CASI measurement collected with first orientation at $\theta_i = 0^\circ$ for OPGaAs sample # F 5-11-11. Diffraction patterns observed. ....	66
Figure 46: CASI measurement collected with first orientation at $\theta_i = 18.5^\circ$ for OPGaAs sample # F 5-11-11. Diffraction patterns observed. ....	67
Figure 47: CASI measurement collected with first orientation at $\theta_i = 37^\circ$ for OPGaAs sample # F 5-11-11. Diffraction patterns observed. ....	68
Figure 48: CASI measurement collected with first orientation at $\theta_i = 55.5^\circ$ for OPGaAs sample # F 5-11-11. Diffraction patterns observed. ....	69

	Page
Figure 49: CASI measurement collected with second orientation at $\theta_i = 0^\circ$ for OPGaAs sample# F 5-11-11. Single diffraction peak observed. ....	70
Figure 50: CASI measurement collected with second orientation at $\theta_i = 18.5^\circ$ for OPGaAs sample# F 5-11-11. Single diffraction peak observed. ....	70
Figure 51: CASI measurement collected with second orientation at $\theta_i = 37^\circ$ for OPGaAs sample # F 5-11-11. Single diffraction peak observed. ....	71
Figure 52: CASI measurement collected with second orientation at $\theta_i = 55.5^\circ$ for OPGaAs sample # F 5-11-11. Single diffraction peak observed. ....	71
Figure 53: FTIR transmission measurements for sample # F 4-26-11 as the sample is rotated from $0^\circ$ to $140^\circ$ under a constant polarization incident light. ....	73
Figure 54: Change in transmission through the sample # F 4-26-11 at different wavenumbers as it is rotated from 0 to 360 degrees. ....	73
Figure 55: FTIR transmission measurements for sample F 5-11-11 as the sample is rotated from $0^\circ$ to $140^\circ$ under a constant polarization incident light. ....	74
Figure 56: Change in transmission through the sample # F 5-11-11 at different wavenumbers as it is rotated from 0 to 360 degrees. ....	74
Figure 57: Change in incident intensity due to clipping of the beam by the sample holder .....	75
Figure 58: Clipping of incident beam caused by misaligned sample holder. ....	76
Figure 59: Minimized clipping of incident beam with a second sample holder. ....	76
Figure 60: Polarization effect from the grated material illustrated for both the samples	78

Figure 61: Photothermal deflection setup as a future recommendation to measure the absorption coefficient of various samples. ....	82
Figure 62: Sample # F 4-26-11 Run#1 cooling curve fitted to an exponential decay function. ....	83
Figure 63: Sample # F 4-26-11 Run#2 cooling curve fitted to an exponential decay function. ....	84
Figure 64: Sample # F 4-26-11 Run#3 cooling curve fitted to an exponential decay function. ....	84
Figure 65: Sample # F 5-11-11 Run#1 cooling curve fitted to an exponential decay function. ....	85
Figure 66: Sample # F 5-11-11 Run#2 cooling curve fitted to an exponential decay function. ....	85
Figure 67: Sample # F 5-11-11 Run#3 cooling curve fitted to an exponential decay function. ....	86
Figure 68: Sample # F 5-11-11 Run#4 cooling curve fitted to an exponential decay function. ....	86
Figure 69: Sample # B 9-23-10 Run#1 cooling curve fitted to an exponential decay function. ....	87
Figure 70: Sample # B 9-23-10 Run#2 cooling curve fitted to an exponential decay function. ....	87
Figure 71: Sample # B 9-23-10 Run#3 cooling curve fitted to an exponential decay function. ....	88

	Page
Figure 72: Sample # B 9-23-10 Run#4 cooling curve fitted to an exponential decay function. ....	88
Figure 73: Calorimetry curves for an unpatterned GaAs sample. ....	89
Figure 74: Calorimetry curves for an intentionally Si doped OPGaAs sample. ....	89
Figure 75: Calorimetry curves for a commercially bought GaP wafer. ....	90
Figure 76: Calorimetry curves for an AFRL HVPE grown GaP sample. ....	90
Figure 77: Calorimetry curves for an Fe <sup>2+</sup> doped ZnSe sample with free-carrier concentration of $4.6 \times 10^{18} \text{ cm}^{-3}$ . ....	91
Figure 78: Calorimetry curves for an Fe <sup>2+</sup> doped ZnSe sample with free-carrier concentration of $8.3 \times 10^{18} \text{ cm}^{-3}$ . ....	91
Figure 79: Thermal image of an OPGaAs sample before laser was started. ....	95
Figure 80: Thermal image of an OPGaAs sample during laser saturation stage. ....	95
Figure 81: Thermal image of an OPGaAs sample after the laser was stopped. ....	96

## List of Tables

	Page
Table 1: Feature comparisons between promising laser source conversion materials.. ....	4
Table 2: Description of samples used for laser calorimetry. ....	31
Table: 3: Saturation stage data rows describing the summation method of determining absorptance .....	42
Table 4: Absorptance and absorption coefficient values found using Equation (19) for all samples. ....	59

# **Characterizing Optical Loss in Orientation Patterned III-V Materials Using Laser Calorimetry**

## **I. Introduction**

### **Motivation**

Mid-Infrared (MIR) laser sources are essential for vital U.S. Air Force applications like IR countermeasures[1], laser radar and remote sensing [2]. Sensing applications operate by collecting radiation emitted from the target and the background via a detection system. Directed Infrared Countermeasure (DIRCM) systems mode of operation involves detecting a target, resolving it's threat level and then if necessary, using a guide beam to track the target and applying a high energy laser beam to achieve desired lethal fluence [3]. Active IR countermeasure technique like an IR jammer is an onboard system that protects the aircraft by blinding or defeating heat-seeking missiles using counter-sensor applications [4].

For all such applications, radiation has to travel through the intervening atmosphere, at which point, this radiation gets attenuated due to absorption and scattering. In the absorption process, photons at higher energy level get absorbed and new photons at lower energy level get emitted. Scattering takes place primarily due to aerosols in the atmosphere that spread the photons off-axis and reduce the energy delivered to the target. Figure 1 [5], exhibits atmospheric transmission at sea level, with high transmission windows present between 2-5 $\mu\text{m}$  and 8-12 $\mu\text{m}$ . The primary absorbers of radiation in this range are trace gases and water vapor.



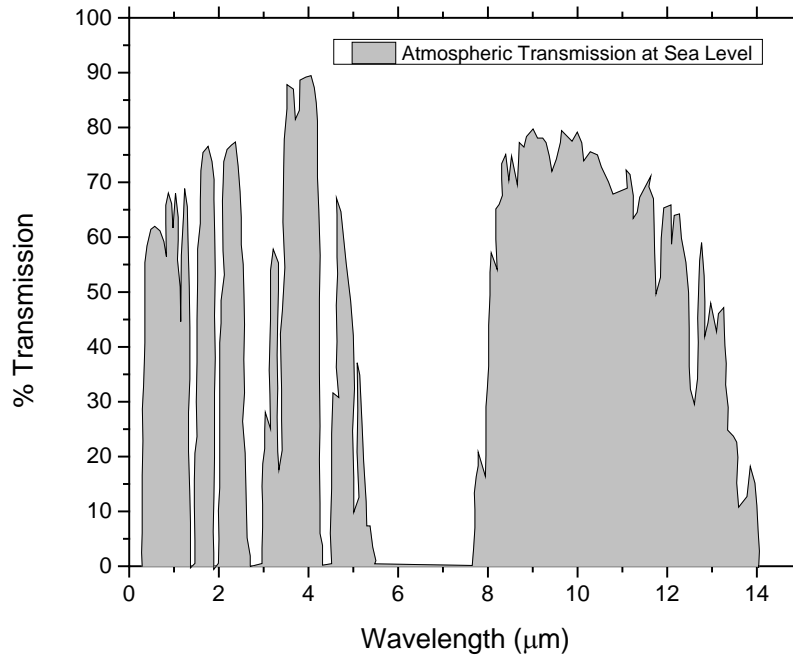


**Figure 1: Atmospheric transmittance at sea level in the IR region. Plot was re-drawn and modified using data from [5]. Some Air Force applications require laser output in the 2-5  $\mu\text{m}$  range window due to high transmittance and fewer absorption bands in this region.**

Air Force MIR applications listed above and specifically, target acquisition, recognition and designation require laser output in the 2-5  $\mu\text{m}$  wavelength range [6]. This range allows for maximum transmission through Earth's atmosphere because there is low natural IR radiation at these wavelengths and lower absorption due to water vapor and carbon dioxide. MIR LIDAR also requires pulsed laser sources in this transmission window for atmospheric remote sensing applications such as measurement of aerosols and greenhouse gases, tracking  $\text{CO}_2$  absorption across the globe, improving certain disaster predictions by measuring vegetation over vulnerable areas, etc. [7]. This creates a need for tunable, efficient and reliable laser sources that are transparent in the 2-5  $\mu\text{m}$  range. Successful candidates for countermeasure lasers should exhibit the critical

performance characteristic of 'useful energy on target'. This characteristic is related to the laser source's spectral coverage, beam quality, turn-on time, power, modulation/duty cycle and efficiency [3]. A multi-wavelength output is needed to cover the spectral range from 2-5  $\mu\text{m}$ , matching the atmospheric transmission window. Beam quality is related to the effective spot size on the target and it usually worsens due to atmospheric effects resulting in lower power delivered as compared to a diffraction-limited beam. Turn-on time of the laser should be minimal in order to decrease the DIRCM system cycle from the recognition and pursuing of the target to a successful laser engagement. Modulation relates to the temporal output of the laser source and duty cycle refers to the actual 'laser on' time as compared to the pulse period. Thermal susceptibility of the laser to the heat load impacts the modulation while the thermal management impacts the sustainable duty cycle performance. Finally, efficiency improvement is a continuous effort for military applications with benefits like increases in the prime power of the system, reduction in the operational size due to lower thermal management issues and overall reduction in costs due to lower complexity of the laser system.

### **Problem Statement**

Not many materials have laser transitions in the 2-5  $\mu\text{m}$  range, and the few that do, lack the needed breadth of wavelength tunability. Hence, nonlinear processes like Optical Parametric Oscillation (OPO), Optical Parametric Generation (OPG), etc. are employed to convert frequency of readily available laser sources into desired wavelength for pertinent applications. An OPO utilizes a second order nonlinear interaction to convert the pump frequency,  $\omega_p$ , into a signal,  $\omega_s$ , and idler frequency,  $\omega_i$ . This

conversion satisfies the relationship:  $\omega_p = \omega_s + \omega_i$  with  $\omega_i < \omega_s$ . OPO derived sources are most relevant for military applications that require tunable high power lasers [7]. Some of the pump sources used for frequency conversion by nonlinear processes are neodymium-doped yttrium aluminum garnet (Nd:YAG) laser at 1064 nm, titanium sapphire laser from 720-810 nm and solid state fiber lasers.

A comparison of the important properties of commonly used frequency conversion materials are shown in Table 1 [9]. Most promising among them are the QPM III-V materials.

**Table 1: Laser source conversion material feature comparisons [9]. III-V materials like GaAs and GaP are the most promising with broad transmission windows, high nonlinear coefficient.**

Properties	ZnGaP <sub>2</sub>	AgGaSe <sub>2</sub>	LiNbO <sub>3</sub>	GaAs	GaP
Transmission window [ $\mu\text{m}$ ]	1.8-12	0.73-18	0.4-5	1 - 16	0.55-12
Nonlinear optical coefficient [ $\text{pm.V}^{-1}$ ]	111	43	27	94	71
Laser damage threshold [ $\text{MW/cm}^2$ ]	6	1.25	2	3	Unknown
Birefringence	Yes	Yes	No	No	No
Thermal Conductivity [ $\text{W.m}^{-1}.\text{K}^{-1}$ ]	36	1.1	5.6	46	

Orientation patterned (OP), III-V materials are promising nonlinear frequency conversion materials that can be used in high power, tunable laser sources in the MIR range for several Air Force applications. Due to its high nonlinearity, high thermal conductivity, and low losses in a greater wavelength region, OPGaAs is an attractive option for many Air Force applications. GaP is another promising III-V material of interest to the Air Force. It exhibits similar properties to GaAs with the advantage being

the negligible two-photon absorption in GaP at around 1  $\mu\text{m}$ . GaP also has higher band gap of 2.26 eV as compared to 1.42 eV of GaAs. This makes it easier to pump GaP with commercially available 1  $\mu\text{m}$  solid state fiber lasers.

Zinc-Germanium Diphosphide (ZGP) has a large nonlinear optical coefficient, good transparency range [10], but the low-loss transmission range of OPGaAs extends to 12  $\mu\text{m}$ , well beyond the limits of ZGP, which exhibits multi-phonon absorption beyond 8.5  $\mu\text{m}$ . OPGaAs also has higher thermal conductivity than ZGP which helps improve device efficiency [8]. The short- wavelength cut-off in ZGP also limits the pump wavelength to be greater than or equal to 2  $\mu\text{m}$  [9]. AgGaSe<sub>2</sub> has a wide transparency region [10], permitting higher range of OPO output frequencies. An OPO based on AgGaSe<sub>2</sub> does not reach optimal output power levels due to inadequate heat dissipation because of its low thermal conductivity [6].

Lithium niobate is the current choice for infrared countermeasure (IRCM) devices due to years of testing, ease of manufacturing, and tunability across a wide spectral range [6]. LiNbO<sub>3</sub> is a ferroelectric material with large electro-optic and acousto-optic coefficients. It is one of the most versatile and highly studied optical material. Quasi phase matching (QPM) provides LiNbO<sub>3</sub> with periodic poling (PPLN) and gives it a higher nonlinear coefficient. Nevertheless, in comparison with GaAs, LiNbO<sub>3</sub> is not as transmissive and therefore it suffers with performance degradation at wavelengths greater than 4  $\mu\text{m}$  as shown in Figure 2.

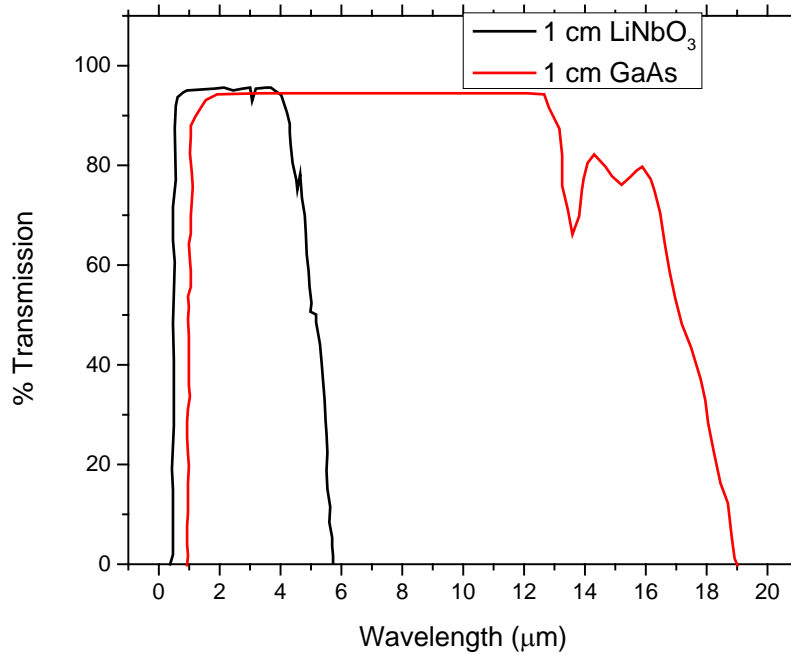


**Figure 2: Transmission spectra comparison between LiNbO<sub>3</sub> and GaAs. Plot was re-drawn and modified using data from [11]. LiNbO<sub>3</sub> is far less transmissive at wavelengths greater than 4 μm.**

## Research Scope

Characterization of major sources of loss in these laser source materials is of critical importance to achieve efficient device operation [12]. Signal conversion efficiency in orientation patterned material is restricted by the optical transmission losses involved, which are based on the properties of the crystal structure in the material [13]. Optical loss sources include the two photon absorption, free carrier absorption, deep level absorption and scattering produced by the domain walls. This thesis focuses on the absorption and scatter related material losses in III-V materials

Matter can be simplified into discrete electric charges that are both positively and negatively charged. An incident radiation electric field hence produces a harmonic motion in the charges inside the matter. Electromagnetic energy radiation from these

accelerated electric charges is the radiation scattered by the obstacle. In engineered grating patterns, domains are grown next to each other with an antiphase boundary at the domain wall. These domain walls have been shown to be littered with defects extending a few micrometers on either side of the wall [14]. These defects and dislocations augment scattering of light at the wall [15]. Also, any imperfect phase matching due to missing domain reversals or non-symmetric patterns is a major source of device efficiency loss. Understanding loss due to scatter from the crystal is one of the research objectives of this thesis. A Complete-Angle Scatter Instrument (CASI) employing an 8.15  $\mu\text{m}$ , 2mW laser is used for characterization of orientation patterned III-V materials.

Another major source of loss is related to the material itself. Optical absorptance helps in deciding the worthiness of a nonlinear material for pertinent applications such as electro-optic switching, frequency conversion in OPO's, etc. Material loss sources include among others, free carrier absorption and deep level absorption (EL2). Fundamental wavelength absorption induced by free carriers from dopants like Si and Ge inhibits slope efficiency which is defined as the gradient of the laser output versus pump power curve. This type of absorption increases with increase in pump wavelength [12].  $\text{Si}_{\text{Ga}}$  is the primary source of donors while Ga vacancies are sources of native acceptors. EL2 is a deep donor, attributed to be an As-As anti site defect in orientation patterned GaAs.

Absorption losses determination approaches can be divided into three categories: a transmission measurement using Beer's law to calculate absorption; by emissometry, wherein the radiation emitted is equated to the absorption; and by calorimetry where the absolute change in temperature of the sample is related to the absorption [16].

Absorption losses in III-V materials are investigated using Laser Calorimetry in this thesis. Transmission techniques are usually limited to detecting absorption losses greater than 1% as most of the observed loss in low absorption samples is reflection from the entrance and exit surfaces. In emissometry, determination of absorption coefficient is difficult due to the influx of unwanted radiation and additional noise from temperature variations in the surroundings. Given the acute relationship between thermal emission of a body and the radiation wavelength, the sensitivity of the system also gets heavily dependent on wavelength [16]. Meanwhile, thermocouple calorimetry as practiced in this thesis is among the most widely used technique. Using the adiabatic approach and the assumption that the temperature across the sample is homogeneous, the decay constant of the decline in sample temperature is measured. Sensitivity is higher in this technique as compared to transmission measurement, and unlike emissometry, sensitivity in thermocouple calorimetry is not dependent on wavelength.

Absorption can be measured using various techniques like laser calorimetry [16], photothermal deflection [17], photothermal interferometric technique [18], thermal imaging [19], thermal lens [20] and transient optical absorption [21]. Photothermal techniques, such as probe beam deflection and thermal lens detection, are popular in low absorption measurement of optical coatings. Interferometric technique is mainly used for detecting thermal lensing in optics due to light absorption from a laser beam. Thermal imaging is used to measure the surface absorption of optical coatings used in high power laser systems. Surface thermal lensing technique computes the absorption of transmissive optical components (mainly coatings) by using a probe beam to calculate the absorptance induced surface deformation. Transient optical absorption is primarily used

for determination of absolute nonlinear absorption in dielectric coatings. Laser calorimetry's advantages include the easy to use equipment and straightforward directions to measure absorption. The International Organization of Standardization (ISO) has also selected laser calorimetry as an international standard for calculating absorptance losses. Previously, Meyer had worked on similar loss characterization using an integrated sphere method [6]. Since higher sensitivity was required for the comparatively lower loss III-V materials, laser calorimetry was used in this thesis. Absorption loss can be the primary limiting factor in performance of a device. It is therefore essential to measure these losses accurately. Laser calorimetry is used to measure such loss by heating the material with irradiation from a laser while recording the rise in temperature. Then the sample is allowed to cool while continuing to record temperature. The time taken to reach the original temperature is related to the absorption coefficient.



## **Overview**

This work undertook the characterization of patterned III-V materials by understanding the losses related to absorption and scattering. Chapter II of this thesis looks at the relevant theory of nonlinear processes, template fabrication, laser calorimetry and scattering principle. It also includes an account of the work done by others in this area.

Chapter III provides detailed information about the patterned III-V materials used in the experiments. Laser calorimetry and scattering measurement experiments are also described. Polarization dependent absorption experiment was performed on some samples. This experiment is also specified here.

Chapter IV presents the results of all the experiments. Finally, Chapter V provides conclusions and some recommendations for future work.

## II. Literature Review

### Nonlinear Processes

Boyd describes nonlinear effects as occurring when “the response of a material system to an applied optical field depends in a nonlinear manner” upon the input electromagnetic wave [22]. A better understanding of optical nonlinearity is gained by looking at the dependence of polarization  $P(t)$  of a material on the strength  $E(t)$  of an applied optical field. Equation (1) describes the linear dependence of polarization on the electric field strength

$$P(t) = \epsilon_0 \chi^{(1)} E(t), \quad (1)$$

where  $\epsilon_0$  is the permittivity of free space and the constant of proportionality  $\chi^{(1)}$  is known as the linear susceptibility. This equation is adapted for nonlinearity by expressing the polarization as a power series in the field strength,

$$\begin{aligned} P(t) &= \epsilon_0 [\chi^{(1)} E(t) + \chi^{(2)} E^2(t) + \chi^{(3)} E^3(t) + \dots] \\ &= P^{(1)}(t) + P^{(2)}(t) + P^{(3)}(t) + \dots. \end{aligned} \quad (2)$$

Accordingly,  $\chi^{(2)}$  and  $\chi^{(3)}$  are known as the second and third -order non-linear optical susceptibilities, respectively [22]. Physical processes that occur as a result of  $P^{(2)}(t)$ , the second-order nonlinear polarization, are relevant to this thesis and include second-harmonic generation, sum and difference frequency generation, etc.

An optical field with two distinct frequency components that are incident upon a second-order nonlinear optical medium can be given by

$$E(t) = E_1 e^{-i\omega_1 t} + E_2 e^{-i\omega_2 t} + c. c. \quad (3)$$

Then the second-order contribution to the nonlinear polarization from Equation (2) can be given as,

$$P^{(2)}(t) = \epsilon_0 \chi^{(2)} [E_1^2 e^{-2i\omega_1 t} + E_2^2 e^{-2i\omega_2 t} + 2E_1 E_2 e^{-i(\omega_1 + \omega_2)t} + 2E_1 E_2^* e^{-i(\omega_1 - \omega_2)t} + c. c.] + 2\epsilon_0 \chi^{(2)} [E_1 E_1^* + E_2 E_2^*]. \quad (4)$$

Expressing this result in a convenient notation,

$$P^{(2)}(t) = \sum_n P(\omega_n) e^{-i\omega_n t}. \quad (5)$$

Complex amplitudes of the various frequency components describe physical processes such as second-harmonic generation (SHG), sum-frequency generation (SFG), difference frequency generation (DFG), and optical rectification (OR) as shown in Equation (6),

$$\begin{aligned} P(2\omega_1) &= \epsilon_0 \chi^{(2)} E_1^2 \quad (\text{SHG}), \\ P(2\omega_2) &= \epsilon_0 \chi^{(2)} E_2^2 \quad (\text{SHG}), \\ P(\omega_1 + \omega_2) &= 2\epsilon_0 \chi^{(2)} E_1 E_2 \quad (\text{SFG}), \\ P(\omega_1 - \omega_2) &= 2\epsilon_0 \chi^{(2)} E_1 E_2^* \quad (\text{DFG}), \\ P(0) &= 2\epsilon_0 \chi^{(2)} (E_1 E_1^* + E_2 E_2^*) \quad (\text{OR}) \end{aligned} \quad (6)$$

There are four different nonzero frequency components offered due to nonlinear polarization. Although, appreciable intensity of only one frequency can be efficiently produced in the output signal depending on the phase-matching criteria met. This criteria is explained in detail later.

### ***Optical Parametric Oscillator***

In DFG, the frequency of the resulting wave is the difference of the applied fields. Thus, DFG can be used to produce tunable IR radiation by using a mixture of a fixed-frequency visible laser with a frequency tunable visible laser source. This process leads

to the amplification of the lower-frequency input field, known as optical parametric amplification (OPA), while the net system gain can be used to construct a device known as an optical parametric oscillator (OPO). This concept is summarized in Figure 3. The DFG process produces  $\omega_i$ , while amplifying the lower frequency input field,  $\omega_s$ . Conventionally,  $\omega_p$  is known as the pump frequency and is associated with the pump photon,  $\omega_s$  is the signal frequency and  $\omega_i$  is called the idler frequency. Signal and idler refer to the two remaining photons in the three photon OPO interaction.

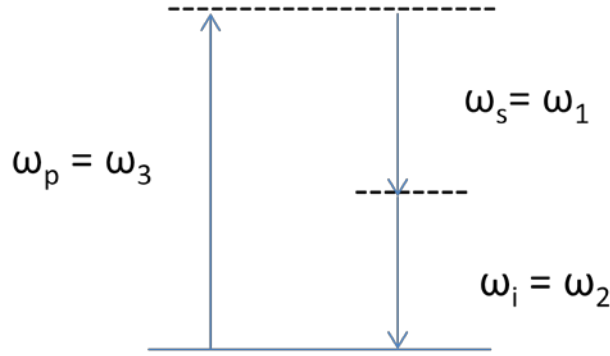


**Figure 3: Connection between difference frequency generation and optical parametric oscillation. In generating the difference frequency  $\omega_i$ , the lower frequency  $\omega_s$  is amplified.**

The gain associated with the process of OPA can in the presence of feedback produces oscillations as shown in Figure 4. In an OPO, the pump photons are converted into signal and idler photons. This nonlinear process is realized when two fundamental laws are met: conservation of energy and conservation of momentum.

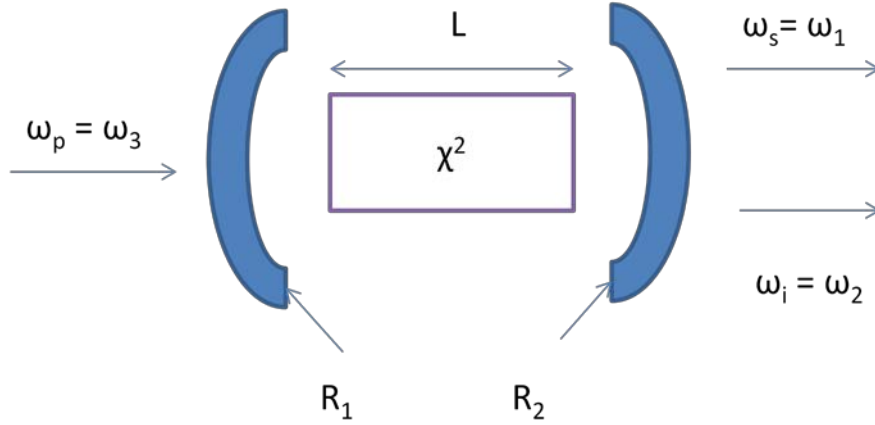


**Figure 4:** The gain associated with the process of optical parametric amplification can be used to construct the optical parametric oscillator (OPO). An OPO is used to convert the pump photons,  $\omega_p$ , into a signal,  $\omega_s$ , and idler photon,  $\omega_i$ .

Conservation of energy of the pump, signal, and idler photons is described by,

$$\frac{h}{2\pi} \omega_{pump} = \frac{h}{2\pi} \omega_{signal} + \frac{h}{2\pi} \omega_{idler} \quad (7)$$

where  $h$  is Planck's constant, and  $\omega$  is the angular frequency. The pump photon with an intense electric field and frequency,  $\omega_p$ , induces a change in the polarization, or dipole moment per unit volume of the nonlinear crystal. If the energy and momentum relationships are satisfied, then this polarization change gives rise to two distinct frequencies,  $\omega_s$  and  $\omega_i$ . The idler and signal gain energy from the pump frequency and all three frequencies propagate out of the system as shown in Figure 4. The idler does not resonate and propagates without reflection in a singly resonant oscillator, while a cavity in which both idler and signal frequencies are resonant or the pump and signal frequencies are resonant is called a doubly resonant oscillator.

An OPO also has to conserve momentum to perform successfully. In order for the momentum to be conserved, the following phase matching condition must be met:

$$\frac{h}{2\pi} \bar{k}_{pump} = \frac{h}{2\pi} \bar{k}_{signal} + \frac{h}{2\pi} \bar{k}_{idler} \quad (8)$$

Meyer provides a clear and concise derivation of this relationship [6]. The amount of phase mismatch  $\Delta k$  (the difference of the wave vectors) as shown in Equation (9), governs the efficiency of the OPO conversion process.

$$\begin{aligned} \Delta k = k_{pump} - k_{idler} - k_{signal} &= \frac{2\pi n_{pump}}{\lambda_{pump}} - \frac{2\pi n_{signal}}{\lambda_{signal}} - \frac{2\pi n_{idler}}{\lambda_{idler}} \\ &= \omega_{pump} - \omega_{signal} - \omega_{idler} \end{aligned} \quad (9)$$

Birefringent phase matching (BPM), and quasi-phase matching (QPM) are used extensively to eliminate the phase mismatch. Birefringent materials like zinc germanium phosphide (ZGP),  $\text{ZnGeP}_2$ , and silver gallium selenide,  $\text{AgGaSe}_2$  are employed in an OPO using BPM, achieved by choosing a suitable direction or critical angle for transmission of light through the crystal. But due to walkoff between interacting waves inside the crystal, a limit exists on the efficiency of mid-IR conversion [9]. An alternate method for phase matching used primarily to overcome this walkoff deficiency is QPM. This technique deliberately introduces a periodic phase change between interacting waves at defined periods through the material. QPM is achieved in ferroelectric materials like lithium niobate,  $\text{LiNbO}_3$ , by periodic poling of the material using strong electric fields. Also III-V isotropic materials like gallium arsenide, GaAs, and gallium phosphide, GaP, are employed in the conversion business via QPM by structurally modifying the crystals and incorporating the grating patterns into the growth processes [23].

## Quasi-Phase Matching

The fundamental equations governing QPM have been thoroughly reviewed in articles and textbooks, rather than deriving them in detail, this treatment will only highlight the relevant equations and theory. In-depth take on this subject can be found in textbooks from Yariv and Yeh or from Boyd [22, 24].

In QPM, the sign of the effective nonlinear coefficient,  $d_{eff}$ , is flipped at regular intervals known as the domain period,  $\Lambda$ , to minimize the phase mismatch,  $\Delta k$ . The reversal of the nonlinear coefficient term shifts the polarization response of the crystal back into phase with the pump beam allowing for continued net positive energy flow from the pump into the signal and idler frequencies [6]. The nonlinear interaction continues to grow due to the domain reversals although not as efficiently as BPM. A conversion efficiency comparison is shown in Figure 5. In the absence of domain reversals, energy would flow back into pump leaving no net signal and idler, energy would simply flow sinusoidally back and forth between the input and output waves. The domain period is chosen to be equal to the phase mismatch present in the nonlinear crystal. This period also contributes to the total momentum of the system,

$$\Delta k = k_{pump} - k_{idler} - k_{signal} - \frac{2\pi}{\Lambda}. \quad (10)$$

The domain period for first-order QPM is twice the coherence length,  $l_{coh}$ . The physical distance of each coherence length in a first order QPM is defined by,

$$l_{coh} \equiv \frac{\pi}{k_{pump} - k_{signal} - k_{idler}} \quad (11)$$

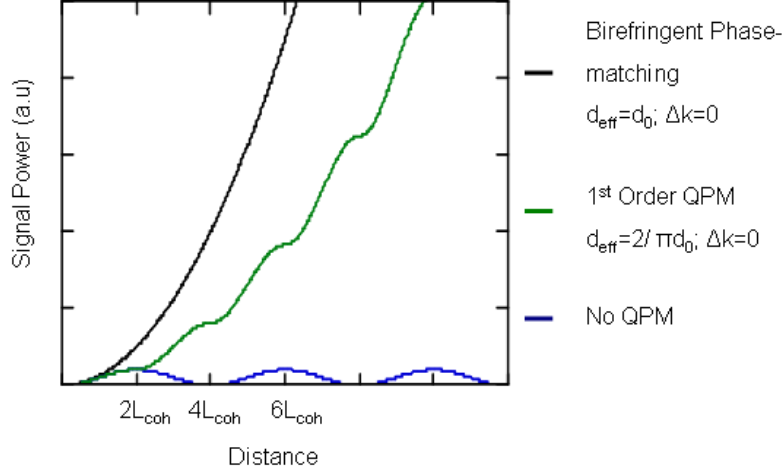


**Figure 5: Comparison of the conversion efficiencies for different phase matching conditions. The black curve represents perfect BPM and assumes the phase matching condition is perfectly satisfied. The green curve assumes the case of QPM, in which the nonlinear coefficient is periodically modulated with a period of twice the coherent length,  $L_{coh}$ . The blue curve assumes that the wavevector mismatch is nonzero. This figure is reproduced from Figure 2 of Meyer's 2006 thesis [6].**

Appropriate QPM grating period can be designed and determined if the pump frequency is known and a nonlinear material with well-defined dispersion is used [25]. The period for first order QPM interaction is given by,

$$\Lambda = \frac{2\pi}{\Delta k} = \left( \frac{n_p}{\lambda_p} - \frac{n_s}{\lambda_s} - \frac{n_i}{\lambda_i} \right)^{-1}, \quad (12)$$

where  $\lambda_p$ ,  $\lambda_s$ , and  $\lambda_i$  are the wavelengths of the pump, signal and idler, respectively, while  $n_p$ ,  $n_s$ , and  $n_i$  are the refractive indices at their respective wavelengths. The indices can be found using Sellmeier equations for GaAs [26]. The Sellmeier equation, a relationship between the refractive index and wavelength for GaAs is plotted in Figure 6 [27].



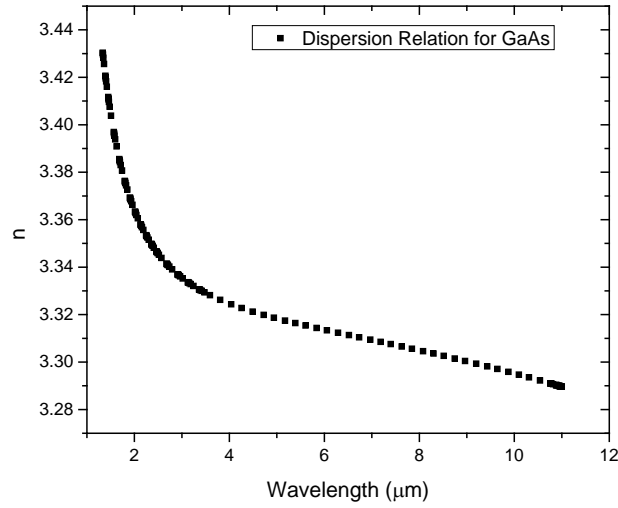


**Figure 6: Sellmeier equation, a relationship between the refractive index and wavelength for GaAs. Plot was created using equation from [27].**

Figure 7 shows the tuning curve for a 2.05μm and 1.90μm pumped OPGaAs OPO [43].

For each QPM grating period, the tuning curve provides two wavelengths corresponding to the signal and idler.

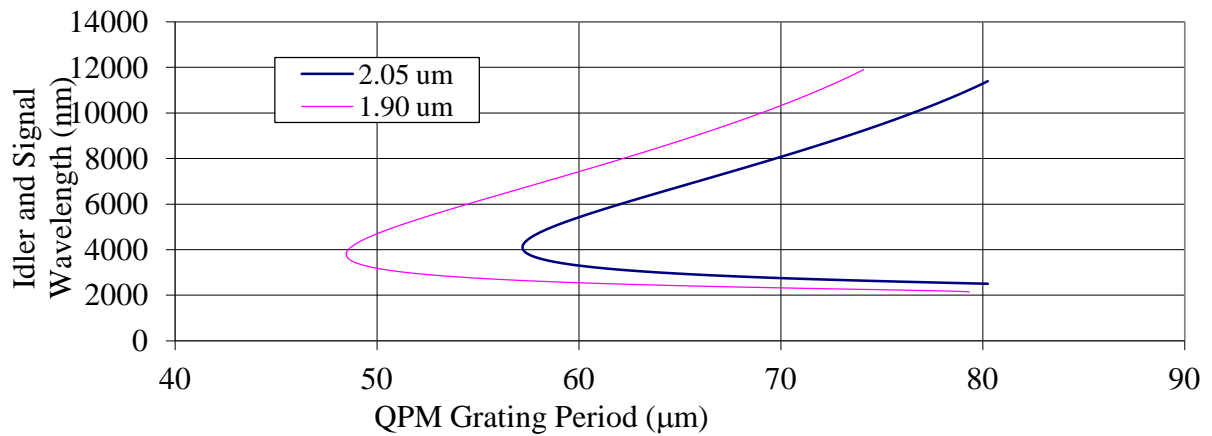


**Figure 7: 2.05 μm and 1.90 μm pumped GaAs OPO tuning curve provides two distinct wavelengths for selected QPM grating period. The wavelengths correspond to signal and idler. This figure is reproduced from Figure 1.1 of Shell's 2007 thesis [43].**

### **Fabrication of III-V materials like GaAs**

The crystallographic properties of GaAs (cubic point group symmetry) and its lack of spontaneous ferroelectric polarization hamper traditional BPM and well-known electric-field poling technique [29]. Modulation of the nonlinear coefficient to achieve QPM is one solution to this problem. This is achieved by fabricating templates with Orientation Patterned surfaces and then utilizing Hydride Vapor Phase Epitaxy (HVPE) to grow waveguide structures or bulk crystal on top of templates. A more detailed version of the growth and fabrication techniques of OPGaAs can be found in Yu's dissertation [30]. OP design can be attained by either using an all-epitaxial fabrication route or by using wafer bonding techniques. In wafer bonding Stack of plates with opposite orientation is fused together to create the OP design in wafer bonding. Figure 8 illustrates the fabrication process of QPM structures using wafer bonding. Waveguides prepared using wafer bonding templates have shown high propagation losses due to initial corrugations [29]. Although OPO, SHG and DFG operations have been demonstrated using wafer bonding technique, the devices based on this technique have been too lossy [30]. Stacking too many wafers is extremely difficult so longer device length is hard to achieve resulting in lower conversion efficiency.

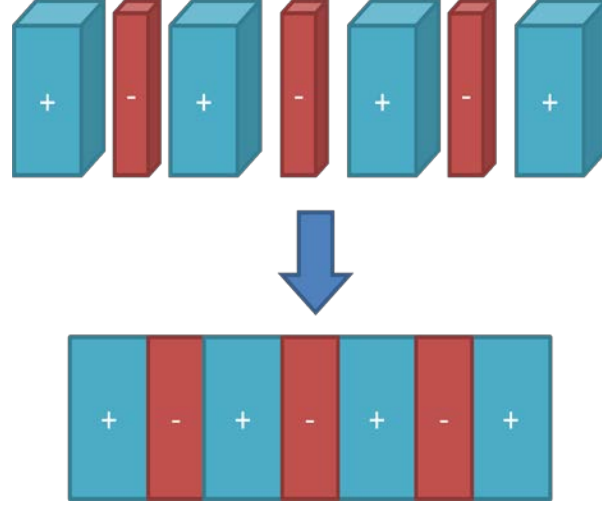


**Figure 8: Modulation of the nonlinear coefficient to achieve QPM using wafer bonding. Every two adjacent wafers have a  $90^\circ$  rotation about  $[001]$  axis.**

Wafer bonding technique is skipped in this discussion as the templates used here were grown using an all epitaxial fabrication route. This method consists of growing a thin nonpolar Ge layer on GaAs substrate which allows a rotation of the top regrowth GaAs layer with respect to the bottom one [31]. QPM domain patterns are realized by using lithographic and etch-stop processes. This completes the template fabrication process. Molecular beam epitaxy is then used to grow the lower layer of GaAs to a thickness of approximately  $10\ \mu\text{m}$ . Finally, HVPE is used to reach device quality thickness of around  $500\ \mu\text{m}$ . The fabrication process of OPGaAs is summarized in Figure 9 [32], while the HVPE growth on patterned templates (shown in step 4-5 in Figure 9), is illustrated in Figure 10.

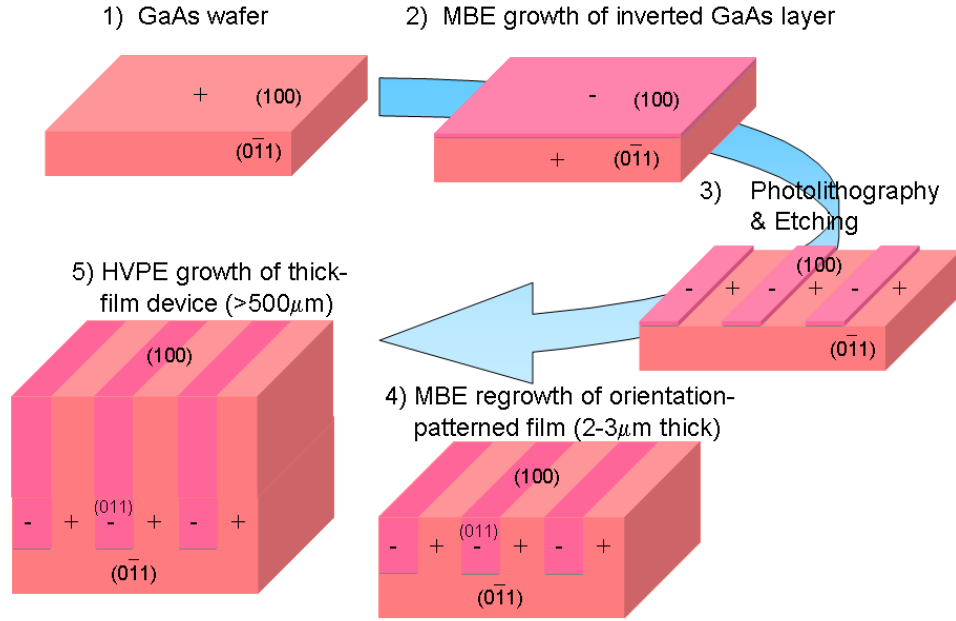


**Figure 9: OPGaAs growth process to produce modulation of the nonlinear coefficient to achieve QPM.**

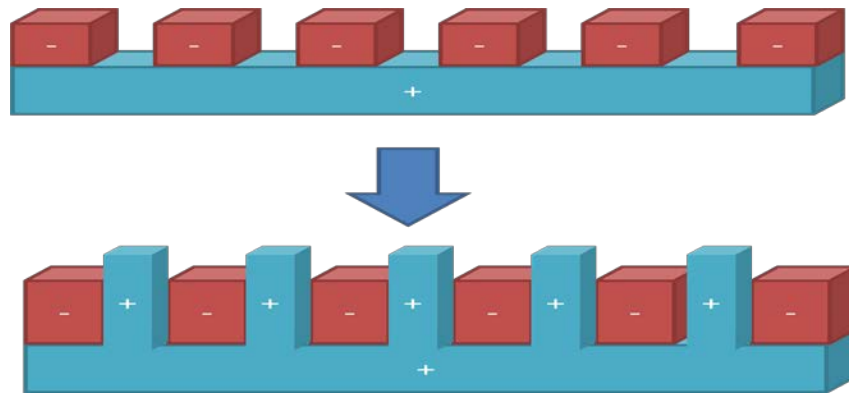


**Figure 10: Orientation patterned template (top part) with surfaces of GaAs with two orientations exposed is first fabricated. Then a thick GaAs layer is epitaxially grown on the template (bottom part) with both domains developing vertically.**

## Laser Calorimetry Theory

Laser calorimetry is initiated by directing the incident beam on the sample. The theory then relates the temperature rise of the sample and the associated rate of rise to the absorption of the material. A general model of heat equation within the sample during laser irradiation can be complicated considering the unusual shape of the sample and the varying impact of the laser profile (assumed Gaussian) has on the sample. However, a good approximation of the change in sample temperature is given by the equation,

$$\frac{dT}{dt} = \frac{aP}{c_p m} - \frac{T - T_0}{\tau}, \quad (13)$$

where  $T$  is sample temperature,  $\tau$  is time constant,  $T_0$  is ambient temperature,  $P$  is the laser power incident on sample,  $c_p$  is the specific heat,  $m$  is the mass of the sample and  $a$  is the fraction of incident power absorbed (absorptance) [33]. This equation is an assumption because it assumes that due to a large enough thermal conductivity of the sample, the small variations in temperature across the sample can be ignored and the temperature profile can be taken constant. This approximation is supported in the thesis by taking IR temperature profile pictures (shown in Appendix B) of the sample in various stages of laser calorimetry measurement to ensure conformity to this assumption. If the laser power is assumed constant, the solution [33] to Equation (13) is,

$$T(t) = \left(T_0 + \frac{aP\tau}{mc_p}\right) + \left(T_i - \left(T_0 + \frac{aP\tau}{mc_p}\right)\right)e^{-\frac{t}{\tau}}, \quad (14)$$

where  $T_i$  is the initial temperature. For maximum sensitivity, the temperature rise above ambient,  $aP\tau/mc_p$  should be as large as possible. A sample data set from a GaAs wafer using a 40 mW cw laser source is shown in Figure 11.

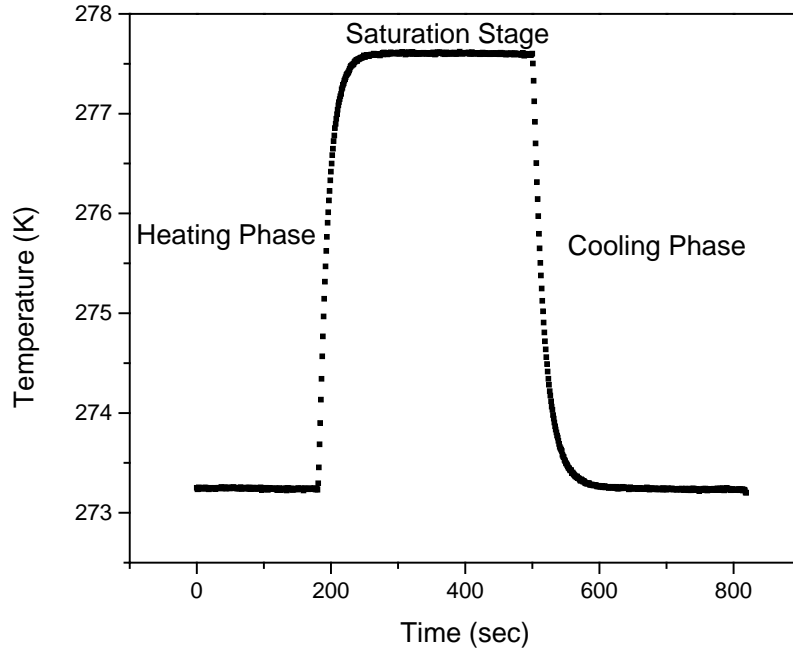


**Figure 11: Sample plot of calorimetry data set. A 40 mW cw laser source was used on a GaAs wafer. The plot points out the primary areas of interest that include the heating phase (material is irradiated by a laser), saturation stage (temperature change with respect to time is zero) and cooling phase (laser is turned off).**

During the cooling phase, the laser power is zero, so the change in sample temperature can be fitted to a decaying exponential function to yield values of  $\tau$  and  $T_0$ . While absorbance calculated includes contributions from both surface and bulk absorption, the laser calorimeter does not distinguish between the two, so surface absorption was neglected and this placed an upper limit on the bulk absorption calculated values. Absorbance is also related to the multiple passes of the laser beam through the sample caused by internal reflections. Orchard deals with this reflection issue by summarizing the multiple beams inside the sample to form two beams propagating in opposite directions,  $P_F$  (power of beam traveling in forward direction) and  $P_R$  (power of

beam traveling in backward direction) [33]. These can be defined using the transmission of the output face,  $Trans$ , and the transmitted power,  $P_{Trans}$  as,  $P_F = \frac{P_{Trans}}{Trans} e^{\alpha b}$  and

$P_R = \frac{P_{Trans}R}{Trans}$ . The total power absorbed by the sample is then,

$$P_{abs} = (P_F + P_R)(1 - e^{-\alpha b}) = \alpha P \quad (15)$$

Internal transmittance is the fraction of radiant power that reaches the opposite side of a sample of thickness  $b$ . The relation between internal transmittance and absorption coefficient ( $\alpha$ ) is [34],

$$\text{Internal Transmittance} = \exp(-\alpha b). \quad (16)$$

While the internal transmittance is independent of surface losses by reflection, absorption and scatter, it is related to absorptance. For the simple case of a uniform, uncoated optical material, Equation (15) reduces to:

$$\exp(-\alpha b) = \frac{Trans - a}{Trans - Ra}, \quad (17)$$

where  $Trans$  is the external transmittance and  $R$  is the single surface Fresnel reflectance.

Equation (16) is valid for perpendicular incidence of the laser beam on a sample with parallel surfaces, negligible optical scatter and negligible surface absorption. For some cases, when  $\alpha b \ll 1$ , a first-order expansion of Equation (17) gives,

$$a \approx \alpha b. \quad (18)$$

While solving as-is for the absorption coefficient in Equation (17) gives us,

$$\alpha = -\frac{1}{b} \ln\left(\frac{Trans - a}{Trans - Ra}\right) \quad (19)$$

This latter formula was used for calculation purposes as the criteria for Equation (18) was not met convincingly.

There are several methods to extract absorptance from the observed temperature versus time. The gradient method consists of calculating the slope of the calorimetry data curves at two instants  $t_h$  and  $t_c$  [35]. The first is taken during the heating phase while the second is taken during the cooling phase and they are chosen so that the temperature change at each instant is the same. From the derivatives taken at these two times, the absorptance is obtained from

$$\frac{d}{dt} \Delta T(t_h) - \frac{d}{dt} \Delta T(t_c) \approx \frac{aP}{mc_p}. \quad (20)$$

Equation (13) can also be used to extract absorptance. Using this equation in the 'saturation stage' of Figure 11 makes the temperature change with respect to time on the left hand side zero. The rest of the equation can be solved to find absorptance

$$a = \frac{(T - T_0)mc_p}{\tau P}. \quad (21)$$

Finally, since data is taken at discrete intervals in a laser calorimeter, the following quantities can be defined to obtain the absorptance

$$A_n = \sum_{i=1}^n \left( \frac{P_i + P_{i-1}}{2} \right) (t_i - t_{i-1}) \quad (22)$$

$$B_n = \frac{1}{\tau} \sum_{i=1}^n \left( \frac{T_i + T_{i-1}}{2} - T_0 \right) (t_i - t_{i-1}) + (T_n - T_0). \quad (23)$$

A graph of  $B_n$  versus  $A_n$  produces a straight line with a gradient of  $a/mc_p$  [33].

## Scattering Theory

Every encounter of light with particles in bulk matter can be viewed as a cooperative event of interaction between a stream of photons and an array of atoms suspended in void. When the electrons associated with these atoms and molecules react with absorption and prompt re-emission of incident electromagnetic radiation, the process



is broadly termed as scattering. Scattering can be defined as the absorption and prompt re-emission of electromagnetic radiation by electrons. Scattering principles can be widely found in great detail in optics textbooks so the following description is meant to be a lighter treatment of this topic. This summary is primarily derived from Hecht [36].

### ***Rayleigh Theory***

Rayleigh theory applies to particles that are considered small compared to the wavelength of the incident light being scattered. Scattering involving particles smaller than about  $\lambda/15$  is referred to as Rayleigh scattering. This includes most of the atoms and molecules since they are few tenths of a nanometer in diameter whereas the light has a wavelength of around 500 nm [36].

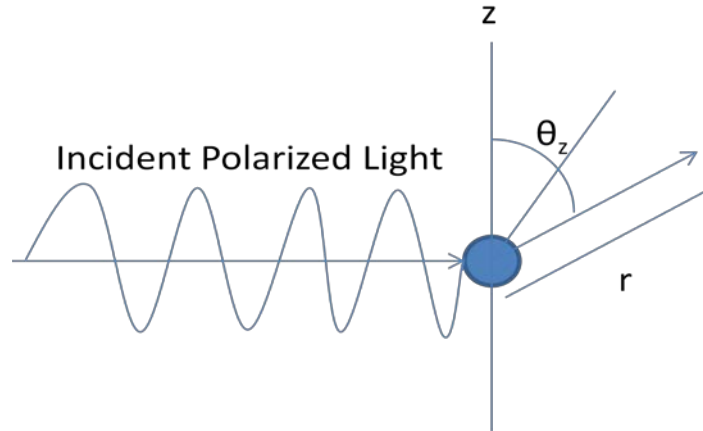


**Figure 12: Incident light polarized in the z direction incident upon a small particle causes scattering in all directions. For simplicity we choose one direction to understand the concept of Rayleigh theory which states that the scattering intensity is inversely proportional to  $\lambda^4$ .**

Rayleigh theory can be explained by first describing the theory for light scattering off a small particle in an ideal solution. A time-dependent electromagnetic field located at the origin can be described by:

$$E_z = E_0 \cos\left(\frac{2\pi c t}{\lambda}\right) \quad (24)$$

where  $E_0$  is the amplitude of the electric field,  $c$  is the speed of light, and  $\lambda$  is the wavelength of light. The subscript  $z$  stands for plane polarized light in the  $z$  direction. The incident electric field induces a dipole moment in the polarizable particle upon interaction. The magnitude of this dipole moment is proportional to the field and the proportionality constant is called polarizability,  $\alpha_p$ . The induced dipole moment is

$$p = \alpha_p E_0 \cos\left(\frac{2\pi ct}{\lambda}\right). \quad (25)$$

While this induced dipole moment radiates in all directions, for simplicity, we only account for the scattered light at a distance  $r$  from the origin along a line that makes an angle  $\theta_z$  with the  $z$  axis. The second derivative of dipole moment is acceleration of this charge so the scattered light is proportional to it. Also the electromagnetic fields fall off as  $1/r$  and the projection of the dipole moment in the observation direction is  $\sin(\theta_z)$ . Combining these effects, the electric field scattered in the  $\theta_z$  direction at a distance  $r$  is given by,

$$E_s = \frac{1}{rc^2} \frac{d^2 p}{dt^2} = \frac{1}{c^2} \alpha_p E_0 \frac{4\pi^2 c^2}{r\lambda^2} \sin(\theta_z) \cos\left(\frac{2\pi ct}{\lambda}\right) \quad (26)$$

Scattered light measuring equipment is typically only sensitive to the intensity of light which is equal to the amplitude of the electromagnetic field squared. Thus squaring Equation (26) gives the intensity of scattered light at  $r$  and  $\theta_z$

$$I_s = I_{0z} \alpha_p^2 E_0^2 \frac{16\pi^4}{r^2 \lambda^4} (\sin(\theta_z))^2 \quad (27)$$

where  $I_{0z}$  is the intensity of the  $z$  polarized light,  $I_{0z} = E_0^2$ . Hence, Rayleigh concluded that the intensity of the scattered light was proportional to  $1/\lambda^4$  and therefore short wavelength light scatters more than long wavelength light.

For the case where Rayleigh theory does not apply, i.e., the particle cannot be considered small when compared to the incident wavelength, then the scatter can arise from different parts of the particle. These scattering centers located across the particle force the incident light to take different routes before reaching the detector. This difference in path lengths can lead to destructive interference that reduces the intensity of the scattered light. If the atoms are arrayed in a far more orderly fashion in a dense media (like in liquids and solids), then the light beam effectively encounters a uniform medium with no discontinuities to destroy the symmetry and the scattered wavelets interfere constructively in the forward direction but destructive interference predominates in all other directions. So, little or no light ends up scattered laterally or backwards in a thick homogeneous medium [36].

### ***Diffraction***

Diffraction arises from the interaction of electromagnetic waves with some sort of physical obstruction like antiphase boundaries on GaAs. When a small aperture at  $\Sigma$  is illuminated by plane waves from a very distant source,  $S$ , and the plane of observation,  $P$  is also at a great distance, then the projected pattern spreads out considerably and bears little resemblance to the actual aperture. This is known as Fraunhofer or far-field diffraction. This diffraction occurs at an aperture of greatest width  $a$  when  $R > a^2/\lambda$ , where  $R$  is the smaller of the two distances from  $S$  to  $\Sigma$  and  $\Sigma$  to  $P$ . The CASI setup explained in the next chapter satisfies this condition; hence, I only discuss Fraunhofer diffraction in this thesis. Using the Huygens-Fresnel Principle for a long slit whose width is much less than  $\lambda$  and is illuminated by plane waves, the slit is considered a line source of electron oscillators where each point emits a spherical wavelet given by,

$$E = \left(\frac{\varepsilon_0}{r}\right) \sin(\omega t - kr) \quad (28)$$

where  $\varepsilon_0$  is the source strength. For a continuous line source where  $D$  is the entire length of the array, and  $\varepsilon_L$  is the source strength per unit length, the net field is given by,

$$E = \varepsilon_L \int_{-\frac{D}{2}}^{\frac{D}{2}} \frac{\sin(\omega t - kr)}{r} dy \quad (29)$$

The procedure for obtaining the irradiance function for a monochromatic wave diffracted by many slits as laid out in Hecht, takes the integral from above and applies the Fraunhofer condition to it, by which the distance to the point of observation,  $r$ , can be written as a linear function of the aperture variables. The flux density distribution function from all the slits is then given by

$$I(\theta) = I_0 \left(\frac{\sin \beta}{\beta}\right)^2 \left(\frac{\sin N\alpha}{\sin \alpha}\right)^2 \quad (30)$$

where  $\beta = (kb/2) \sin \theta$  and  $\alpha = (ka/2) \sin \theta$ . The width of the slits is  $b$ , center-to-center separation between them is  $a$  and  $\theta$  is angle between the point of observation,  $P$ , and the normal to the plane containing the slits. The principal maxima occur when  $\frac{\sin N\alpha}{\sin \alpha} = N$ , that is, when  $\alpha = 1, \pm\pi, \pm2\pi, \dots$  or equivalently,

$$a \sin(\theta_m) = m\lambda \quad (31)$$

with  $m = 0, \pm 1, \pm 2, \dots$ . Minima of zero flux density exist whenever  $\left(\frac{\sin N\alpha}{\sin \alpha}\right)^2 = 0$  or when  $\alpha = \pm \frac{\pi}{N}, \pm \frac{2\pi}{N}, \dots, \pm \frac{(N+1)\pi}{N}, \dots$ . Between consecutive principal maxima, there are  $N-1$  minima and some subsidiary maximum between each pair of minima.

### III. Methodology

#### OPGaAs Samples

Samples available for testing are listed in Table 2 along with their carrier concentrations, thickness and mass. Samples were provided by Air Force Research Lab-RY branch. While the template for some of the patterned samples was sourced from outside the facility, all HVPE thick-layer growth was performed by Air Force Research Lab, AFRL/RYP, currently located at Wright Patterson AFB, Ohio. Some samples were grown at different times under slightly different conditions as growth techniques evolved and thicker growth of the patterned material was achieved. Thickness measurement includes only the orientation patterned growth for OPGaAs samples, not the substrate.

GaAs sample preparation involves cutting and polishing the sample. A wet wire saw STX-202 was used for cutting the samples to desired dimensions. Then the samples were polished on a quartz plate using alumina slurry of grit sizes varying from 3-20  $\mu\text{m}$ . The samples were mounted to the brass polishing holder using crystal bond and polishing was done manually by making figure 8's on the plate to ensure a uniform polish. After removing the substrate from the samples, a chemical mechanical polish (CMP) was performed to obtain a final glossy finish. This entails replacing alumina with a CMP polish slurry containing 50 ml colloidal silica, 200 ml deionized water and 30 ml bleach. Only samples 4, 5, 9, and 10 were polished on both sides. The purpose of the polishing is to produce a smooth surface for bulk scattering measurements and to decrease surface absorption effects during laser calorimetry.

**Table 2: Description of samples used for laser calorimetry.**

Sample Name (Growth Date)	Carrier Concentration (cm <sup>-3</sup> )	Thickness (mm)	Mass (gm)
F 5-11-11	$4 \times 10^{17}$	0.50	0.1228
F 4-26-11 R1	$5 \times 10^{15}$	0.70	0.1698
B 9-23-10	$5 \times 10^{15}$	0.52	0.1150
GaP wafer	Unknown	0.30	0.0874
HVPE grown GaP	Unknown	0.35	0.0939
Fe <sup>2+</sup> ZnSe 015	$4.6 \times 10^{18}$	1.62	0.5721
Fe <sup>2+</sup> ZnSe 016	$8.3 \times 10^{18}$	1.85	0.3198

Samples F 5-11-11 and F 4-26-11 are orientation patterned as seen in Figure 12.

These domains of alternate phase were deliberately induced to achieve QPM. The thickness listed refers to the epitaxially grown material.

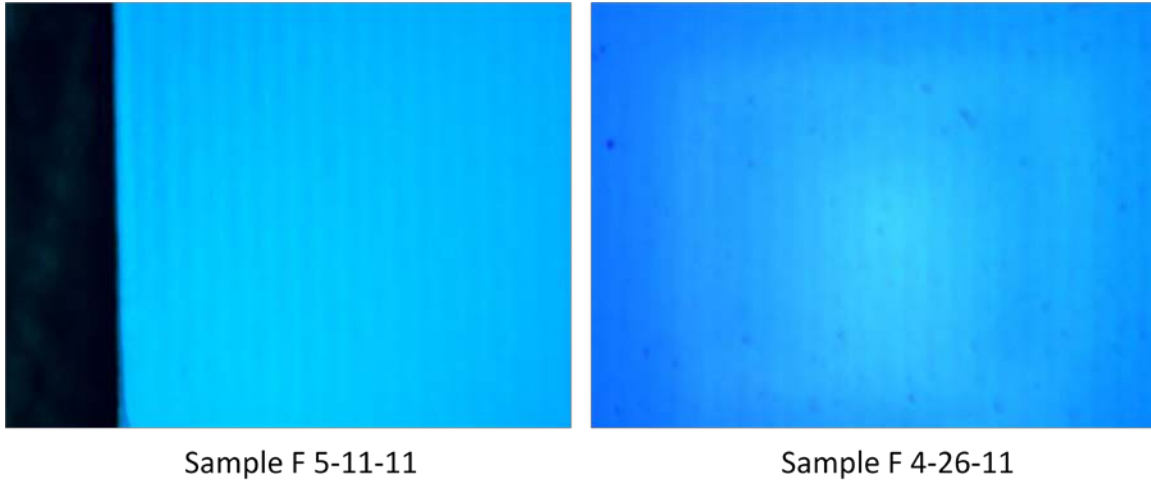


**Figure 13: OPGaAs samples observed under a Nikon Nomarski microscope at 5x magnification after chemical mechanical polishing. Orientation pattern domains (with a period of 100  $\mu$ m) are visible. HVPE thick layer growth was performed on templates at AFRL.**

## Laser Calorimetry Experiment

A THOR Labs ITC 4001 Laser diode with a 1625 nm, 50 mW fiber pigtail was used as the source for all the samples. The output wavelength was fixed while the output power was adjusted with the current setting of the laser diode. The power output had a range from 2-50 mW. A converging lens made from  $\text{CaF}_2$  was used between the laser source and the sample as seen in Figure 14 to get a beam size of 518 microns on the sample. A THOR Labs beam profiler was used to find this beam size. Also a calibrated Newport Power Meter and detector were used to find the new reduced laser output at the sample due to the lens.

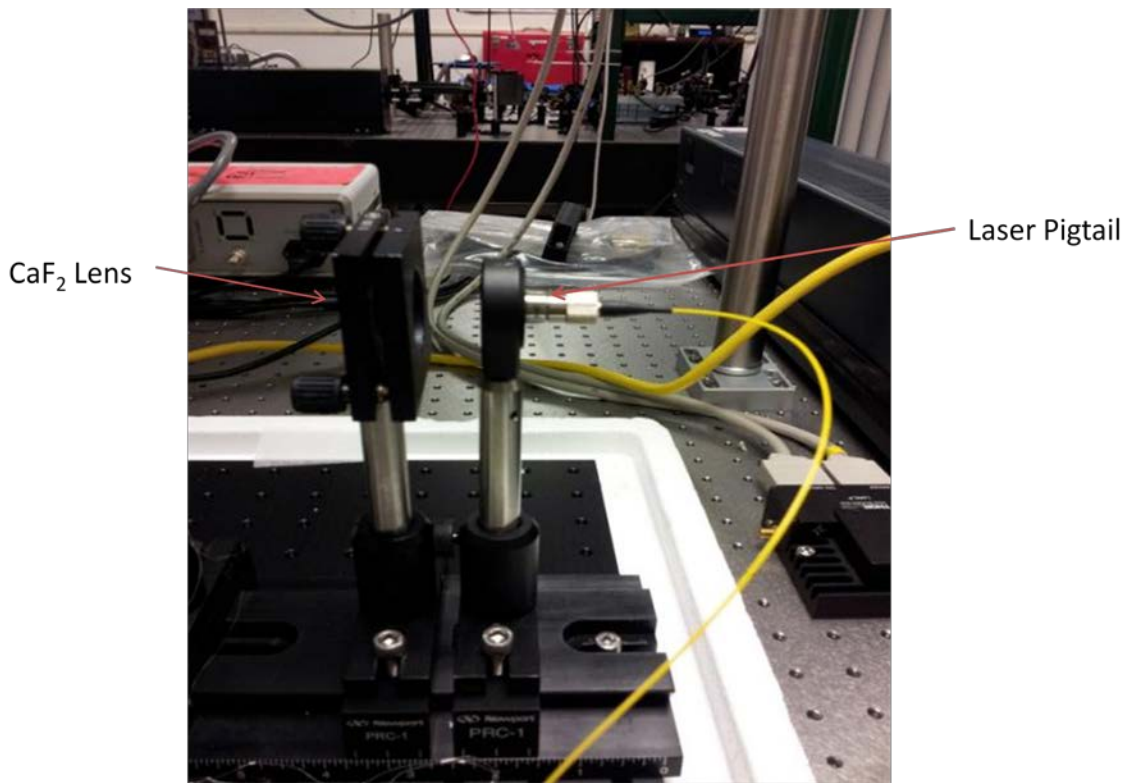


**Figure 14:** Setup of source for laser calorimetry. A THOR LABS ITC 4001 Laser diode connected to a 1625 nm, 50 mW fiber pigtail. A  $\text{CaF}_2$  converging lens is placed in front to achieve the spot size of 518  $\mu\text{m}$ .

The sample is glued to the edge of a nylon string with minimal amounts of Rubber Cement and is made to hang from the sample holder as shown in Figure 15. This mounting technique ensures minimal additional thermal mass is attached to the sample. The mounting also avoids the sample from making any undesirable contact with other instruments in the apparatus. Two strings going across the sample holder at the bottom help in keeping the sample face perpendicular to the incoming laser direction. The thermocouple is also slipped between one of the bottom strings and the sample. This helps in maintaining a stable contact between the sample and the sensor while negating the use of any adhesives between the sensor and the sample. Absence of adhesives in making this contact helps in improving the temporal response of the measurement and obtaining more precise readings as the thermal mass of the sample remains the same. A similar sample holder is used and mounting procedure is repeated for the reference sample. A GaAs wafer polished on both sides is used as a reference for all the measured samples. This sample is placed in similar surroundings to provide an accurate reference temperature.



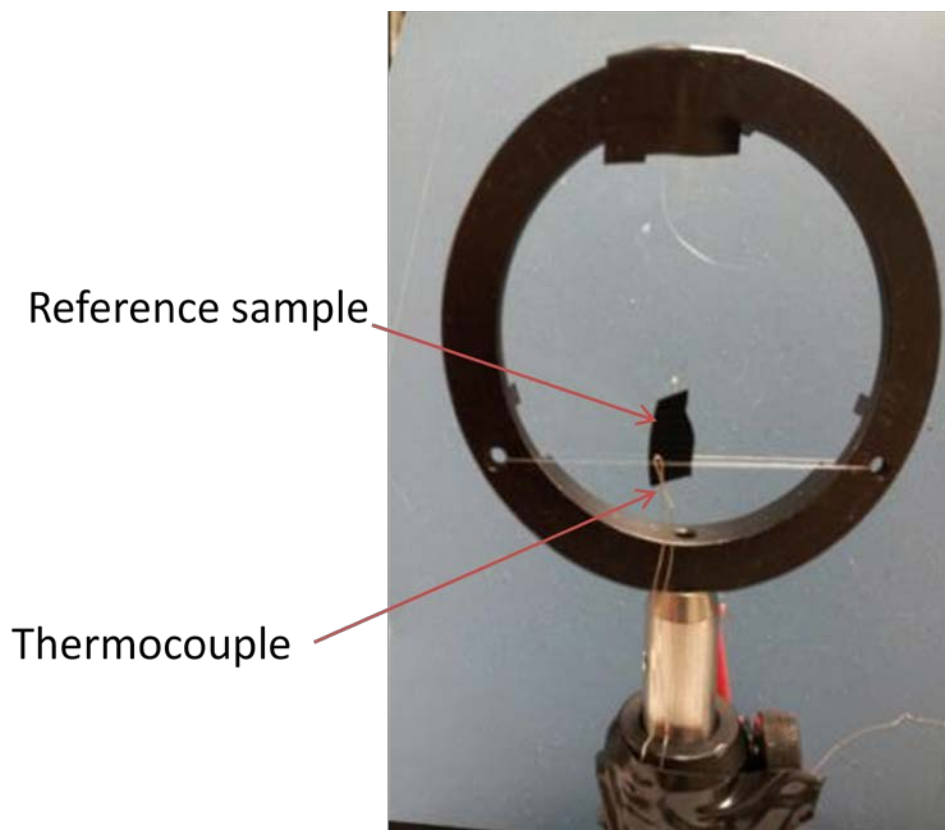


**Figure 15: Sample mount with reference sample hanging on a nylon string. A thermocouple is slipped between the bottom string and the sample.**

Both the sample holders, laser source (pigtail), and the lens setup are enclosed in a Styrofoam box as shown in Figure 16 for better thermal insulation. Small holes for access are made to the side of the box for the pigtail and thermocouple wires. Thermal insulation significance provided by the Styrofoam box is clearly illustrated in Figure 17. Successive runs were conducted on a  $\text{Fe}^{2+}\text{ZnSe}$  sample with open and closed lid. Open lid measurement proved unreliable and change in sample temperature is hard to detect precisely.



**Figure 16:** Laser pigtail source, lens and sample holders are enclosed in a Styrofoam box for better insulation. Small holes are made to the side of the box to attach connectors from the Keithley meter to the thermocouple wires.

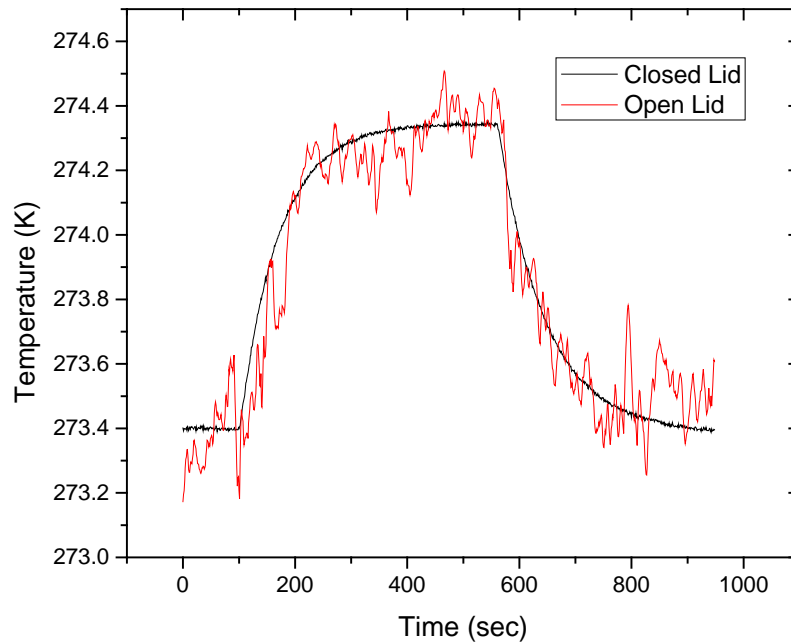


**Figure 17:** Thermal insulation provided by the Styrofoam box. Successive runs were conducted on a  $\text{Fe}^{2+}\text{ZnSe}$  sample with open and closed lid. Open lid measurement proved unreliable and change in sample temperature is hard to detect precisely.

An Omega Type E unsheathed CHROMEGA Constantan thermocouple was used for temperature measurement. Both the reference and measured thermocouple wires are connected to obtain a differential temperature measurement. A Keithley 2700 Digital Multimeter is used to convert the differential voltage between the thermocouples to temperature. An ExcelLINX program that accompanied the multimeter is used to record and display the data in Microsoft Excel. Operating instructions for this software are explained in detail in Appendix B and an image of the graphical user interface is shown in Figure 18.

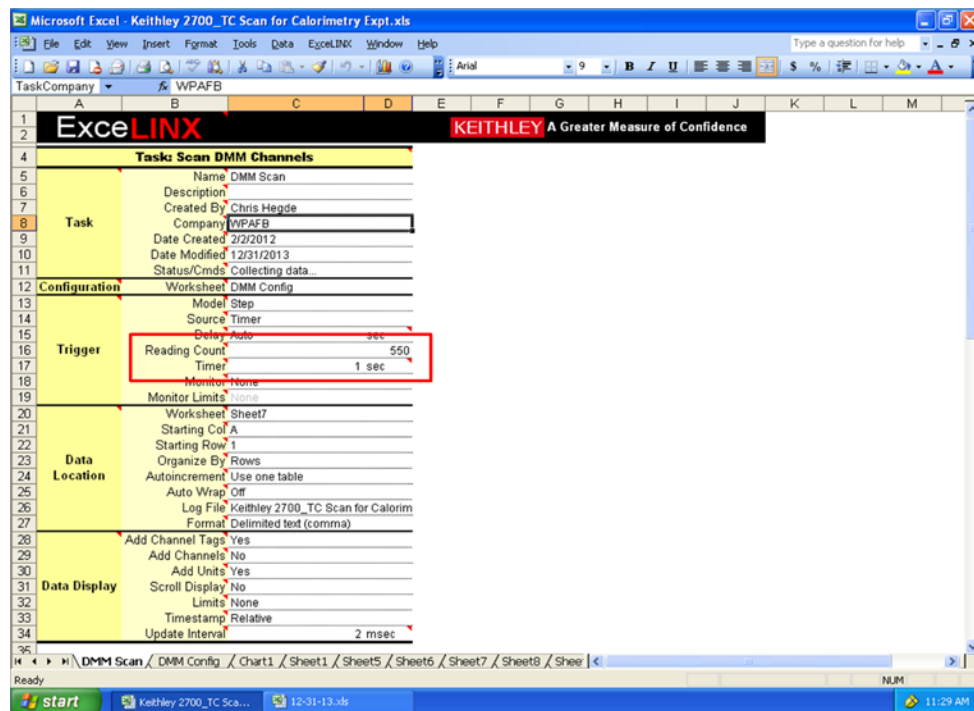


**Figure 18:** ExcelLINX computer software was used with the Keithley multimeter to record and display the change in temperature versus time of the sample. Data gets saved to an excel file for further processing. Some important functions include the 'Reading Count' which allows us to set the number of data points desired and 'Timer' is used to set the frequency at which each data point is collected.

For calorimetry experiment, both the reference sample and the measurement sample are mounted as explained above and the laser is aligned so that the beam is

directed on the sample but away from the thermocouple. Then the lid is placed on the optical setup as shown in Figure 19.

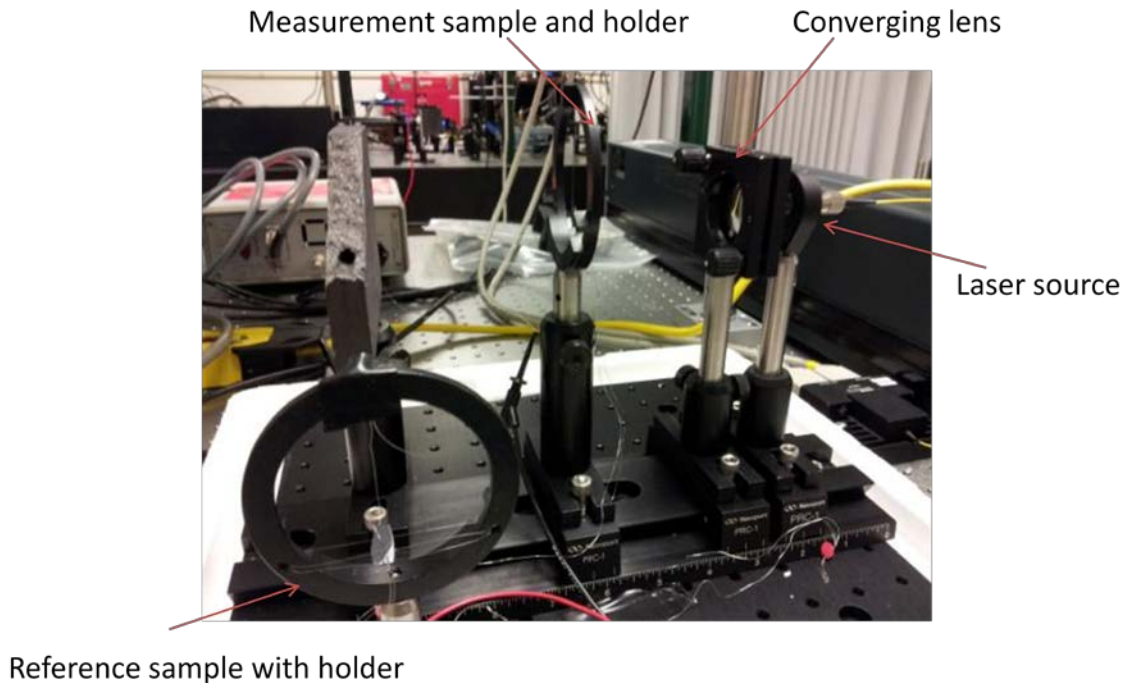


**Figure 19: Optical laser calorimetry setup. This configuration is thermally isolated from the surrounding by enclosing it inside a Styrofoam box.**

All the components so far described for laser calorimetry are displayed in Figure 20. To normalize the temperature inside the box, the setup is left undisturbed for around 45 minutes. Then a typical run of around 550 seconds is initiated using ExcelLINX software as explained in the Appendix B. A representative plot of temperature versus time is shown in Figure 21. The laser is kept on for 250 seconds and then abruptly stopped. The decay curve is fitted to an exponential to obtain a time constant. Also, the absolute difference between the saturation stage temperature and final temperature is found. These values are then used in the expressions explained in Chapter II to obtain the

absorption coefficient of the sample. The representative plot in Figure 21 is an example of a sample measurement where signal is far greater than the noise of the instrument.

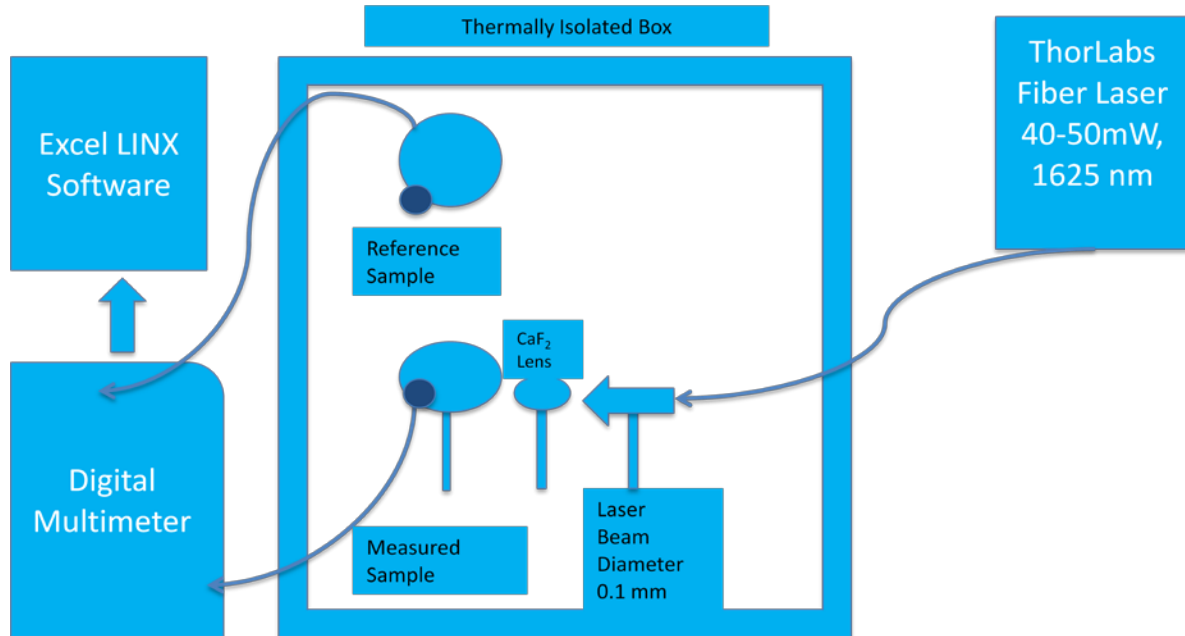


**Figure 20: Complete laser calorimetry setup.** A laser diode is used to irradiate the measurement sample with its change in temperature measured using an OMEGA Type E thermocouple. The difference in voltage between the measured and reference thermocouple is converted to temperature by the Keithley multimeter and data is stored in the Excel LINX software.

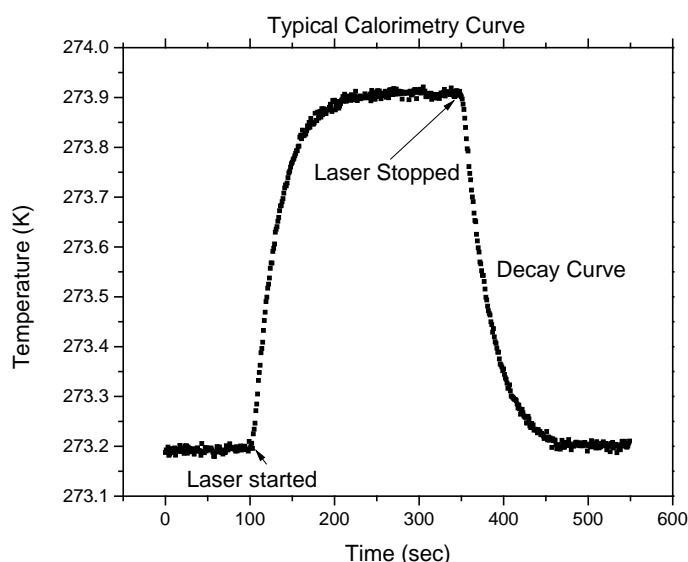


**Figure 21:** A representative plot from the laser calorimetry experiment for a sample where signal is far greater than the instrument noise. The laser is kept on until saturation and then abruptly stopped. The decay curve is fitted to an exponential to obtain the time constant. The absolute change in temperature of the sample of around 0.7 K is also obtained from the plot.

Before initiating the calorimetry measurement it is important to stabilize the temperature inside by waiting long enough after the lid has been placed to ensure uniform sample temperature. Figure 22 shows the change in sample temperature as the ambient temperature inside normalizes. The wait time varies for each time the lid is lifted but at least 45 minutes is recommended from experience. If excessive laser alignment was performed on the sample then a longer wait times is required to bring the sample back to normal initial temperature. Waiting for temperature to normalize inside the Styrofoam box before taking calorimetry measurements results in relatively flat initial curves (Figure 23) that symbolize the stable sample temperature inside. Uniform sample temperature is important in minimizing unnecessary errors while calculating absolute change in temperature.

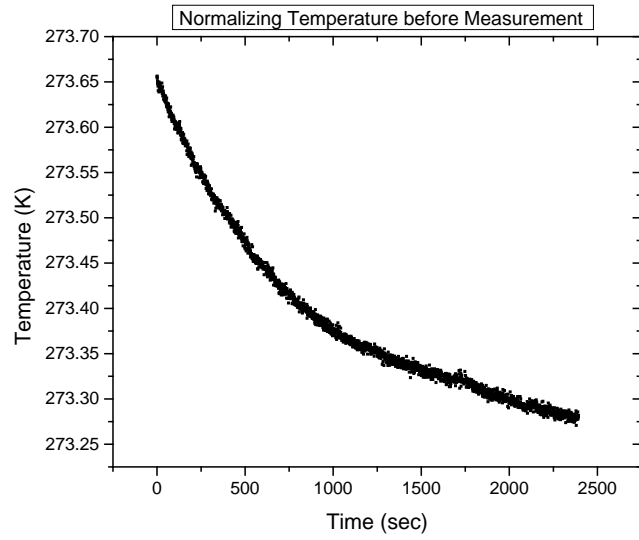


**Figure 22:** Plot of temperature normalizing in the interior of the box as the setup is left undisturbed before a measurement can be taken. The wait time varies for each time the lid is lifted. Note starting temperature is higher than ambient due to rise in sample temperature from laser alignment process.

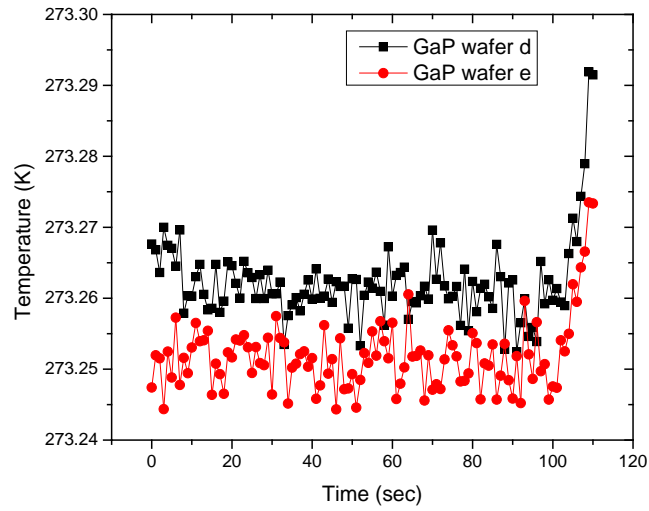


**Figure 23:** Waiting for temperature to normalize inside the Styrofoam box before taking calorimetry measurements results in relatively flat initial curves that symbolize the stable sample temperature inside. Uniform sample temperature is important in minimizing unnecessary errors while calculating absolute change in temperature.

The three different methods available to calculate absorptance (as explained in Chapter II) are utilized on a single set of calorimetry data collected from a GaAs wafer to compare and contrast between them. Figure 24 shows the gradient method which involves taking the slope of the rising and falling curve at the same temperature change. While, Figure 25 shows the summation method applied with the graph of  $B_n$  against  $A_n$  as described in Chapter II. Figure 26 explains the saturation method which uses the decaying part of the data curve to calculate absorptance.

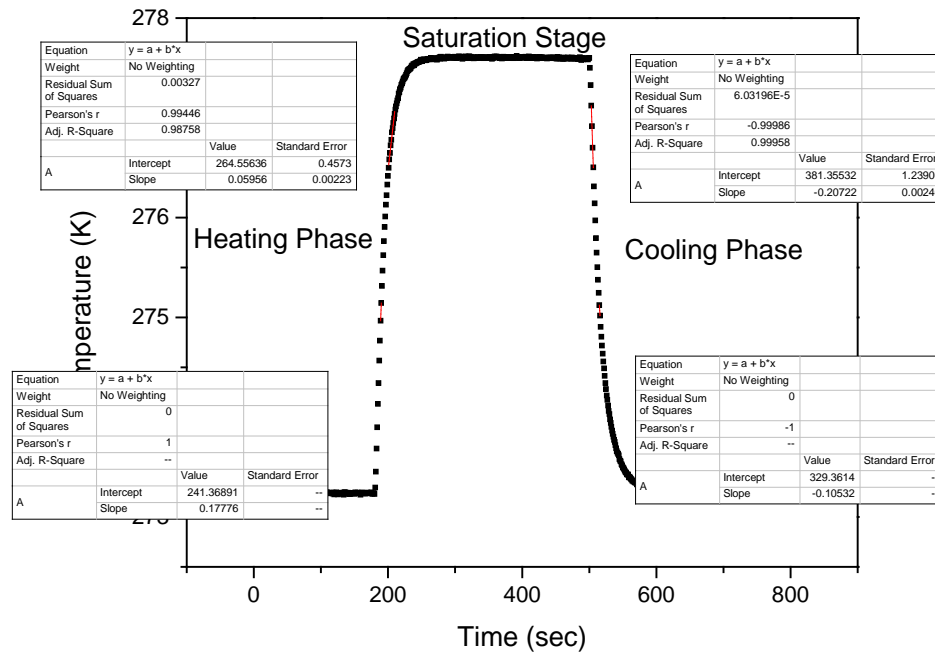


**Figure 24: Gradient method explained in Chapter II, is an alternate technique to recover absorptance. It is applied here to a data set collected from a GaAs wafer of mass 0.09837g.**

The gradient method compares the slopes of the rising and falling curves provided both points have the same absolute change in sample temperatures. Then according to Equation (20), the absorptance can be found by solving for  $a$ ,  $\frac{mc_p}{P} \left( \frac{d}{dt} \Delta T(t_h) - \right.$



$\frac{d}{dt} \Delta T(t_c) \approx a = 0.33$  (upper set of slopes),  $0.35$  (lower set of slopes). The

advantages of the methods lie in the simplicity of simply finding the slopes and finding the associated absorptance. Some disadvantages of this method can include the variation in absorptance values depending on the set of points used to calculate the slope as seen in our case. Also, it is important to note that the GaAs wafer used was particularly lossy, so the big change in sample temperature made it easier to calculate the slopes. Determining slopes with accuracy, can be difficult for measurements when the sample has exceptionally low loss and hence the change in temperature is not as big.

**Table: 3: Data rows during saturation stage describing the summation method of determining absorptance, used here on a GaAs wafer of mass 0.09837g. The 'Temperature' and 'Time' columns obtained using a Keithley multimeter are used to find the quantities, 'A<sub>n</sub>' and 'B<sub>n</sub>' (shaded columns below) as explained in Chapter II. Note  $t$  is the time while  $T$  is the temperature of sample.**

Temp. (K)	Time (sec)	$\left(\frac{P_i + P_{i-1}}{2}\right) * (t_i - t_{i-1})$	$A_n$	$\left(\frac{T_i + T_{i-1}}{2} - T_0\right)$	$(T_n - T_0)$	$\left(\left(\frac{T_i + T_{i-1}}{2} - T_0\right)(t_i - t_{i-1}) + (T_n - T_0)\right)$	$B_n$
277.603	477	0.04	11.90	4.360	4.363	8.72	143.9
277.598	478	0.04	11.94	4.360	4.358	8.72	144.4
277.596	479	0.04	11.98	4.357	4.356	8.71	144.9

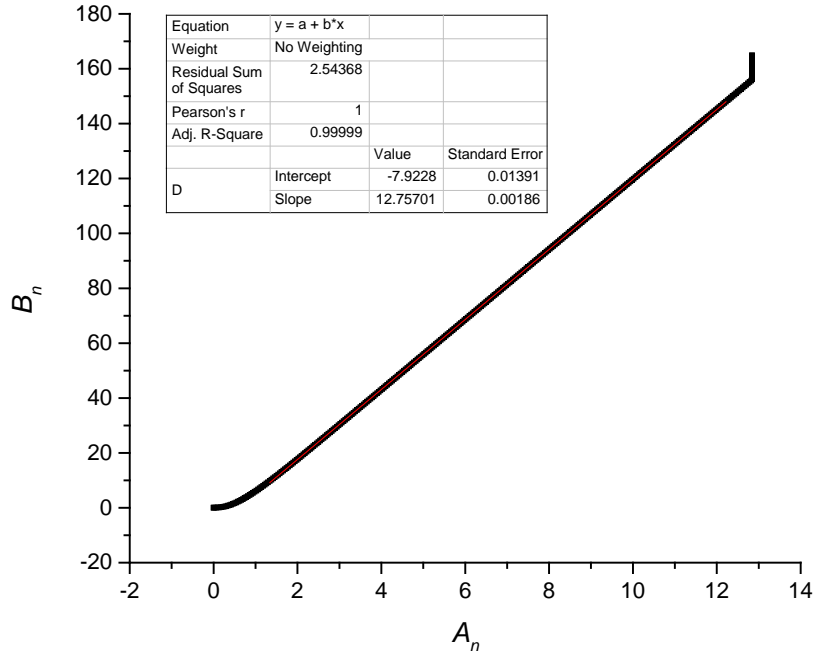


**Figure 25: Summation method explained in chapter II as an alternate technique to recover absorptance. It is applied here to a data set collected from a GaAs wafer with mass 0.09837g. As explained in Chapter II, the gradient of the  $A_n$  versus  $B_n$  curve is equated to the quantity,  $a/(mc_p)$  where,  $a$  is the absorptance,  $m$  is the mass,  $c_p$  is the specific heat of the sample.**

Applying the summation method as explained in Chapter II, the absorptance can be found by solving for  $a$  in:  $(slope)mc_p = a = 0.44$ . Due to the level of complexity in finding the summation values and the possible change in these values between successive runs with changes in 'laser start' and 'stop' times deterred the further use of this method.

Figure 26 explains the use of the saturation method where the decaying part of the data set is plotted and an exponential fit is used to obtain the decay constant ( $tI$ ). This quantity along with the absolute change in sample temperature ( $\Delta T$ ) are used to obtain absorptance,  $a = \left( \frac{\Delta T mc_p}{P(t1)} \right) \approx 0.31$ . This simplified method was chosen to calculate

absorptance for all the samples evaluated in this thesis. Requirement of reaching a saturation point before the laser is turned off produced similar absorptance values between runs and provided consistency.

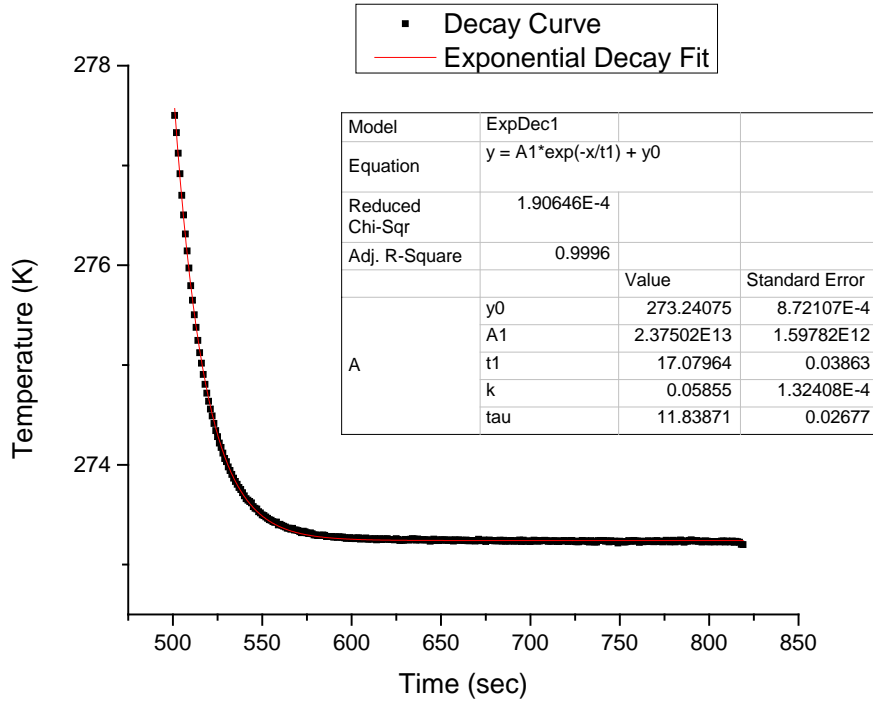


**Figure 26:** Saturation method as explained in Chapter II is applied to a data set recorded using a GaAs wafer of mass 0.09837 g. Points collected after the laser is turned off are plotted and fitted to a decaying exponential to obtain the decay constant ('t1' above in the box). This quantity along with the absolute change in temperature,  $\Delta T$ , are used to obtain absorptance.

## CASI Measurements

The Complete Angle Scatter Instrument (CASI) measures the scattering of incident light in all directions for both the transmission and reflection hemispheres. Such data can provide insight about the possible relationship of incident direction with loss in materials. To do this, CASI directs laser light (544 nm, 633 nm, 3.39  $\mu\text{m}$ , or 10.6  $\mu\text{m}$ ) from a source box onto a sample mounted on a stage as shown in Figure 27. Light

transmitted and reflected from the sample surface in the plane of incidence is collected by an aperture and measured by a single element photodetector mounted on an arm that sweeps out a full arc around the sample. Six Daylight Solutions tunable, external-cavity quantum cascade lasers (EC-QCL's) are also incorporated into the CASI. The six EC-QCL's span mid wave IR wavelength from 4.37-6.54 $\mu\text{m}$  and long-wave IR wavelengths from 7.41-9.71 $\mu\text{m}$  [37]. Signal detection can be improved by adjusting the output power of the EC-QCL's.

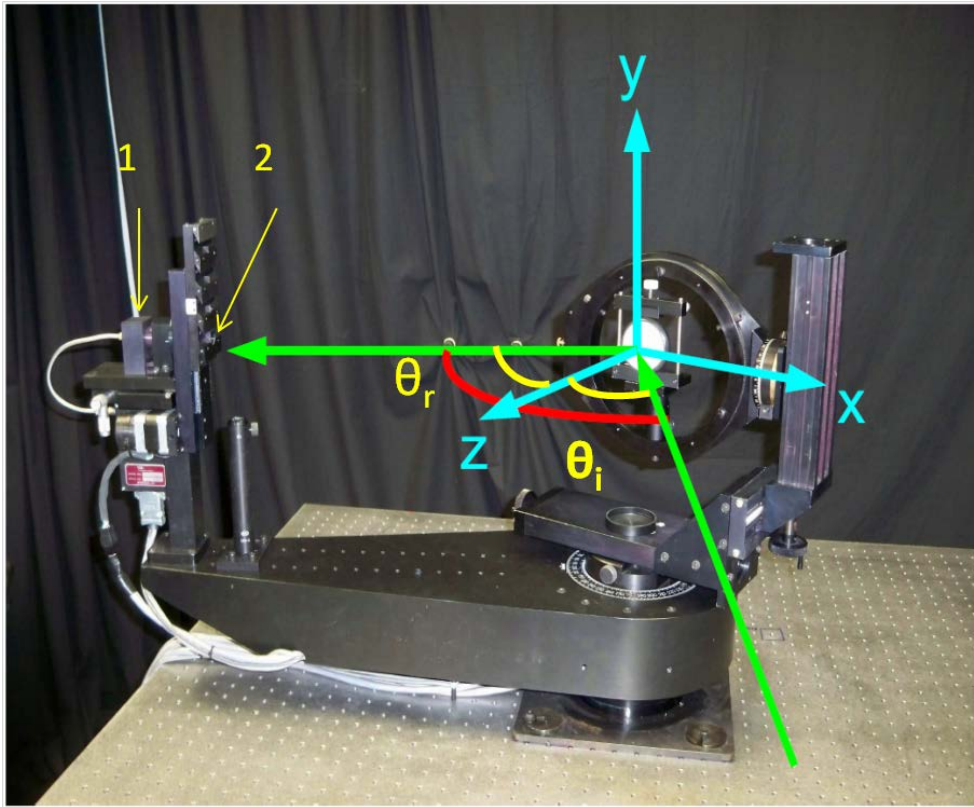


**Figure 27: AFIT's CASI.** The green ray represents the laser beam path incident on the white sample with an incident angle  $\theta_i$ . The detector (1) moves around the sample in the same plane as the incident ray to collect  $\theta_r$ . A variable aperture (2) is available to achieve improved signal detection. Incident angle can be adjusted by moving the sample about the y-axis. The incident beam width is narrow at the sample and is focused on the detector.

An EC-QCL at 8.15  $\mu\text{m}$  was used for scattering measurements from OPGaAs samples in this thesis. The CASI software assumes it is making an in-plane measurement so the incident beam and the reflected beam stays in the x-z plane of Figure 27. Therefore, only  $\theta_i$ , the angle between the z-axis and the incident beam, and  $\theta_r$ , the angle between the z-axis and detector, are varied in the measurement. Angle of incidence was kept normal for all the measurements while  $\theta_r$  went from 0 to 180 degrees for each transmission measurement. The single element photodetector takes flux (power) measurements in an arc around the sample illuminated by a laser. The incident laser beam was parallel to the laboratory horizontal or *p*-polarization.

### **FTIR Measurements**

The apparatus in Figure 28 was used to measure polarization-dependent loss in patterned GaAs. A BOMEM FTIR was used and a Thor Labs BaF<sub>2</sub> holographic wire grid polarizer was placed in front of this source. The polarizer was adjusted for maximum signal at the detector and then kept constant for the entire experiment. After taking a background file in this configuration, the sample fixed to a dial (Figure 29) was placed in between the polarizer and the detector. Using the same background file each time, the sample was rotated by five degree increments and transmission measurements were carried out for each position from 0 to 360 degrees.

The FTIR source was maintained at a constant intensity by keeping the polarizer at the maximum position throughout the experiment. The source spot on the sample was also unchanged as the sample holder was clamped down while rotating between runs.

Consequently, any change in detected intensity can be related to the polarization loss caused by the sample.

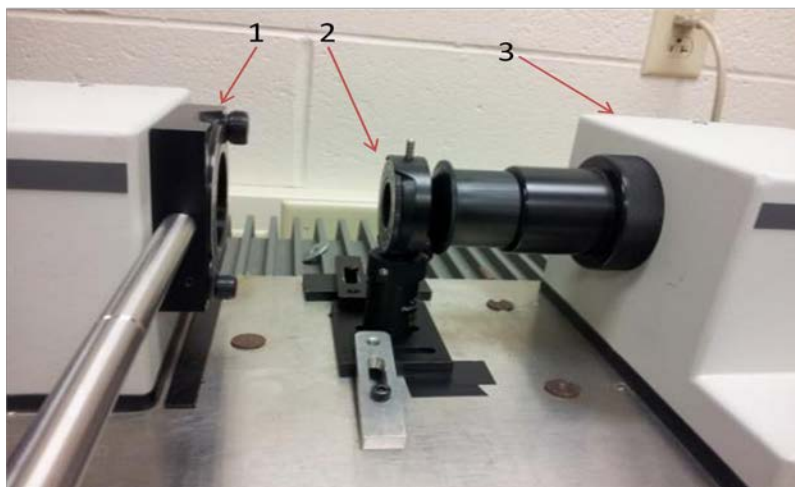


**Figure 28: Polarization dependent loss setup for OPGaAs. A wire grid polarizer (1) is placed in front of a BOMEM FTIR and the sample is fixed to a dial (2) before the FTIR detector (3).**



**Figure 29: Sample mounted to the dial (Part 2 from Figure 28). Transmission measurements were taken as the dial was gently rotated by five degree increments.**

## **Summary**

While optical loss in III-V materials can be attributed to many sources, experiments in this thesis were planned to look at only a few of these due to time constraints. Primary areas of interest here were divided into absorption loss, orientation pattern related loss and polarization loss. Laser calorimetry tool was formulated to understand and detect absorption losses in III-V materials. The AFIT CASI experiment was organized to look at any preferential scattering from orientation patterns deliberately induced in GaAs to achieve QPM. Finally, the FTIR experiment was planned to relate transmission loss in sample to polarization of incident light.

## IV. Results and Analysis

### Chapter Overview

The following sections provide results and analysis of the measurements conducted in this thesis. Absorption measurements conducted on GaAs, GaP and Fe<sup>2+</sup>ZnSe samples using laser calorimetry and related troubleshooting of the procedure are provided in the first section. CASI data with analysis is presented next, and polarization loss data obtained using FTIR experiments are described last.

### Laser Calorimetry

Thermal isolation of the experimental setup from outside temperature drifts is critical for accurate measurement. The sensitivity of the calorimeter system is restricted by the smallest temperature rise that can be reliably measured for a given time interval. Thermocouple readings were investigated for long period in the absence of an active laser source. Figure 30 shows the fluctuations in temperature measured by the thermocouple were approximately 40 mK over a few hours. A typical measurement of the sample weighing around 0.2 gm takes about nine minutes, with a typical temperature change,  $\Delta T \approx 1$  K. Within this short time frame, the minute temperature variation inside the calorimetry housing can be considered negligible. Such degree of thermal stability proves useful when the sample has minimal loss or when the applied laser power is small and hence the absolute temperature rise produced by the laser maybe on the order of thermal noise. The offset between the two thermocouples in Figure 30 from the zero temperature change (273.15° in Kelvin) minimizes over time as the temperature inside



the calorimeter normalizes. Therefore, it is vital to wait for at least 45 minutes after the lid is closed before starting the data acquisition process.

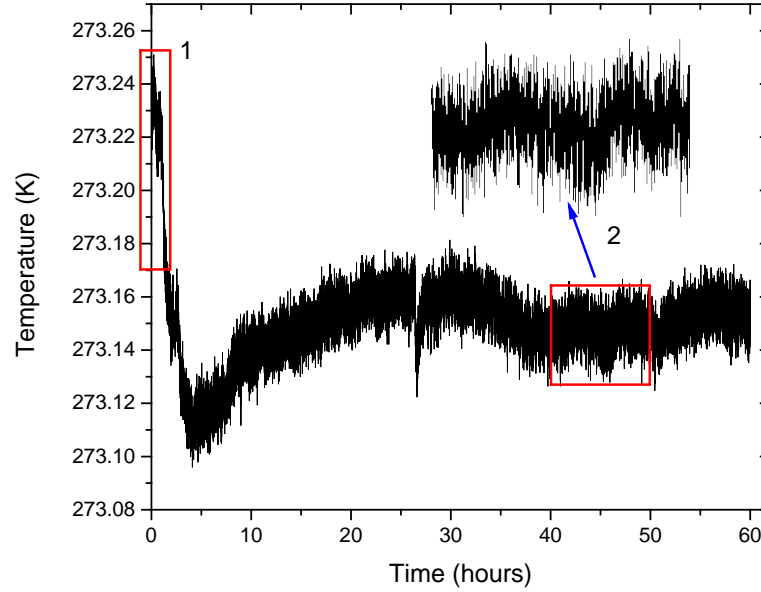


**Figure 30: Insulation provided by the Styrofoam box from outside temperature drifts. Temperature excursions are kept to a minimum and this results in increased sensitivity of the measurement. There is an initial normalization (Box 1), of temperature inside the box as discussed earlier in Figure 22, after which the fluctuations in temperature measured by the thermocouple (Box 2), are approximately given by,  $\Delta T \approx 273.17\text{K} - 273.13\text{K} = 0.04\text{K}$ .**

Once the system was verified to have good thermal insulation, some initial measurements were taken to verify the theoretical concepts of Chapter II. Calorimetry measurements were taken with a GaAs wafer to verify the linear relationship between change in temperature of the sample and the applied power as explained in Equation (13) of Chapter II. Figure 31 shows the data collected from the sample along with a linear fit. The relationship behaves as expected in the limits of power used throughout the experiments as can be seen by simplifying Equation (13) to get,  $\frac{dT}{dP} = \text{constant}$ .

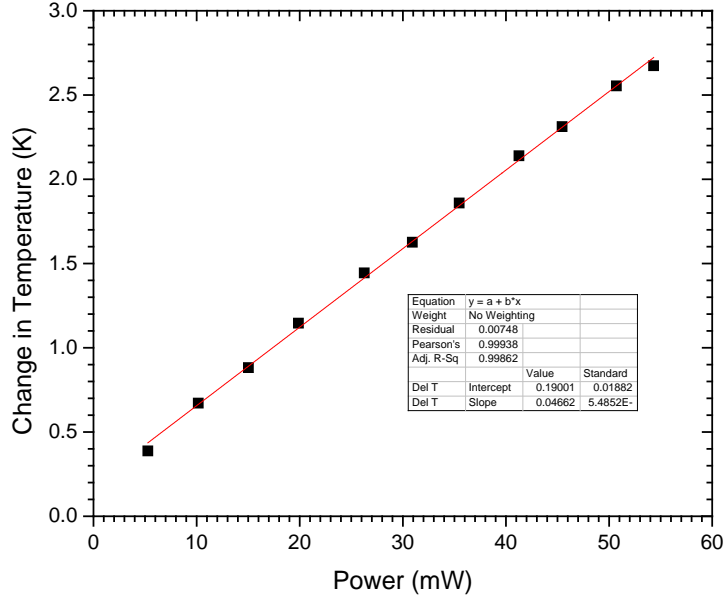


**Figure 31: Laser calorimetry data from a GaAs wafer to observe the relationship between the absolute change in temperature of the sample and the applied power. A linear fit of the data is also shown with a slope of 0.05 and a y-intercept of 0.19.. The laser was operating at 1625 nm.**

After the power and absolute change in temperature relationship was verified, the reflectivity of the laser power from the sample surface was derived from Fresnel's Equations [38]. As the fraction of intensity transmitted by the sample is incident angle dependent and is a maximum at normal incidence, calorimetry measurements were taken with the sample as close to normal to the pump beam as possible. The normal reflection coefficient,  $R$ , is then dependent upon the indices of refraction of the ambient and sample media. Taking the index of refraction of air at STP as 1.000277 ( $n_1$ ) and that of GaAs at 1625 nm as 3.39 ( $n_2$ ), the reflectivity,  $R$  was found to be 29.6% as shown in Equation (32) [27],

$$R_{GaAs} = \left( \frac{n_2 - n_1}{n_2 + n_1} \right)^2 = 29.6\% \quad (32)$$

Similar calculation was also performed for GaP and ZnSe samples with  $n_{GaP} = 3.05$ ,  $n_{ZnSe} = 2.44$  to obtain  $R_{GaP} = 25.6\%$  and  $R_{ZnSe} = 17.6\%$ . Since all the samples measured were not AR coated, this reflection loss was accounted by subtracting it from the applied laser power in the absorbance calculations. This can be justified as only the light that is not reflected at the surface has the potential to be absorbed. Note that the contribution to absorbance from the multiple internal reflections in the medium was taken into account in Chapter II when Equation (19) for absorption coefficient was derived.

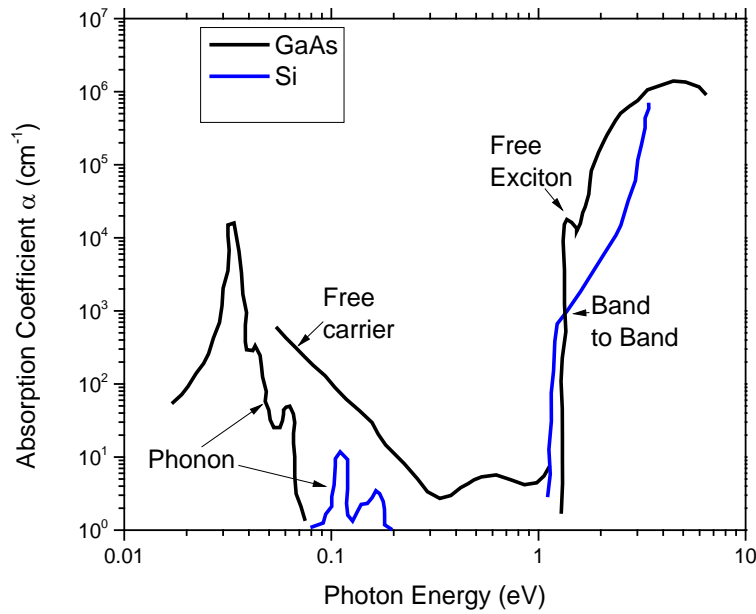


**Figure 32: Observed optical absorption coefficient versus photon energy for Si and GaAs in thermal equilibrium at  $T = 300$  K. Plot was re-drawn and modified using data from [39]. Various mechanisms leading to absorption are shown. The source wavelength for this thesis was 0.76 eV, making free carriers the primary absorbers.**

Various mechanisms leading to absorption are shown in Figure 32 [39].

Interband transitions require higher energy photons to transfer electrons from the valence

band to the conduction band thereby, creating an electron-hole pair. While, phonon transitions occur when long wavelength photons release their energy by directly exciting lattice vibrations. Since the source energy in our case was 0.76 eV, the transition of interest here are the free carrier or intraband transitions. This transition occurs when the absorbed photon imparts its energy to an electron in a given band, causing it to move higher within the same band. Band gap energies for GaAs and GaP are 1.424 eV and 2.26 eV respectively [27]. Figure 33 shows that free carriers are the primary source of absorption below the solid state materials band gap [40].

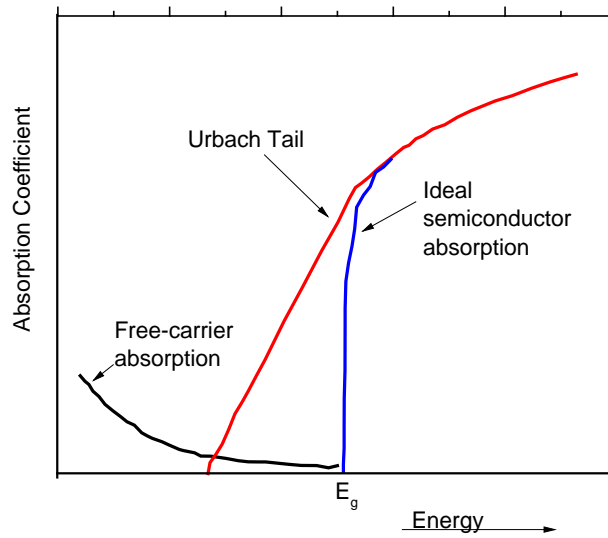


**Figure 33: Change in absorption coefficient of a semi conductor with bandgap energy  $E_g$  versus energy. Plot was re-drawn and modified using data from [40]. Free-carrier absorption dominates at the lower energies used in this thesis.**

Not only do free-carriers play a dominant role in absorption at lower energies, Figure 34 shows that the amount of absorption is proportion to the free carrier concentration in the material [41]. The laser operated at 1625 nm for all the calorimetry

experiments in this thesis so any noticeable change in carrier concentration for similar samples should result in detectable change in absorption.

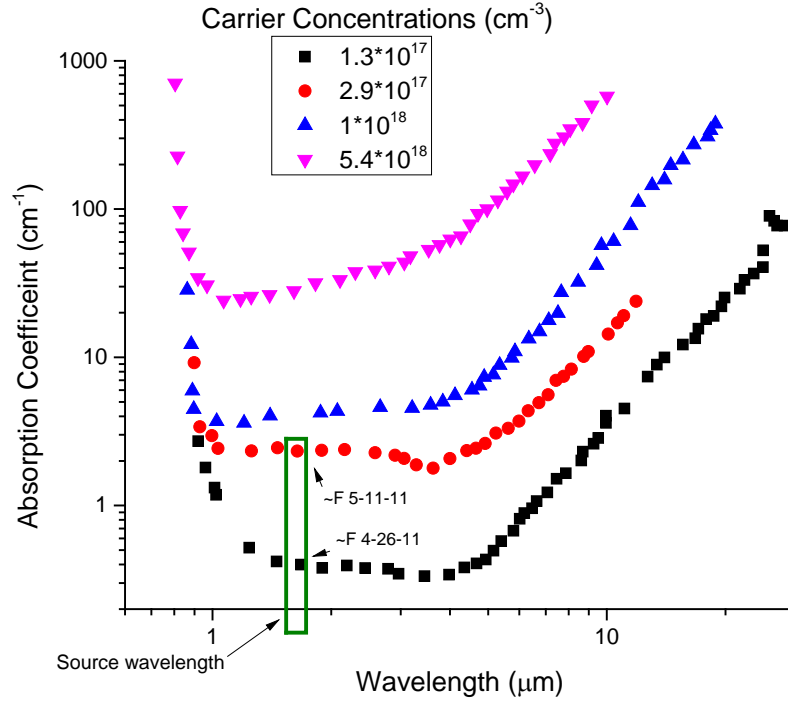


**Figure 34: Free-carrier absorption versus wavelength for different doping levels of GaAs at 296 K. Plot was re-drawn and modified using data from [41]. Conduction electron concentrations (in  $\text{cm}^{-3}$ ) are:  $1.3 \times 10^{17}$ ,  $4.9 \times 10^{17}$ ,  $10^{18}$  and  $5.4 \times 10^{18}$ .**

This relationship between free-carrier concentration and absorption coefficient was inspected in this thesis by measuring the absorption coefficient of two similar ZnSe samples with varying amounts of iron ( $\text{Fe}^{2+}$ ) added as dopants. Both samples were from the same manufacturer and of similar dimensions. As expected, the direct relationship between free-carrier concentration and absorption coefficient was verified and the calorimetry method was validated by measuring (Figure 35) twice the absorption coefficient for the ZnSe sample with higher free-carrier concentration.

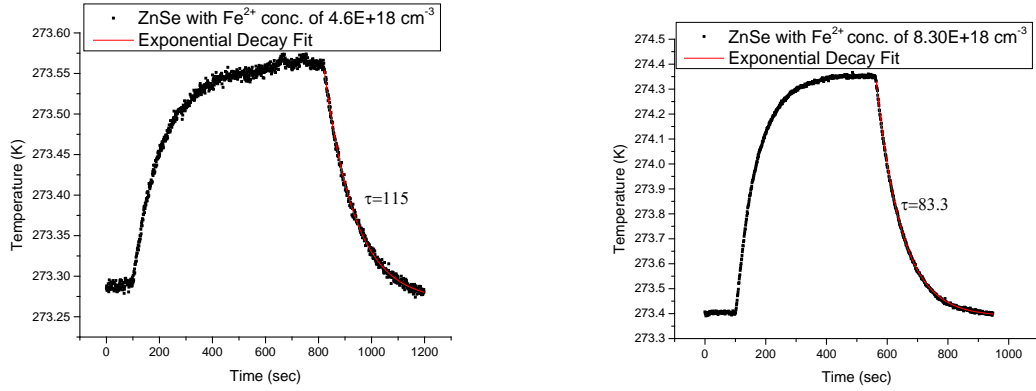


**Figure 35: Comparison between similar ZnSe samples with varying amounts of free-carrier concentrations. As predicted, the sample with higher free-carrier concentration (left), displayed higher absorption.**

During the growth of GaAs films, certain growth processes were altered to enhance impurity concentration and increase the absorption loss of the material. This theory was examined by performing laser calorimetry on two similar OPGaAs samples wherein one of the samples (F 5-11-11) was successfully doped with silicon (Si) impurities during crystal growth. Although, some Si concentration is normal for HVPE grown OPGaAs material, intentional doping with Si can induce free carriers since Si<sub>Ga</sub> is the primary source of donors. Both the samples were polished as discussed before, to avoid the additional loss from the unpolished surfaces in the measurement as we are neglecting surface absorption. Figure 36 shows the calorimetry curves for both the samples. Higher absorption coefficient measured in the impure sample hints towards a direct relationship between excessive dopants to higher absorption loss in the material.

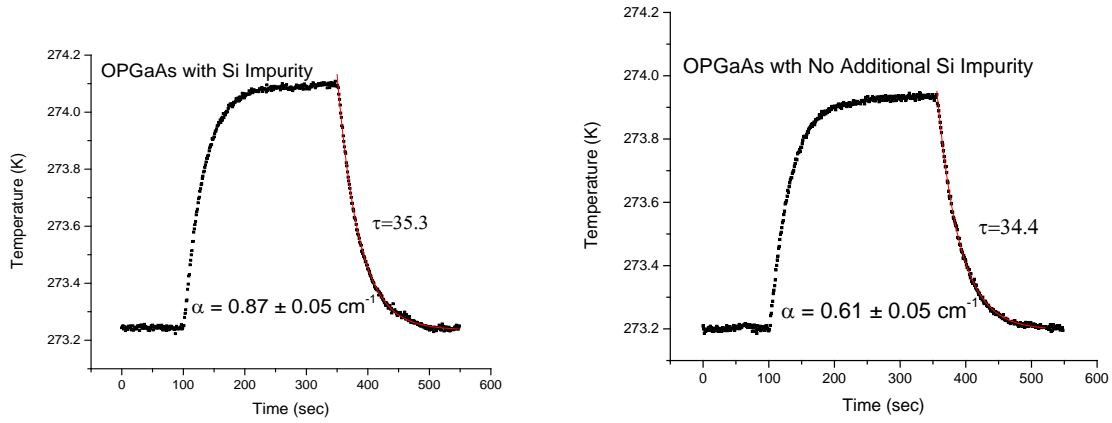


**Figure 36: Laser calorimetry results for two similar OPGaAs samples. One of the samples (left) was intentionally doped with additional Si impurity. Higher absorption coefficient measured in the impure sample hints towards a direct relationship between excessive dopants to higher absorption loss in the material.**

For comparison purposes, two samples of GaP were also measured using laser calorimetry. One of the samples was grown using HVPE technique at AFRL while the other sample was a wafer bought commercially. We have already seen that the GaAs wafer exhibited high absorptance,  $a$ , as compared to HVPE grown OPGaAs when it was used in chapter three to demonstrate the various techniques available to calculate absorptance. Performing a similar comparison for GaP gave the opposite results. Figure 37 shows the calorimetry curves obtained for the two samples. Commercially bought GaP wafer had lower absorption loss than its HVPE grown counterpart. This result can be linked to the possibility that HVPE grown GaP technique is still in its infancy at AFRL.

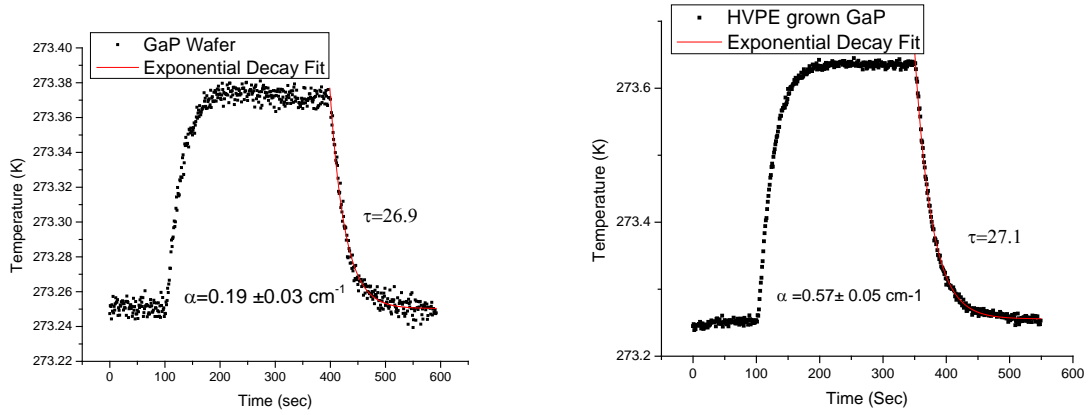


**Figure 37: Calorimetry curves for two GaP samples. The left plot is for a commercially bought wafer while the right plot is for a HVPE grown sample. Commercially bought GaP wafer had lower absorption loss than its HVPE grown counterpart**

Figure 38 displays the measured change in sample temperature throughout the calorimetry cycle for three different runs of OPGaAs with similar configuration. Note the small change in temperature as compared to the other GaAs samples. Limits of the calorimetry method were tested by measuring this very low loss OPGaAs sample successfully. The noise is more prominent in this plot due to the weaker signal and this makes it harder to accurately compute the absolute change in sample temperature.



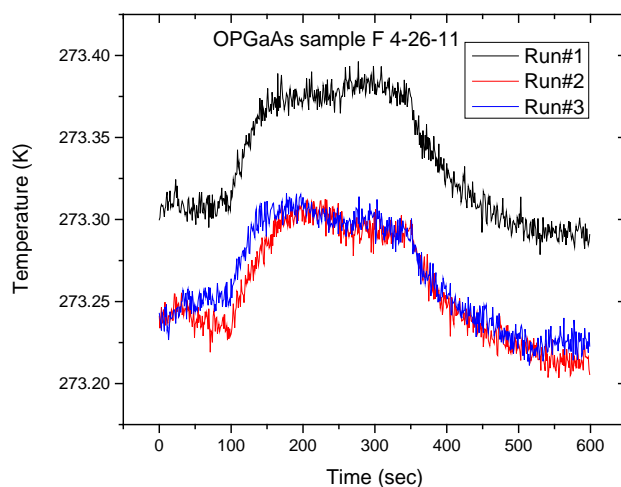


**Figure 38: Change in sample temperature throughout the calorimetry cycle for three different runs with similar configuration. Note the small change in temperature as compared to the other GaAs samples. Limits of the calorimetry method were tested by measuring this very low loss OPGaAs sample successfully. The noise is more prominent in this plot due to the weaker signal and this makes it harder to accurately compute the absolute change in sample temperature.**

Calorimetry measurement data for the various runs conducted for each sample are shown in Appendix A. The time constant was calculated by fitting the cooling curves of each of these runs to a decaying exponential function using 'OriginPro 9'. The absorption coefficients were calculated using Equation (19) for the various runs of the same sample. The average of those runs for each sample is listed in Table 4 and the associated plots are shown in Appendix A. Figure 39 presents the transmission measurements for GaAs and GaP samples using a CARY spectrophotometer.

**Table 4: Absorptance and absorption coefficient at 1.6  $\mu\text{m}$ , found using Equation (19) for all samples.**

Sample	Carrier Concentration ( $\text{cm}^{-3}$ )	Laser Power*(1-Fresnel Reflection Coefficient) (mW)	Absorptance (%)	Absorption Coefficient ( $\text{cm}^{-1}$ )
F 4-26-11	$5*10^{15}$	45(0.704)	$0.18 \pm 0.02$	$0.025 \pm 0.009$
B 9-23-10	$5*10^{15}$	40(0.704)	$3.09 \pm 0.05$	$0.59 \pm 0.08$
F 5-11-11	$4*10^{17}$	40(0.704)	$4.82 \pm 0.08$	$0.80 \pm 0.08$
GaP wafer	Unknown	45(0.744)	$0.56 \pm 0.02$	$0.19 \pm 0.03$
HVPE GaP	Unknown	45(0.744)	$1.96 \pm 0.03$	$0.57 \pm 0.05$
$\text{Fe}^{2+}\text{ZnSe}$ 015	$4.6*10^{18}$	45(0.824)	$1.39 \pm 0.05$	$0.087 \pm 0.005$
$\text{Fe}^{2+}\text{ZnSe}$ 016	$8.3*10^{18}$	45(0.824)	$3.75 \pm 0.02$	$0.21 \pm 0.03$

Absorption coefficient values for B 9-23-10 and F 5-11-11 measured here are a bit higher than those reported in Orchard's paper for a 325  $\mu\text{m}$  untreated (unprocessed wafer i.e. not cleaned with methanol before measurement) GaAs wafer (measured values range from 0.014 to 0.020  $\text{cm}^{-1}$ ) [33]. But absorption coefficient measured for sample F 4-26-11 lies within this range. Absorption coefficient of the other two samples seems comparatively large, but Meyer has reported similar values (ranging from 0.008 to 0.75  $\text{cm}^{-1}$ ) for OPGaAs using an integrating sphere method [6]. Increased absorption in sample F 5-11-11 can also be attributed to the excessive doping of Si in the sample. Although, higher than expected numbers were measured for GaAs samples, laser calorimetry can still be used as a valid loss assessment device. It can be used as a quick and handy tool to compare multiple unpolished samples post-growth to help decide which

sample has a lower absorption loss and is worth spending the extra money to have polishing and AR coating done.

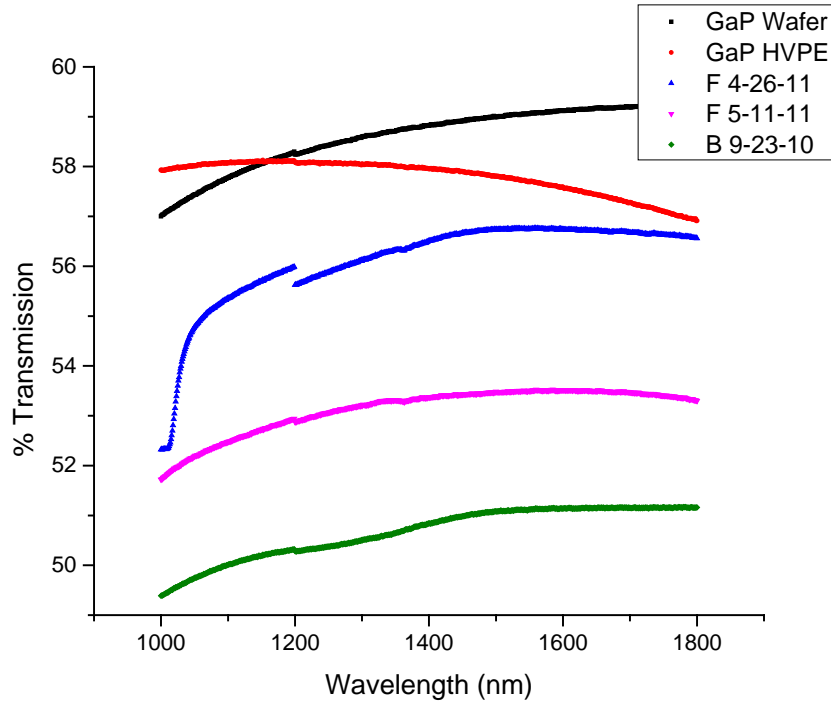


**Figure 39: CARY Spectrophotometer transmission measurement for GaAs and GaP samples. The  $\text{Fe}^{2+}\text{ZnSe}$  samples were sent away to get AR coating done so transmission analysis was not performed on them. Note the kink in the measurement that happens around 1200 nm is due to the spectrophotometer changing the incident lamp (source) internally.**

## CASI

Scattering measurements from two patterned GaAs samples were obtained using a CASI instrument employing a 8.15  $\mu\text{m}$ , 2 mW laser. Samples F 5-11-11 and F 4-26-11 were prepared for CASI measurement by polishing both surfaces. Figure 40 shows the two orientations that were used for each sample to observe any differences in transmission while the incident polarization was kept constant. It should be noted that the free-carrier absorption observed in laser calorimetry at 1.6  $\mu\text{m}$  will be enhanced at 8  $\mu\text{m}$  as shown in Figure 34.

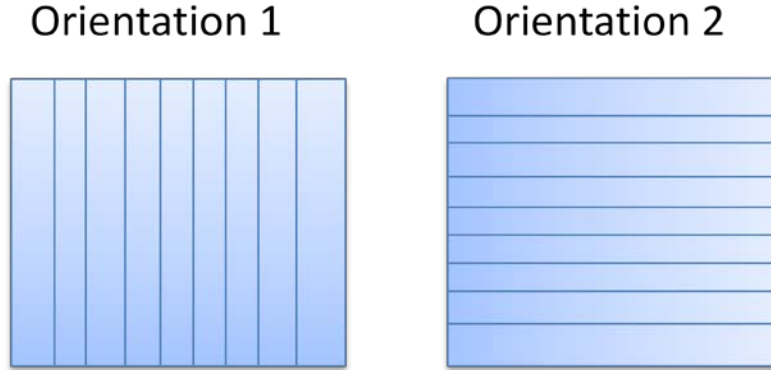


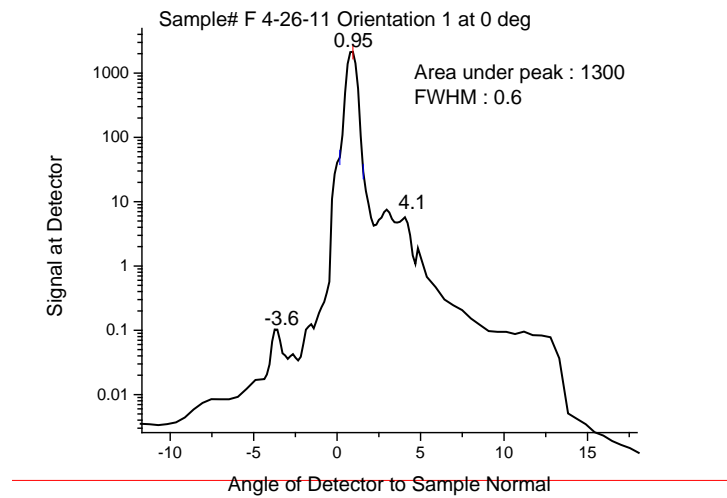
**Figure 40: OPGaAs domain orientations used in CASI measurements for each sample. The laser source was kept normally incident for both orientations.**

The data produced by the CASI is not in a standard coordinate system as the  $0^\circ$  reflection point is at the specular reflection. The reason for this is evident when one considers the system was primarily designed for analyzing surface quality by taking very fine angular resolution data of the specular reflection. The CASI analysis software plots this data in log-log form, meshing positive and negative angles near a “zero” point, so that the specular piece appears very wide and the quality of the surface can be assessed very quickly without additional analysis. To convert the CASI data into standard coordinates, the rotation angle is added to the CASI angle, producing  $\theta_r$  measured from normal. Due to the transmissive measurements, the resulting data is of the form  $(\theta_r, \text{BTDF})$  [42]. Depending on the spacing (grating period) of the material, diffraction orders may appear on the plot as well. Because the grating period for OPGaAs structures ( $110 \mu\text{m}$ ) are comparable to the wavelength ( $8.15 \mu\text{m}$ ), these diffraction patterns will be seen for the first few orders.

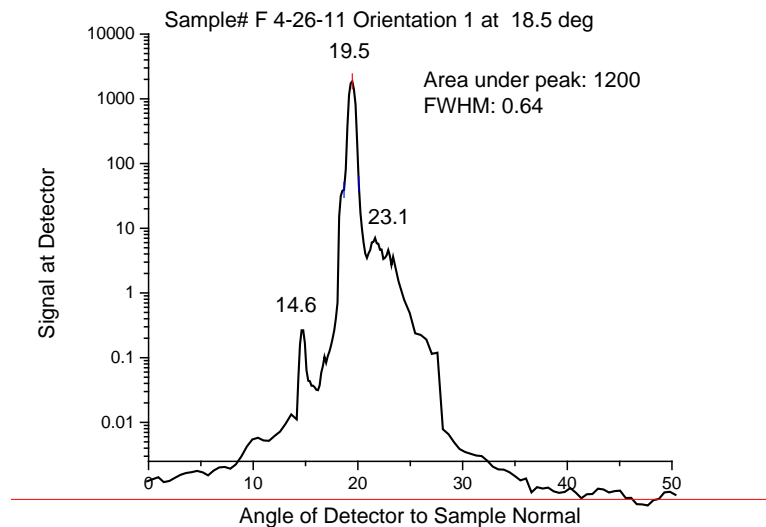
Figures 47 thru 50 display the scattering measurement of sample F 4-26-11 for both orientations, with the incident light normal to the sample surface and Figures 51 thru

58 show the same for sample F 5-11-11. Interestingly, while the former shows no diffraction patterns, the latter has some diffraction patterns evident for both orientations. Both samples were patterned and it was expected before the experiment that these patterns could act as a diffraction grating and give rise to a diffraction pattern at the detector. But these patterns were missing for the first sample (resulting in lower diffraction loss, a desired feature). This could be because the first sample was not doped with excess Si while the second sample was. This addition could have induced a change in the index of refraction across the sample, especially between the patterned and unpatterned material. This change can cause the incident light to diffract from the sample and create the patterns noticed for sample F 5-11-11. This analysis emphasizes the minimization of impurities in the sample to reduce resulting diffraction loss.

Figures 41 and 42 display the CASI measurement collected with an angle of incidence,  $\theta_i = 0^\circ, 18.5^\circ$  respectively, to the sample's (# F 4-26-11) surface. No meaningful diffraction patterns were detected. Also note the Y-axis is a logarithmic scale and any features other than the peak near the incident angle would be hard to distinguish on a regular scale.

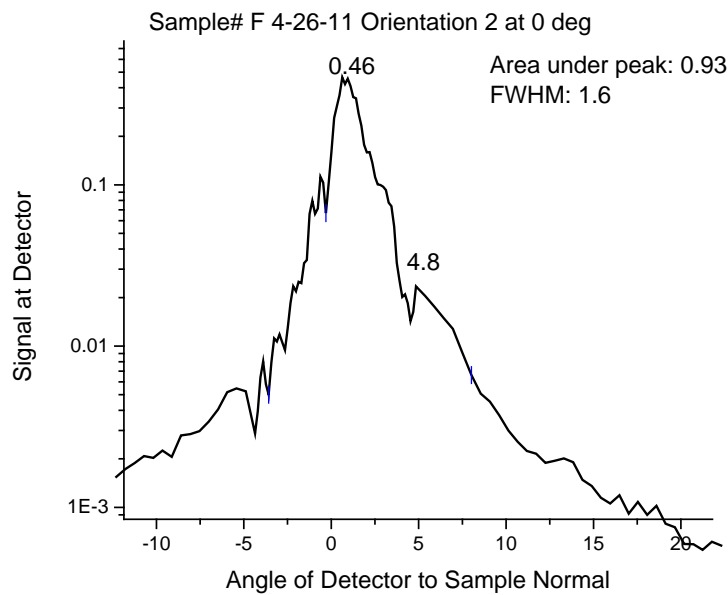


**Figure 41:** CASI measurement collected with an angle of incidence,  $\theta_i = 0^\circ$ , to the sample's (# F 4-26-11) surface normal. No meaningful diffraction patterns were detected. Note the Y-axis is a logarithmic scale and any features other than the peak at  $0.95^\circ$  would be hard to distinguish on a regular scale.

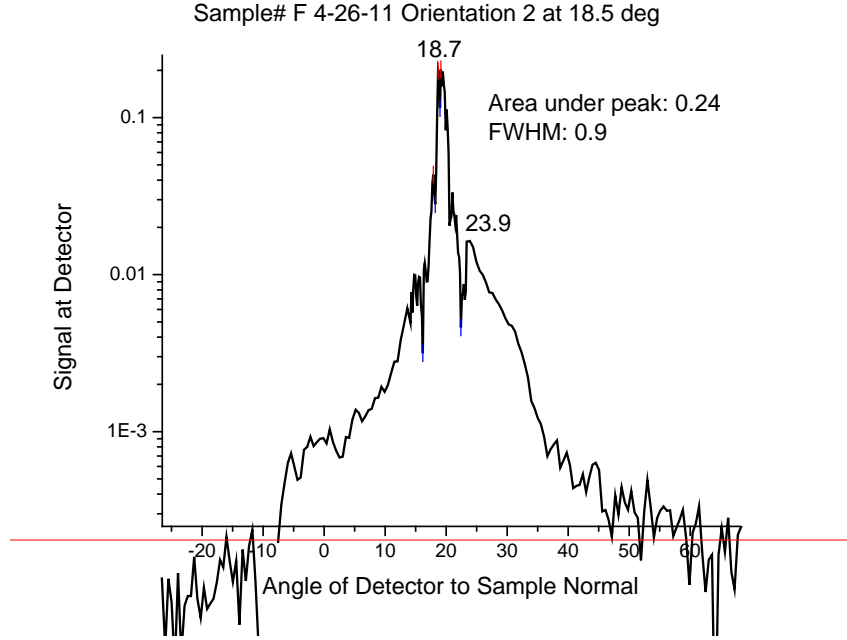


**Figure 42:** CASI measurement collected with an angle of incidence,  $\theta_i = 18.5^\circ$ , to the sample's (# F 4-26-11) surface normal. No meaningful diffraction patterns were detected. Note the Y-axis is a logarithmic scale and any features other than the peak at  $19.5^\circ$  would be hard to distinguish on a regular scale.

Figures 43 and 44 display the CASI measurement collected for a different sample orientation than before. As explained in Figure 46, the sample was turned by  $90^\circ$ . Data was gathered again for incident angles,  $\theta_i = 0^\circ$  and  $18.5^\circ$ . No meaningful diffraction patterns were detected. Also note the Y-axis is a logarithmic scale and any features other than the peak near the incident angle would be hard to distinguish on a regular scale.



**Figure 43:** CASI measurement collected with an angle of incidence,  $\theta_i = 0^\circ$ , to the sample's (# F 4-26-11) surface normal. No meaningful diffraction patterns were detected for this orientation either. Note the Y-axis is a logarithmic scale and any features other than the peak at  $0.46^\circ$  would be hard to distinguish on a regular scale.



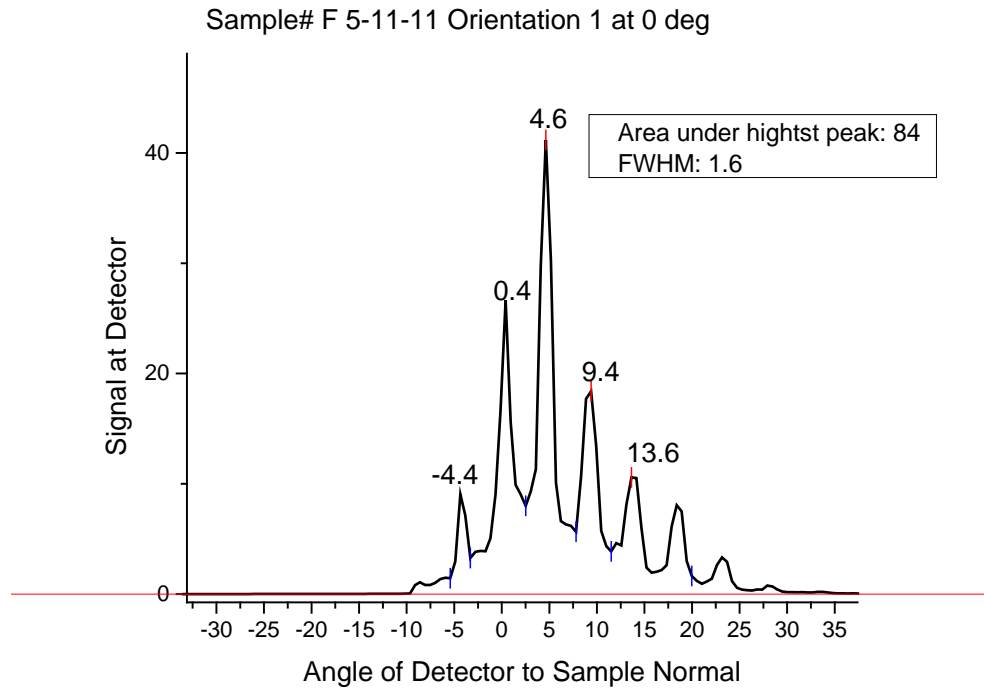
**Figure 44: CASI measurement collected with an angle of incidence,  $\theta_i = 18.5^\circ$ , to the sample's (# F 4-26-11) surface normal. No meaningful diffraction patterns were detected for this orientation either. Note the Y-axis is a logarithmic scale and any features other than the peak at  $18.7^\circ$  would be hard to distinguish on a regular scale.**

Figure 45 shows the CASI measurement for the second sample (F 5-11-11) at  $\theta_i = 0^\circ$ . The zero-order (specular) peak is seen at  $\theta_r = 0^\circ$ , along with five positive and one negative diffraction orders. The diffraction angles in Figure. 45 can be predicted using the Diffraction Grating equation as explained in Chapter II. Assuming the distance between the slits or the domains,  $d$ , to be  $100 \mu\text{m}$  apart, the angles are

$$n\lambda = d(\sin \theta_r - \sin \theta_i), \text{ For } \theta_i = 0,$$

$$\theta = \sin^{-1}\left(\frac{n\lambda}{d}\right) = -4.6^\circ, 0^\circ, 4.6^\circ, 9.4^\circ, 14.2^\circ, \text{etc.}$$





**Figure 45:** CASI measurement collected with an angle of incidence,  $\theta_i = 0^\circ$ , to the sample's (# F 5-11-11) surface normal. Note linear scale in Y-axis. Diffraction patterns are visible for the first few orders near the incident angle. The diffraction angles complement the theoretical values:

$$\text{For } \theta_i = 0, \theta_r = \sin^{-1}\left(\frac{n\lambda}{d}\right) = -4.6^\circ, 0^\circ, 4.6^\circ, 9.4^\circ, 14.2^\circ, \text{etc.}$$

Figure 46 shows the CASI measurement for the second sample (F 5-11-11) at  $\theta_i = 18.5^\circ$ . Diffraction patterns are visible for the first few orders near the incident angle.

The diffraction angles complement the theoretical values:

$$\text{For } \theta_i = 18.5, \theta_r = \sin^{-1}\left(\frac{n\lambda + d \sin \theta_i}{d}\right) = 13.6^\circ, 18.5^\circ, 23.5^\circ, 28.7^\circ, 34.2^\circ, \text{etc.}$$

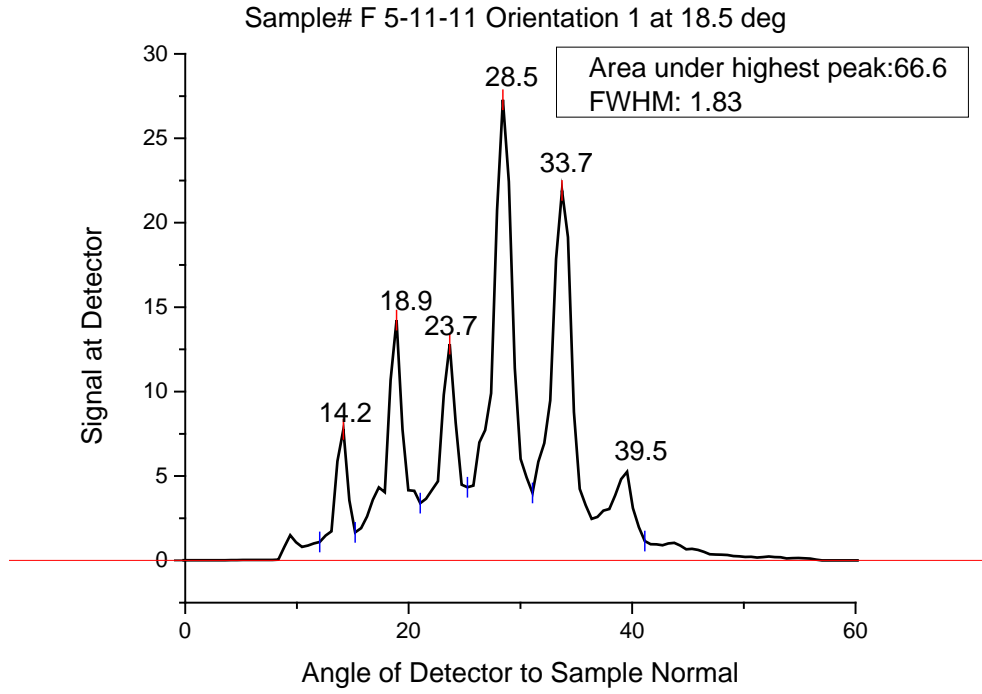


**Figure 46:** CASI measurement collected with an angle of incidence,  $\theta_i = 18.5^\circ$ , to the sample's (# F 5-11-11) surface normal. Note linear scale in Y-axis. Diffraction patterns are visible for the first few orders near the incident angle. The diffraction angles complement the theoretical values:

$$\text{For } \theta_i = 18.5, \theta_r = \sin^{-1} \left( \frac{n\lambda + d \sin \theta_i}{d} \right) = 13.6^\circ, 18.5^\circ, 23.5^\circ, 28.7^\circ, 34.2^\circ, \text{etc.}$$

Figure 47 shows the CASI measurement for the second sample (F 5-11-11) at  $\theta_i = 37^\circ$ . Diffraction patterns are visible for the first few orders near the incident angle.

The diffraction angles complement the theoretical values:

$$\text{For } \theta_i = 37, \theta_r = \sin^{-1} \left( \frac{n\lambda + d \sin \theta_i}{d} \right) = 26.0^\circ, 31.3^\circ, 37^\circ, 43.1^\circ, 49.9^\circ, 57.8^\circ, \dots$$

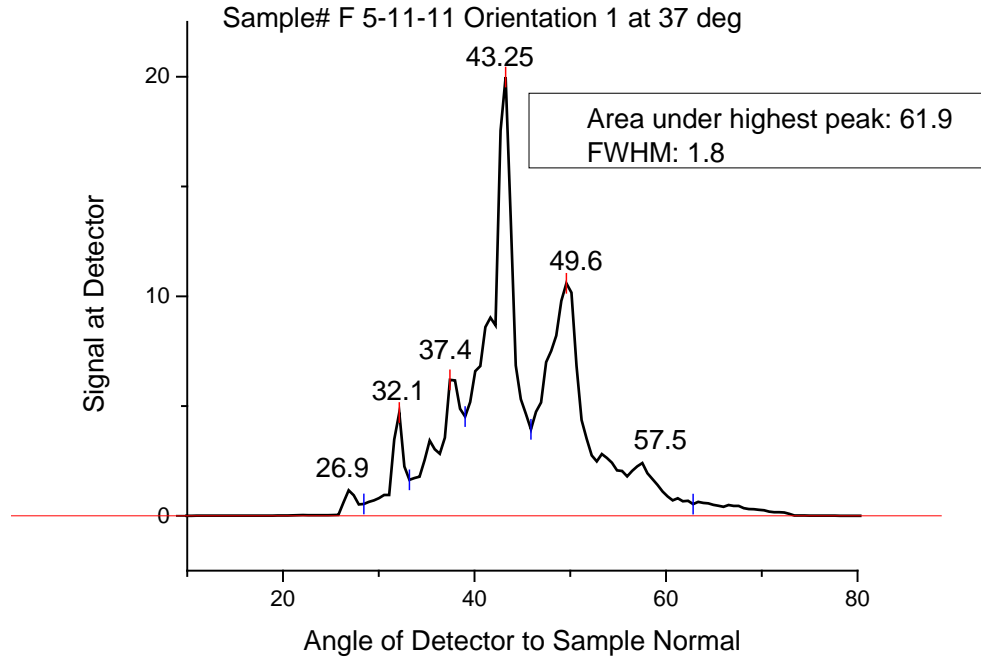


**Figure 47:** CASI measurement collected with an angle of incidence,  $\theta_i = 37^\circ$ , to the sample's (# F 5-11-11) surface normal. Note linear scale in Y-axis. Diffraction patterns are visible for the first few orders near the incident angle. The diffraction angles complement the theoretical values:

$$\text{For } \theta_i = 37, \theta_r = \sin^{-1}\left(\frac{n\lambda + d \sin \theta_i}{d}\right) = 26.0^\circ, 31.3^\circ, 37^\circ, 43.1^\circ, 49.9^\circ, 57.8^\circ, \dots$$

Figure 48 shows the CASI measurement for the second sample (F 5-11-11) at  $\theta_i = 55.5^\circ$ . Diffraction patterns are visible for the first few orders near the incident angle.

The diffraction angles complement the theoretical values:

$$\text{For } \theta_i = 55.5, \theta_r = \sin^{-1}\left(\frac{n\lambda + d \sin \theta_i}{d}\right) = 48.0^\circ, 55.5^\circ, 64.9^\circ, 80.8^\circ, \dots$$

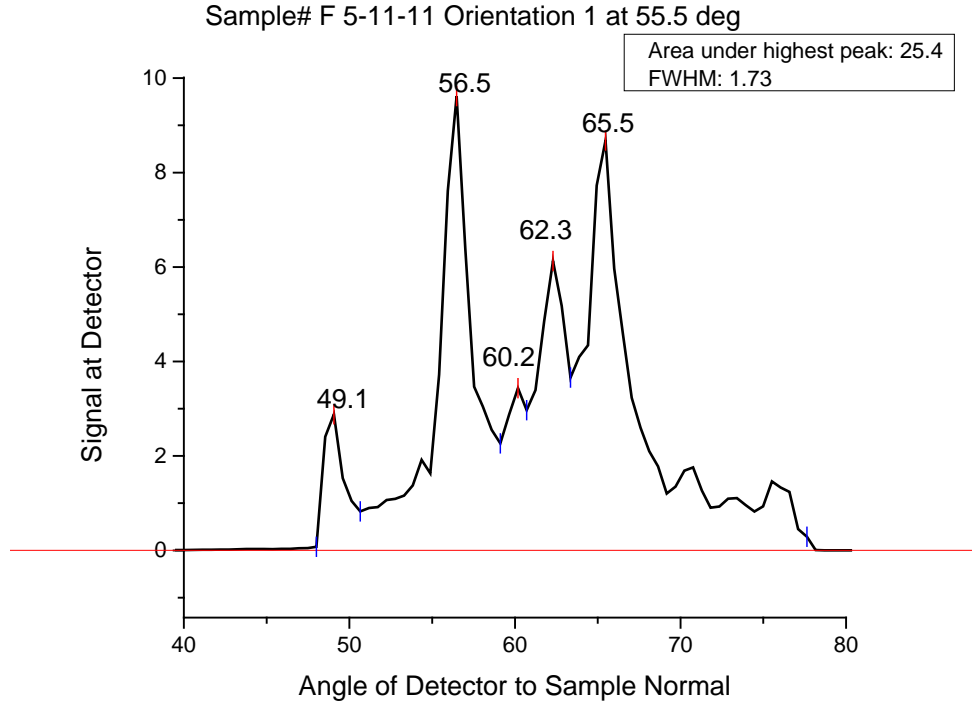


**Figure 48:** CASI measurement collected with an angle of incidence,  $\theta_i = 55.5^\circ$ , to the sample's (# F 5-11-11) surface normal. Note linear scale in Y-axis. Diffraction patterns are visible for the first few orders near the incident angle. The diffraction angles complement the theoretical values:

$$\text{For } \theta_i = 55.5, \theta_r = \sin^{-1} \left( \frac{n\lambda + d \sin \theta_i}{d} \right) = 48.0^\circ, 55.5^\circ, 64.9^\circ, 80.8^\circ, \dots$$

Figures 49 thru 52 shows the CASI measurement for the second sample (F 5-11-11) with the second orientation at  $\theta_i = 0^\circ, 18.5^\circ, 37^\circ$  and  $55.5^\circ$  respectively. Multiple diffraction patterns disappear, as now the diffraction peaks were formed perpendicular to the lab floor and the detector was only able to detect one of the peaks as it went around the arc.

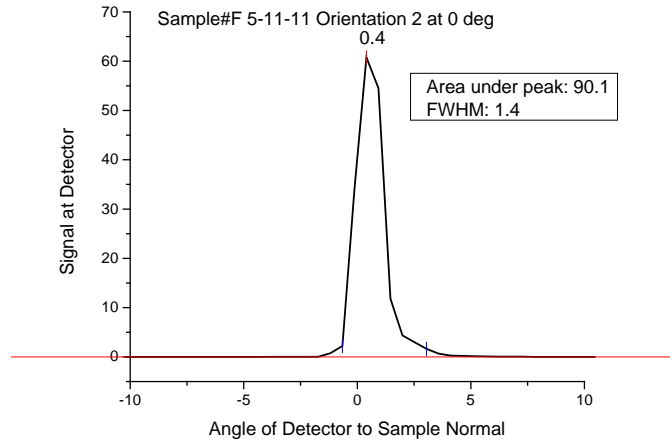


**Figure 49:** CASI measurement collected with an angle of incidence,  $\theta_i = 0^\circ$ , to the sample's (# F 5-11-11) surface normal. Diffraction patterns disappear as the sample is rotated  $90^\circ$ . A possible reason could be that the diffraction peaks were formed perpendicular to the lab floor and the detector was only able to detect one of the peaks as it went around the arc.

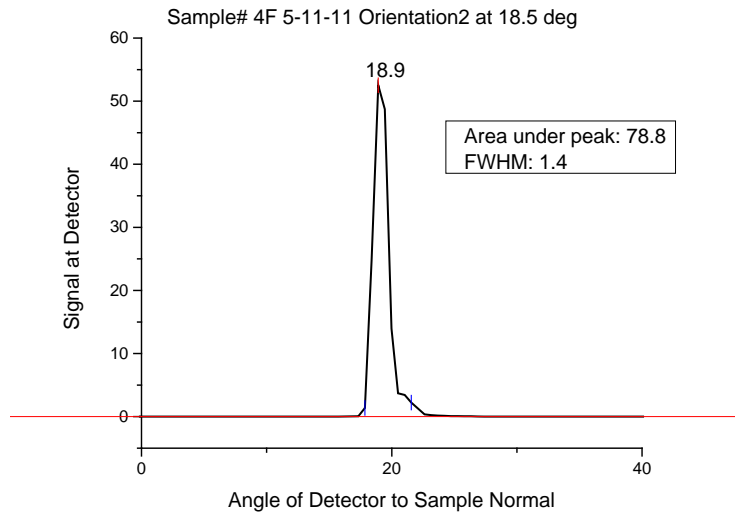


**Figure 50:** CASI measurement collected with an angle of incidence,  $\theta_i = 18.5^\circ$ , to the sample's (# F 5-11-11) surface normal. Diffraction patterns disappear as the sample is rotated  $90^\circ$ . A possible reason could be that the diffraction peaks were formed perpendicular to the lab floor and the detector was only able to detect one of the peaks as it went around the arc.

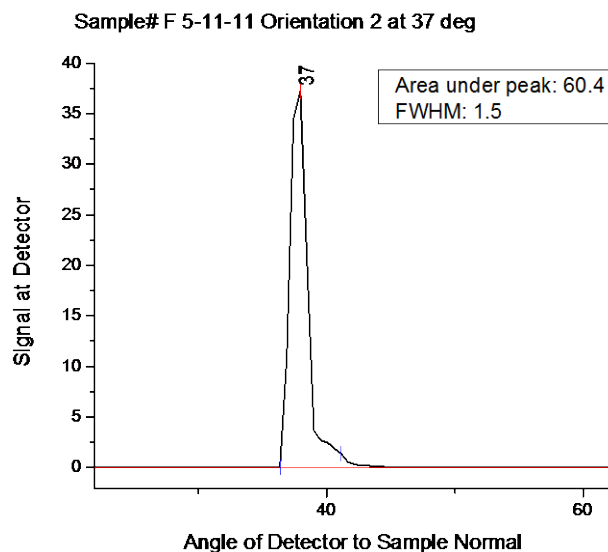


**Figure 51:** CASI measurement collected with an angle of incidence,  $\theta_i = 37^\circ$ , to the sample's (# F 5-11-11) surface normal.. Diffraction patterns disappear as the sample is rotated  $90^\circ$ . A possible reason could be that the diffraction peaks were formed perpendicular to the lab floor and the detector was only able to detect one of the peaks as it went around the arc.

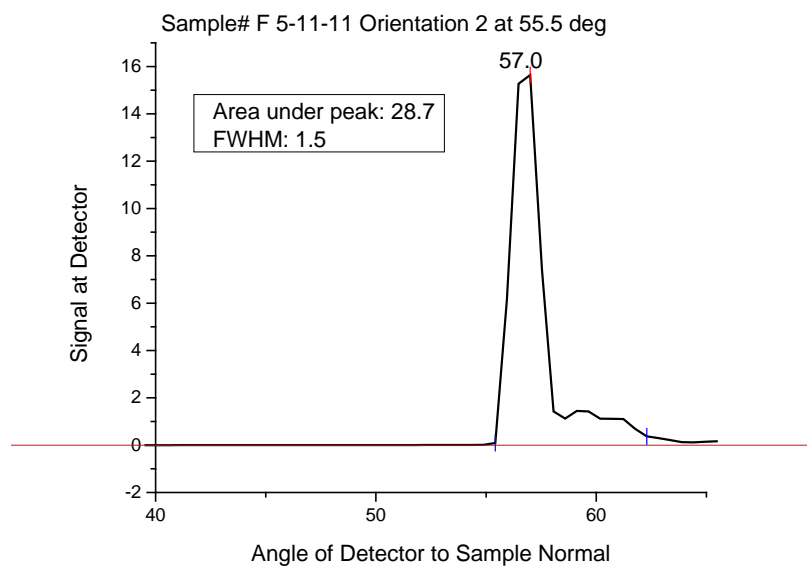
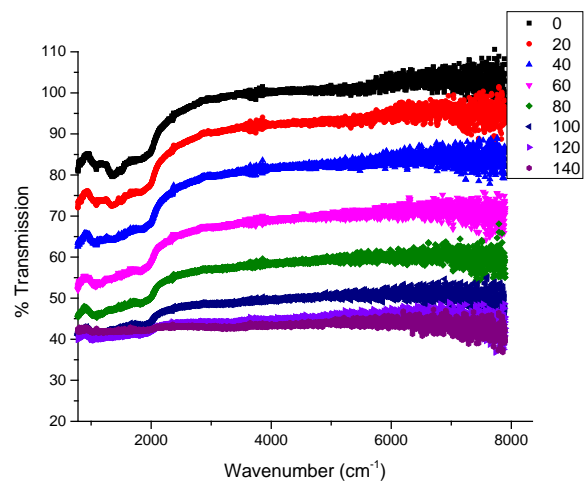


**Figure 52:** CASI measurement collected with an angle of incidence,  $\theta_i = 55.5^\circ$ , to the sample's (# F 5-11-11) surface normal. Diffraction patterns disappear as the sample is rotated  $90^\circ$ . A possible reason could be that the diffraction peaks were formed perpendicular to the lab floor and the detector was only able to detect one of the peaks as it went around the arc.

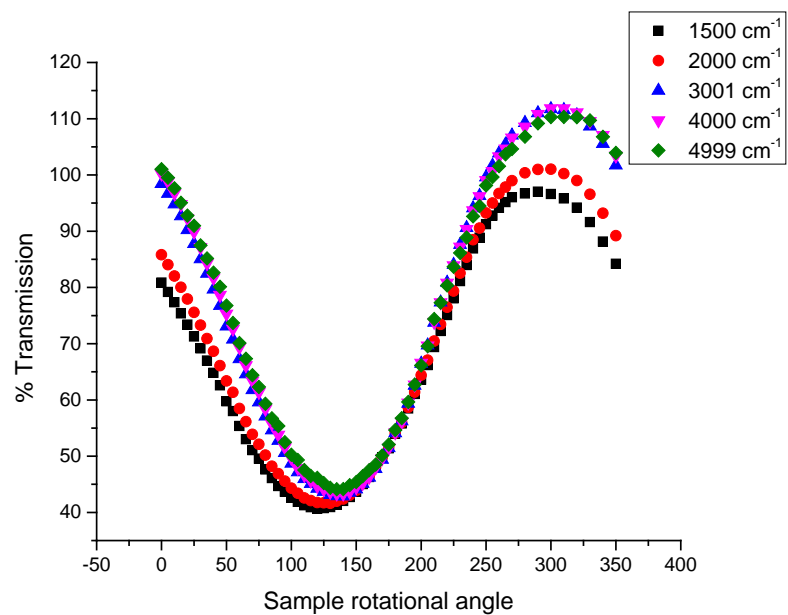
Although the CASI incident laser beam was focused at the detector and not at the sample for all measurements, it has already been verified that there is close agreement between both CASI laser conditions [43]. Small differences in intensity between the orientations may be due to slight differences in laser alignment introduced when the sample was rotated.

## **FTIR**

Samples used in CASI were both OPGaAs with different doping characteristics and hence displayed different absorption profiles as seen before. Both the patterned samples also exhibited some orientation dependence on transmission signal collected by the CASI detector. Thus, to better understand this polarization effect from the grated material, the same two samples were also used in the FTIR measurements. Figure 53 shows the transmission data collected for sample F 4-26-11 from  $0^\circ$  to  $140^\circ$  in  $20^\circ$  increments. Figure 54 is a plot of change in transmission for certain wavenumbers picked from the low noise area of Figure 53.



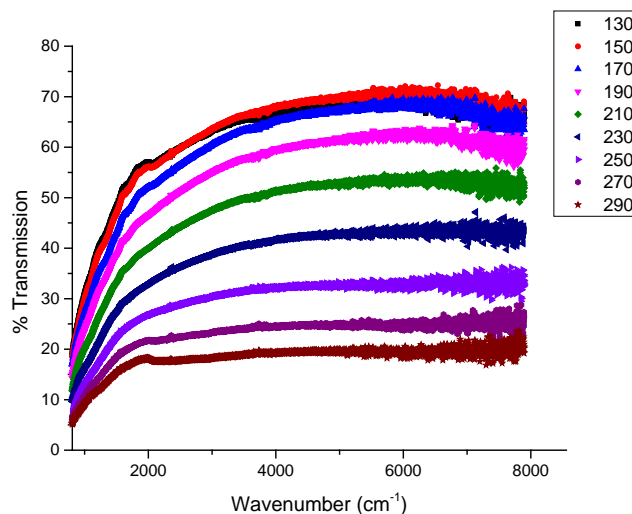
**Figure 53: FTIR transmission measurements for sample F 4-26-11 as the sample is rotated from 0° to 140° under a constant polarization incident light.**



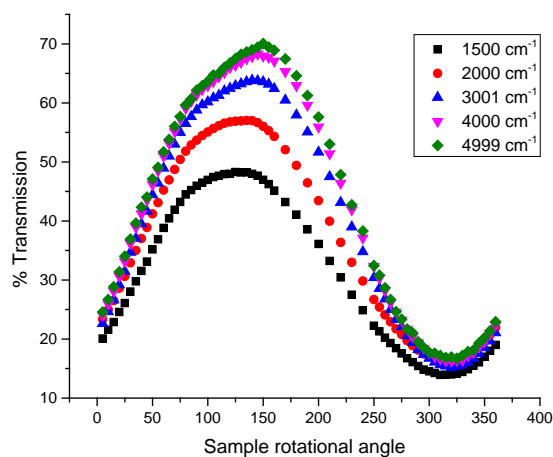
**Figure 54: Change in transmission through the sample F 4-26-11 as it is rotated from 0 to 360 degrees.**



Figure 55 shows the transmission data collected for sample F 5-11-11 from 130° to 290° in 20° increments. Figure 56 is a plot of change in transmission for certain wavenumbers picked from the low noise area of Figure 55.



**Figure 55: FTIR transmission measurements for sample F 5-11-11 as the sample is rotated from 0° to 140° under a constant polarization incident light. Note the lower transmission at lower wavenumbers due to IR absorption of free carriers.**



**Figure 56: Change in transmission through the sample F 5-11-11 as it is rotated from 0 to 360 degrees.**

Note these measurements were repeated and examined closely as very large transmission changes were recorded in both samples. Troubleshooting was conducted as these results were believed to be a product of an experimental artifact since, in Figures 53 and 55, the sample had vastly varying detector signals at 180° apart. While the beam location on the sample is assumed fixed, it is possible that while rotating the sample, the incident beam might be getting clipped by the sample holder. So FTIR transmission measurements were again taken with the same setup as before, but this time without the sample in the sample holder to look for any possible clipping of the incident beam.

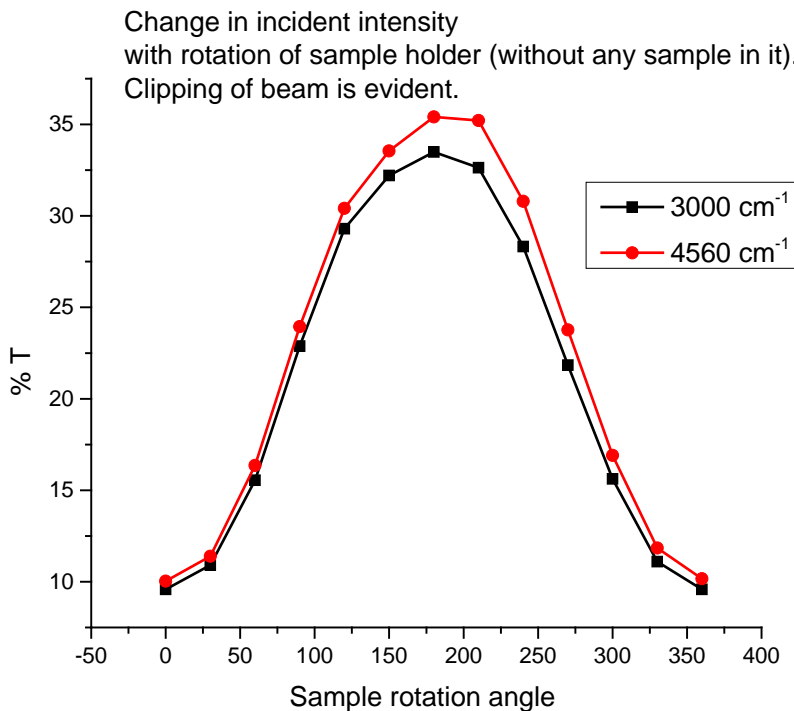


**Figure 57: Change in incident intensity due to clipping of the beam by the sample holder. Misaligned sample holder in the experiment created majority of the transmission changes in Figures 53 thru 56.**



**Figure 58:** The sample holder hole was misaligned with the center of the FTIR beam. This caused clipping of the incident beam and non-uniform transmission through the sample holder to the detector.

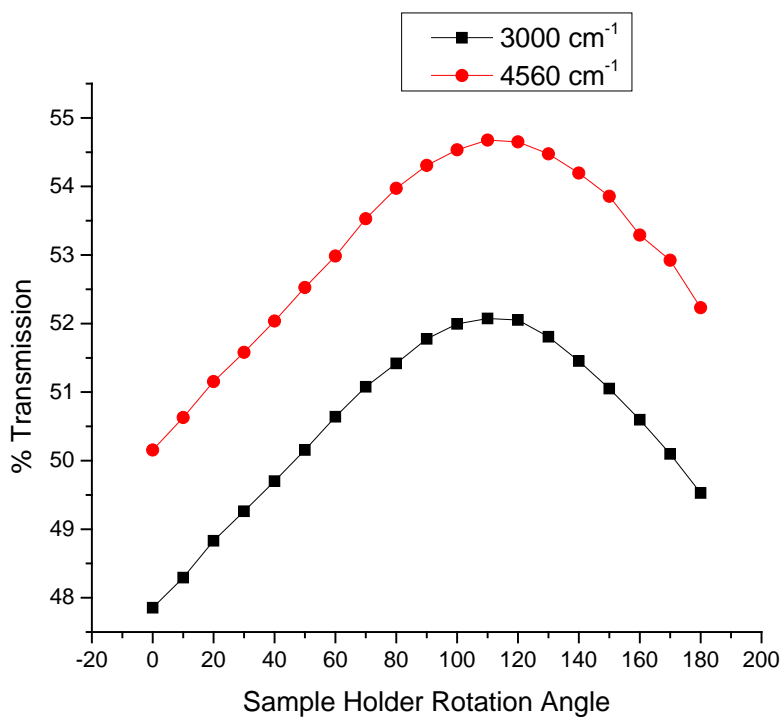


**Figure 59:** New sample holder tested without the sample in it for any incident beam clipping. Some clipping is present (although far less than the previous sample holder as shown in Figure 61) as the detected intensity is not uniform as the sample is rotated.

Figure 57 shows the change in incident intensity due to clipping of the beam by the sample holder. Thus it is evident that a misaligned sample holder in the experiment created majority of the transmission changes in Figures 53 thru 56. The sample holder hole was misaligned with the center of the FTIR beam as shown in Figure 58. This caused clipping of the incident beam and non-uniform transmission through the sample holder to the detector. So the sample holder was replaced with another, possessing a symmetrical outer circle and a machined inner circle. This new sample holder was also tested without the sample in it for any incident beam clipping. Figure 59 demonstrates the change in intensity at the detector as the sample holder is rotated. Unfortunately, even after many attempts of aligning the sample holder to the center of the FTIR beam (having a beam width larger than the inner circle of the sample holder) the clipping was not completely eliminated, although the degree of clipping was minimized drastically.

In order to circumvent this issue of varying incident intensity falling on the detector, the transmission measurements for both the samples was measured from  $0^\circ$  to  $180^\circ$  in  $10^\circ$  increments. Then these transmitted numbers for the two arbitrarily picked wavelengths ( $3000$  and  $4560\text{ cm}^{-1}$ ) were divided by the corresponding numbers obtained for just the holder in Figure 59. The results (converted to percentages) of this calculation are plotted in Figure 60. While the results are still not in harmony when  $180^\circ$  apart, the gross amplification due to the misaligned sample holder is gone. Also, the absolute effect of polarization from the grated material although present, is greatly minimized.

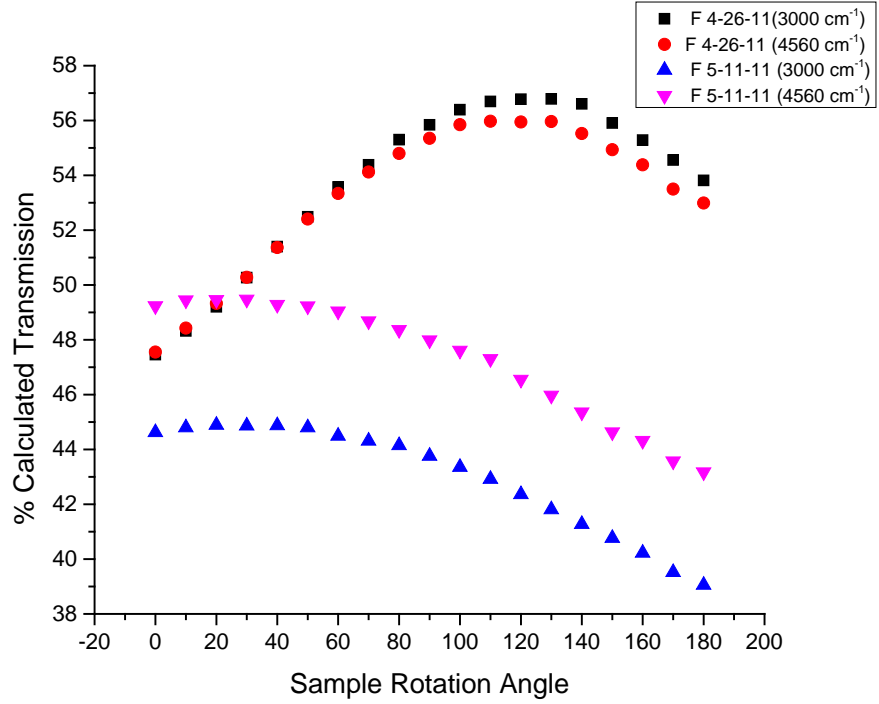


**Figure 60:** The transmitted numbers of the two samples, found using the new sample holder for the two arbitrarily picked wavelength (3000 and 4560  $\text{cm}^{-1}$ ) was divided by the corresponding numbers obtained for just the holder in Figure 65. The result is converted to percentage and plotted. Some polarization effect from the grated material exists for both the samples.

## Summary

This chapter presented the data collected in all three experiments performed in this thesis. Absorption coefficient measurements were measured for GaAs, GaP and  $\text{Fe}^{2+}\text{ZnSe}$  samples using laser calorimetry. CASI measurements were conducted and diffraction patterns as predicted were detected only for the sample with excessive doping of Si. FTIR measurements for both patterned GaAs samples exhibited some polarization effect from the grated material.

## **V. Conclusions and Recommendations**

### **Chapter Overview**

This chapter summarizes the findings of this research and comments on their significance. Also covered are more short-term immediate actions to be taken and longer term recommendations for future work.

### **Conclusions of Research**

A technique to measure absorption loss in AFRL grown materials was built, successfully demonstrated and validated on multiple samples. The laser calorimeter can be used by AFRL on materials grown domestically to characterize and determine the loss mechanisms. This can help achieve optimum HVPE growth configuration (or recipe) for maximizing device efficiency. It can also be used as a tool to compare multiple unpolished samples post-growth to help decide which sample has a lower absorption loss and is worth spending the extra money to have polishing and AR coating done.

CASI measurements conducted on two patterned GaAs samples provided some interesting results. It was expected before the experiment that these patterns would act as a diffraction grating and give rise to a diffraction pattern at the detector. But these patterns were only detected for the sample with excessive doping of Si. This addition could have induced a change in the index of refraction across the sample, especially between the patterned and unpatterned material, a possible source of the diffraction pattern. This analysis emphasizes the minimization of impurities within the sample to reduce resulting diffraction loss

Incident polarization dependence on patterned samples was investigated using an FTIR and a wire grid polarizer. Initial FTIR measurements were marred by a misaligned sample holder resulting in clipping of the incident beam. The sample holder was replaced by one with better symmetrical circles and the alignment issues were minimized. Both patterned GaAs samples exhibited some polarization effect from the grating material. The amount of transmission detected changed by as much as 20% for both samples as they were rotated to change incident polarization.

## **Recommendations for Action and Future Research**

### ***Accounting for Surface Absorption:***

Since laser calorimetry does not differentiate between bulk and surface absorption, the surface absorption,  $a_{surface}$ , was neglected for all the samples (since they were polished) in this thesis. Bulk absorption coefficient measured in this thesis was higher than the published values and the total absorptance,  $a$ , goes as,  $a \approx \alpha l + a_{surface}$ , where  $\alpha$  is the absorption coefficient and  $l$  is the sample thickness. This relationship can help explain the higher than usual numbers measured. In order to account for surface absorption and ensure that it is small enough to be neglected, we can take a set of similar samples with varying thickness and calculate their absorptance using laser calorimetry. Then the y-intercept of absorptance versus sample thickness gives us surface absorption.

### ***Adopting a Different Wavelength***

Using a 2  $\mu\text{m}$  laser should make this experiment more appealing for GaAs due to related real world applications. An OPO pump laser can be used possibly to get useful results that can help possibly with enhancing device efficiency.

### ***Diffraction from Sample Edge***

For CASI and FTIR, it would be of more practical use if both these experiments were repeated with the incident light focused on the polished edge of the sample to resemble the actual real-estate as used in an OPO. Also, a better sample holder with perfect alignment is needed for the CASI setup to ensure beam clipping is further minimized.

### ***Photothermal Deflection Technique***

Photothermal Deflection Spectroscopy (PDS) can be used as an alternate method to measure absorption coefficient and also to verify laser calorimetry results. The advantage of this technique is that it measures only the true bulk absorption of the sample. The setup is shown in Figure 61, it explains how PDS measures the heating of the environment which occurs when a sample absorbs light from an incident pump laser [44]. The sample then transfers some of the heat to the surrounding medium which produces a change in index of the medium. Thus, when a probe laser beam around the sample produces a deflection in the probe laser beam passes through the liquid medium, it gets slightly deflected and this measured deflection is proportional to the absorption of the original material.



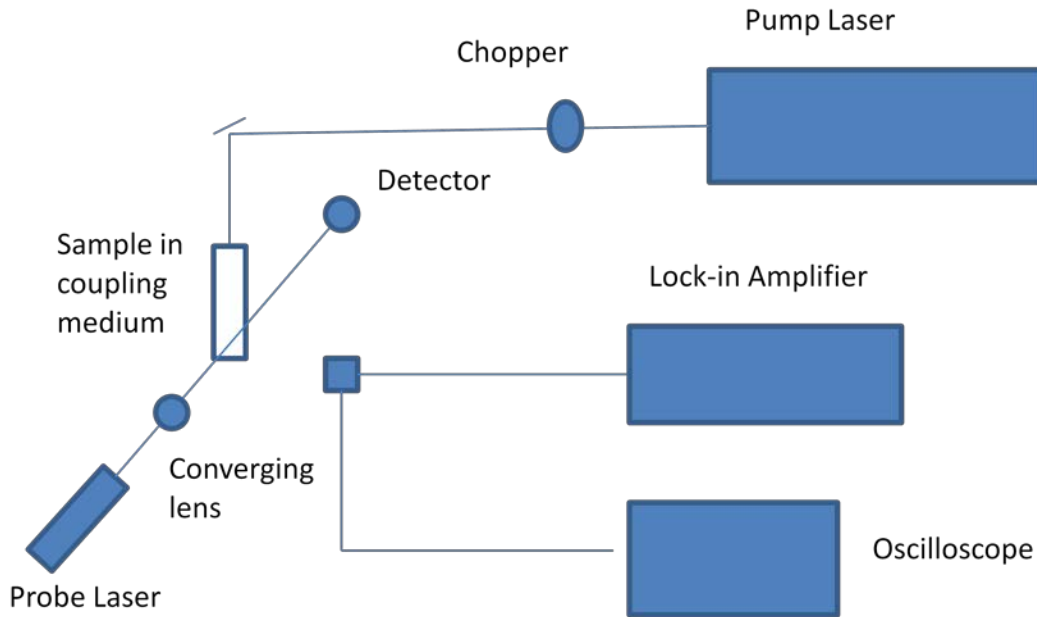


**Figure 61: Photothermal deflection setup as a future recommendation to measure the absorption coefficient of various samples. Figure was self-drawn and adapted from [44].**

## Summary

An absorption loss characterization tool was added to the AFRL inventory. Absorption coefficient of various samples can now be reliably measured and results can help achieve optimum HVPE growth configuration for maximizing device efficiency. Rapid post growth loss analysis can also help decide which samples are promising enough for further processing (polishing, AR coating, etc.). Careful management of any additionally added dopants (like Si impurities) was advised as this can lead to diffraction losses in the sample, as shown by the CASI experiment. The FTIR experiment detected a subtle relationship between the incident polarization of light and the associated transmission signal from the OPGaAs samples.

## Appendix A

Following figures show the fitting performed by 'OriginPro 9' to the cooling curves of the calorimetry measurements.

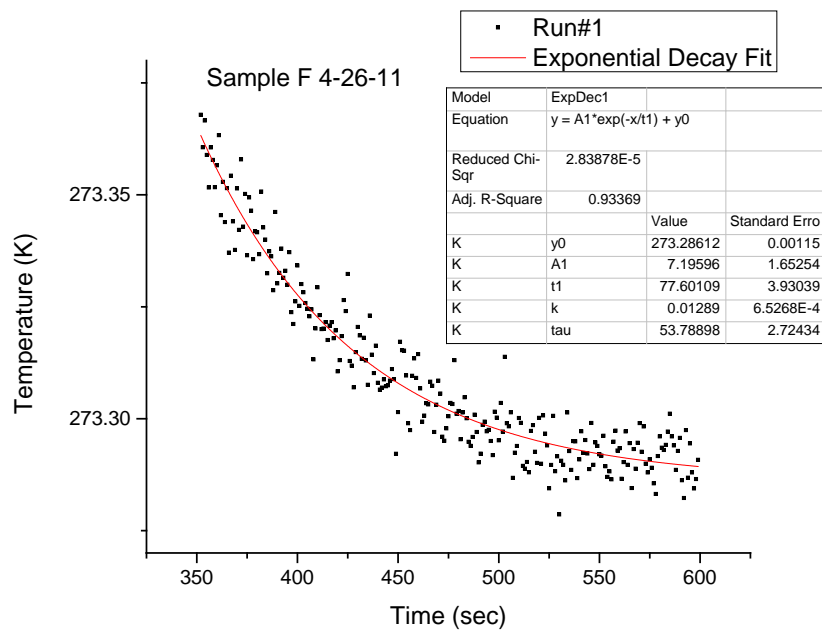


**Figure 62: Sample# F 4-26-11 Run#1 cooling curve is fitted to an exponential decay function.**

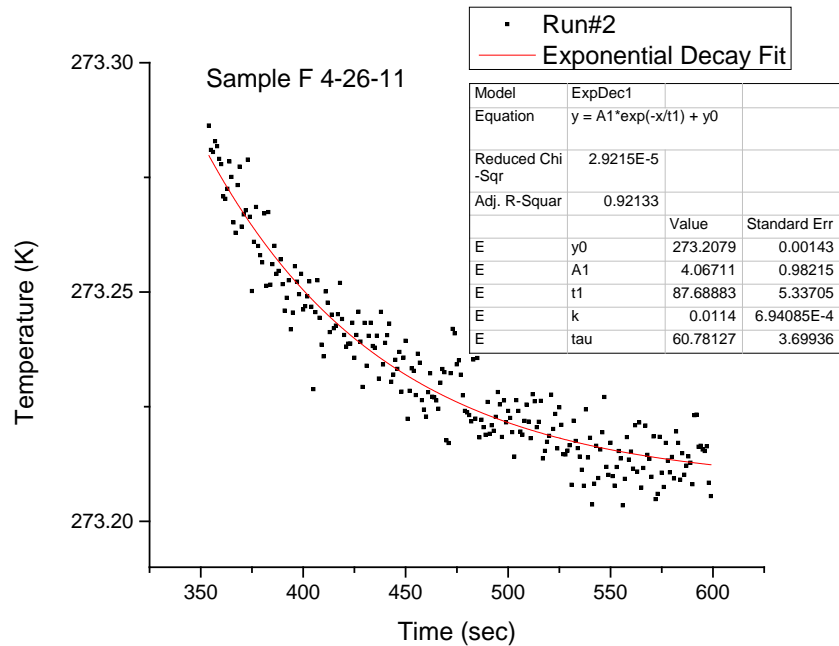


Figure 63: Sample F 4-26-11 Run#2 cooling curve is fitted to an exponential decay function.

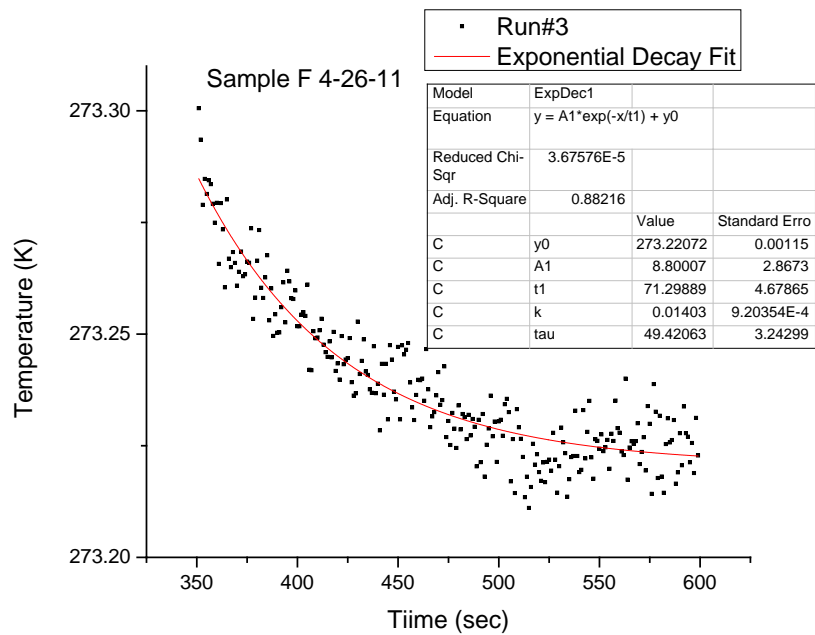


Figure 64: Sample F 4-26-11 Run#3 cooling curve is fitted to an exponential decay function.

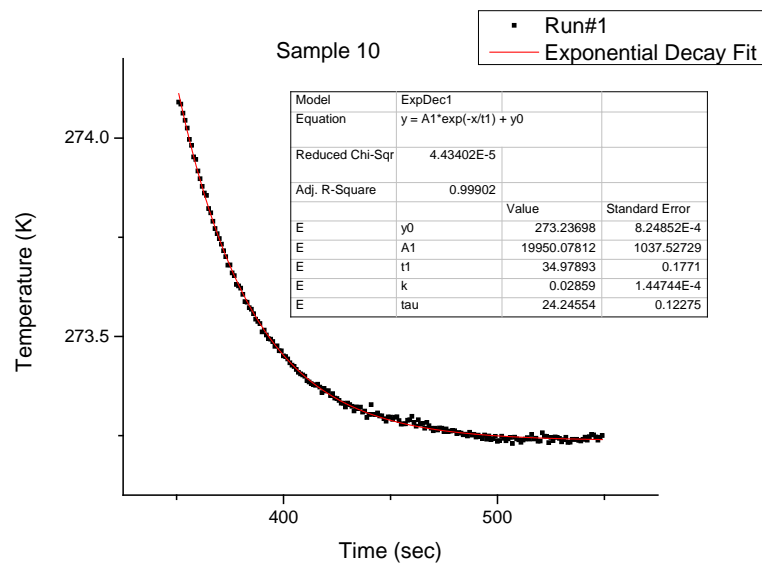


Figure 65: Sample F 5-11-11 Run#1 cooling curve is fitted to an exponential decay function.

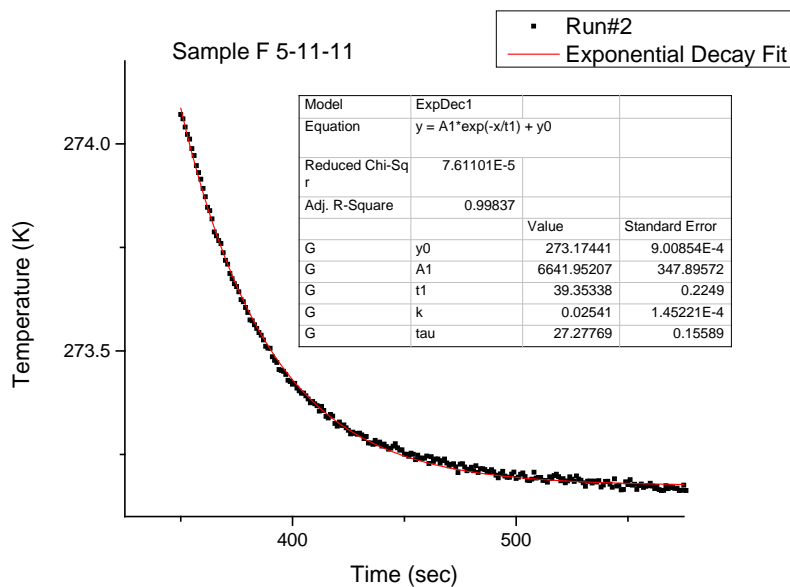


Figure 66: Sample F 5-11-11 Run#2 cooling curve is fitted to an exponential decay function.

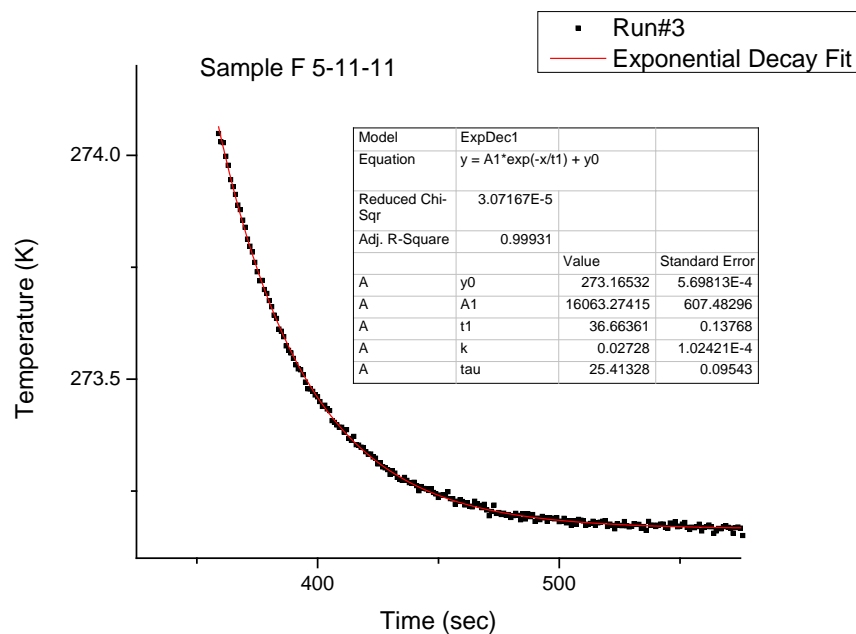


Figure 67: Sample F 5-11-11 Run#3 cooling curve is fitted to an exponential decay function.

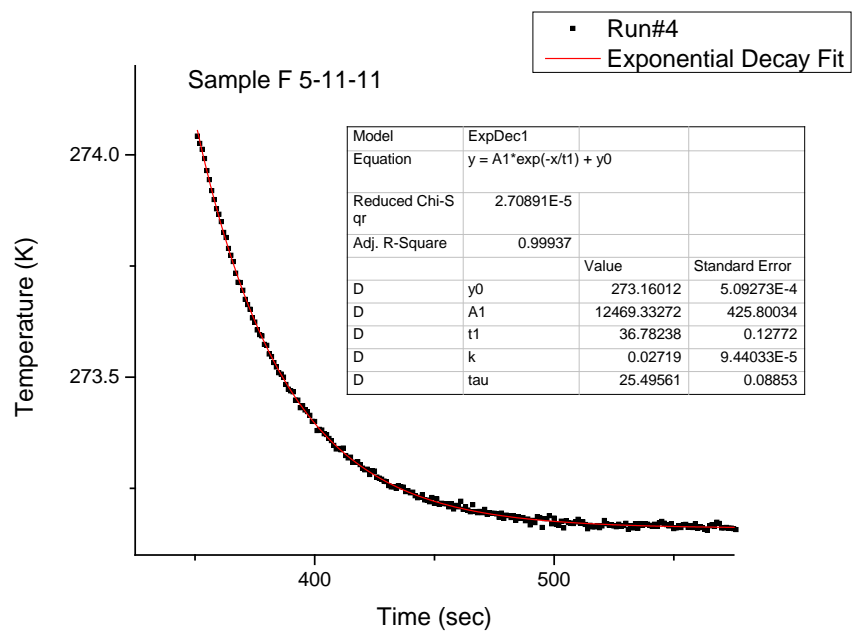


Figure 68: Sample F 5-11-11 Run#4 cooling curve is fitted to an exponential decay function.

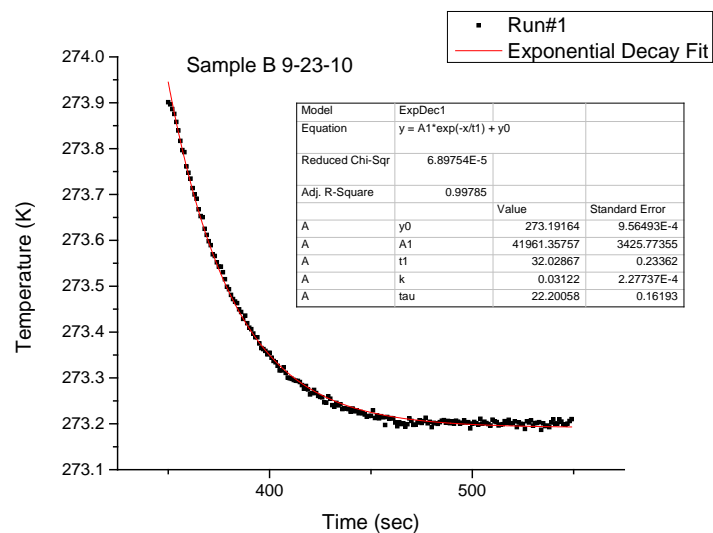


Figure 69: Sample B 9-23-10 Run#1 cooling curve is fitted to an exponential decay function.

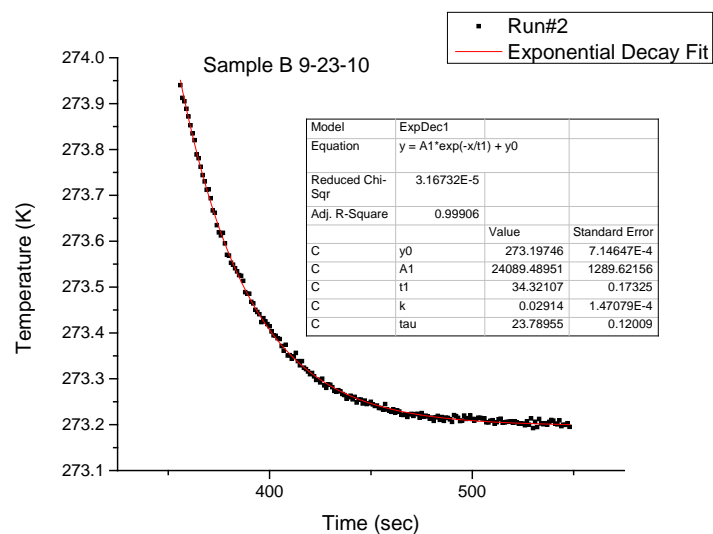


Figure 70: Sample B 9-23-10 Run#2 cooling curve is fitted to an exponential decay function.

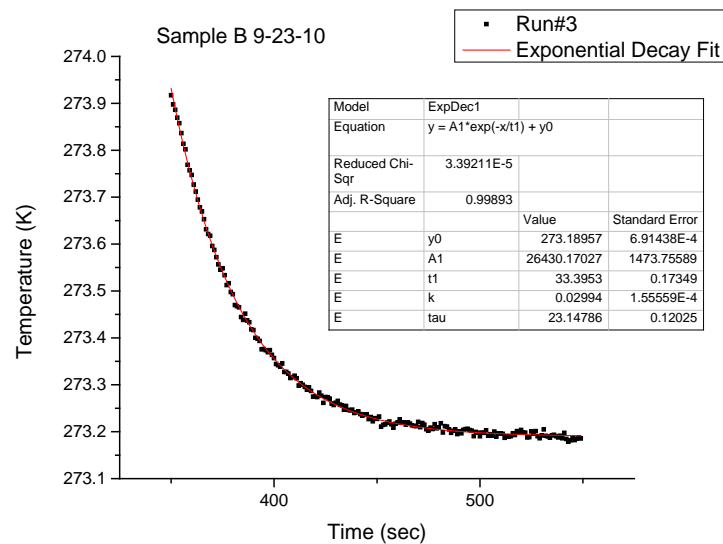


Figure 71: Sample B 9-23-10 Run#3 cooling curve is fitted to an exponential decay function.

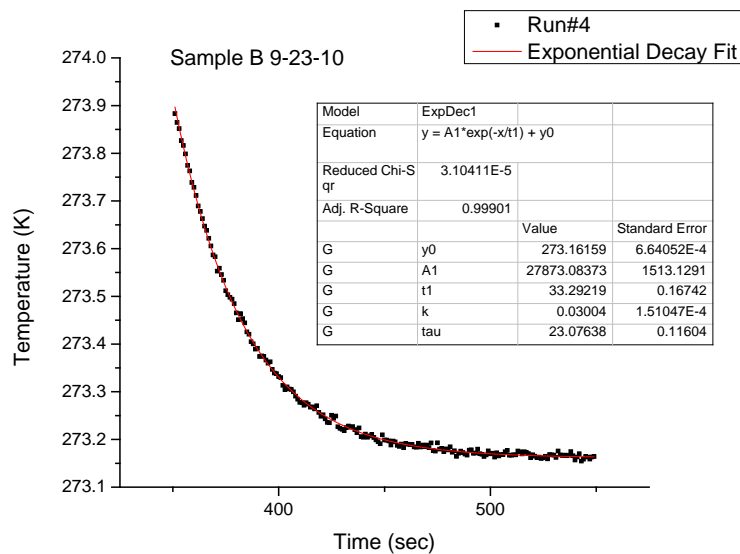
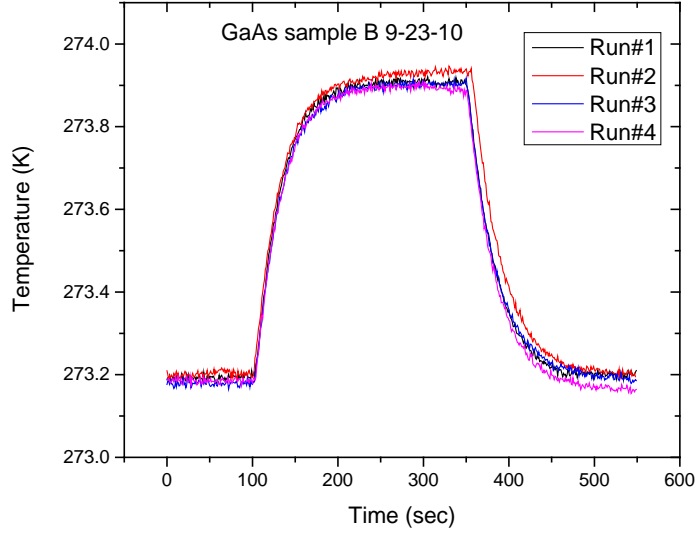
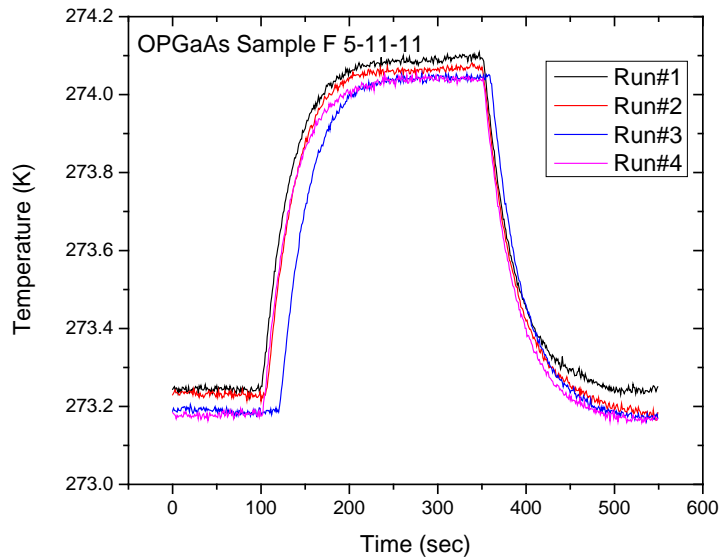


Figure 72: Sample B 9-23-10 Run#4 cooling curve is fitted to an exponential decay function.



**Figure 73:** Change in sample temperature throughout the calorimetry cycle for four different runs with similar configuration conducted on an unpatterned GaAs sample. The change in temperature for this sample is higher so the signal is much stronger than the noise.



**Figure 74:** Change in sample temperature throughout the calorimetry cycle for four different runs with similar configuration on an intentionally Si doped OPGaAs sample.



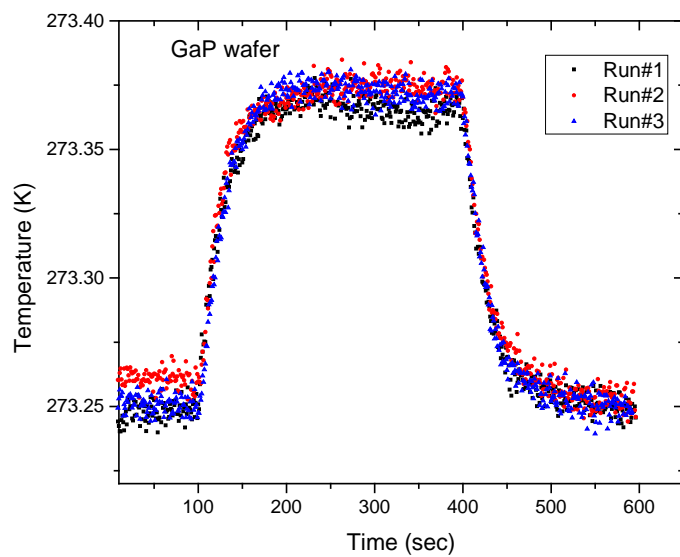


**Figure 75:** Change in sample temperature throughout the calorimetry cycle for three different runs with similar configuration on a commercially bought GaP wafer.

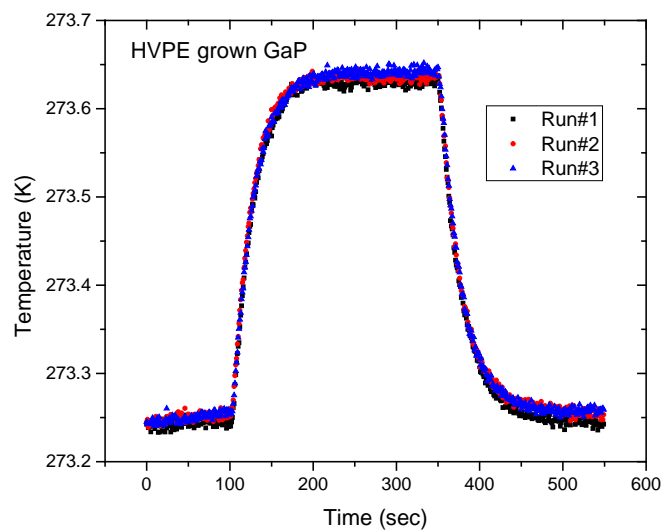


**Figure 76:** Change in sample temperature throughout the calorimetry cycle for three different runs with similar configuration on an AFRL HVPE grown GaP sample.

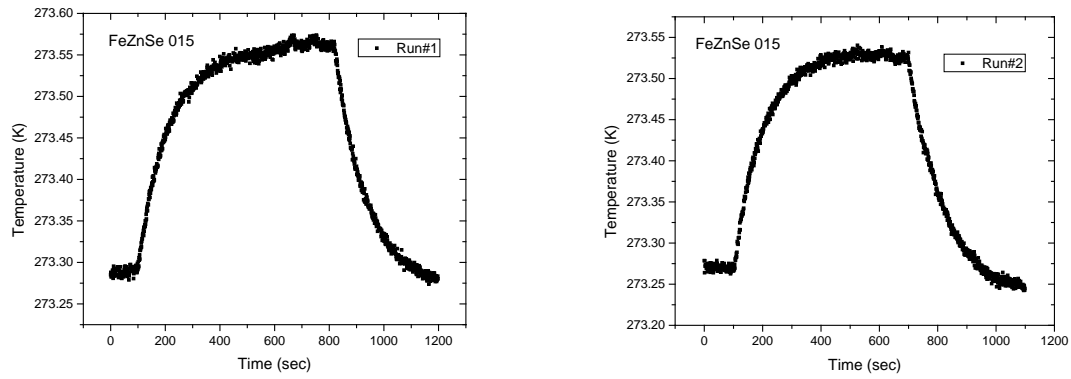


**Figure 77:** Change in sample temperature throughout the calorimetry cycle for two different runs on an  $\text{Fe}^{2+}$  doped ZnSe sample. Free carrier concentration in the sample was  $4.6 \cdot 10^{18} \text{ cm}^{-3}$ . The plots are separated because the time scale was varied between the runs to ensure that the sample saturated before the laser was turned off.

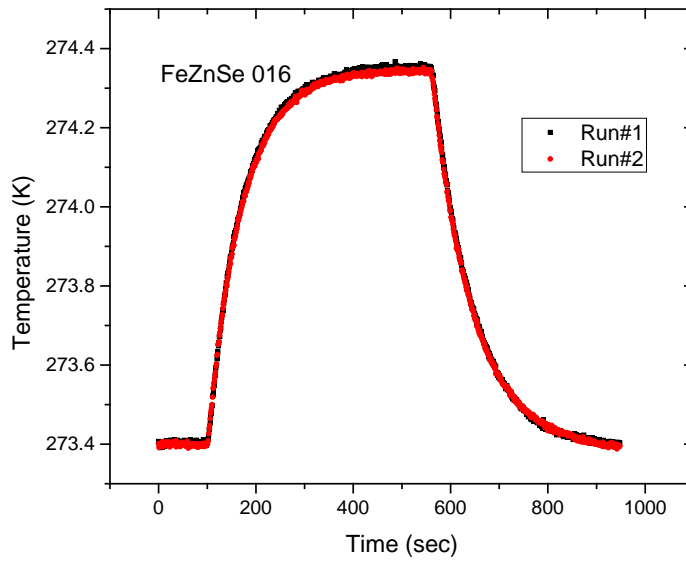


**Figure 78:** Change in sample temperature throughout the calorimetry cycle for two different runs with similar configuration on a  $\text{Fe}^{2+}$  doped ZnSe sample. Free carrier concentration in the sample was  $8.3 \cdot 10^{18} \text{ cm}^{-3}$ .

## **Appendix B**

### **Laser Calorimetry Experimental Setup Instructions (Do's and Don'ts)**

Before starting the calorimetry measurement, the sample should be cleaned thoroughly using acetone to reduce any additional surface reflection and to minimize surface absorption. As shown before in Chapter III, a nylon string is then taken and one of the tip is slightly dipped in Rubber-Cement. The best adhesive for use in this situation was found by conducting an experiment in which multiple candidates (school glue, nail polish, Duco-Cement and Rubber-Cement) were tested. The thermocouples were attached to a GaAs wafer sample and then the sample was picked up to increase the temperature of the sample which was displayed on the multimeter. The adhesive with the most accurate temperature reading was Rubber-Cement. Precaution should be taken to add only a slight amount of adhesive to the string to diminish any unnecessary thermal mass increase. The adhesive end of the string is glued to the face of the sample and left to dry for about five minutes. Then the string is carefully picked up and attached to the sample holder using a small piece of tape such that, the sample is hanging freely between the two nylon bottom strings of the sample holder. These guide strings at the bottom make certain that the sample face is perpendicular to the incident laser light. A similar process has to be repeated to attach a reference sample to the reference sample holder inside the calorimeter box.

After both the samples have been connected to the sample holders, the respective thermocouples are placed on the samples by sticking them in between the sample and the guide string. This type of thermocouple attachment negates the need of using any more

adhesives and hence reduces additional thermal mass. Then the laser is aligned onto the sample center and away from the thermocouple to complete the sample mounting and aligning part of the experiment. The lid is then placed on the box and the setup is left alone for about 45 minutes to let the inside temperature normalize. While waiting for the normalization part, the multimeter and the computer are fired up. The Keithley multimeter default preset ('K Type') of the type of sensor used, needs to be changed (by going into the menu and clicking the 'DMM Config' button) to the 'Type E' thermocouple we are using every time the multimeter is powered on. Depending on the mass of the sample to be measured, the ExcelLinx software will have to be setup for a run long enough so that the user has enough time to accommodate the saturation phase and the cooling phase. This can be easily set by using the 'DMS Scan' sheet of the software to change the 'Reading Count' to the desired run-time with a one second 'Timer'. The particular run we desire can be started by clicking on the drop down menu of 'Status/Cmds' button located on the same sheet and picking the 'Start/Collect' option. If there are no errors, the status changes to 'Collecting Data'. Then clicking on the associated sheet where the data is being collected shows the temperature and time being recorded in real-time. The laser then needs to be turned on manually for the required amount of time it takes to saturate the sample. After the software has stopped recording , multiple runs can be performed to ensure consistency. The alignment can also be check between runs by lifting the lid and waiting for then waiting for the appropriate time for temperature normalization.

### ***Minimizing Noise***

System noise is the limiting factor in laser calorimetry experiment. Chapter IV included some discussion and an experimental result (Figure 30) illustrating that the system temperature fluctuations were about 40 mK. This is the absolute minimum noise of the setup and limits any temperature measurements lower than 40 mK. As shown previously with the low loss OPGaAs sample, when the signal (or absolute change in temperature) is not big enough for pure samples, the noise makes it difficult to measure the decay constant and absolute change in sample temperature accurately. This induces a larger than usual uncertainty in the calculated absorption coefficient. As mentioned in the setup instructions above, special care should be taken to not induce any additional noise. Better contact between the sample and the thermocouple can give us a stronger signal. Replacing the current thermocouple with a more sensitive one can also provide higher accuracy in measurements.

### ***Thermal Camera Images for a Different Sample Holder Configuration***

A different sample holder configuration was used before arriving at the present setup. The previous configuration entailed applying excessive adhesive (Rubber-Cement) to the back face of the sample and attaching it to the guide strings. To check the temperature stability across the sample a RAZiR camera (made by GuideIR) was used to take images of the sample in all three stages (before, during and after the laser was turned on). Figures 79 thru 81 show these three stages. Although, the line profile across the samples shows good consistency, indicating somewhat identical temperature distribution, the extra thermal mass of the adhesive presented a problem. The images revealed that the adhesive was (more than the sample) consuming the heat intended for the sample and

thus making the measurements erroneous. Hence, the current setup was adopted with a goal to minimize the adhesive use.

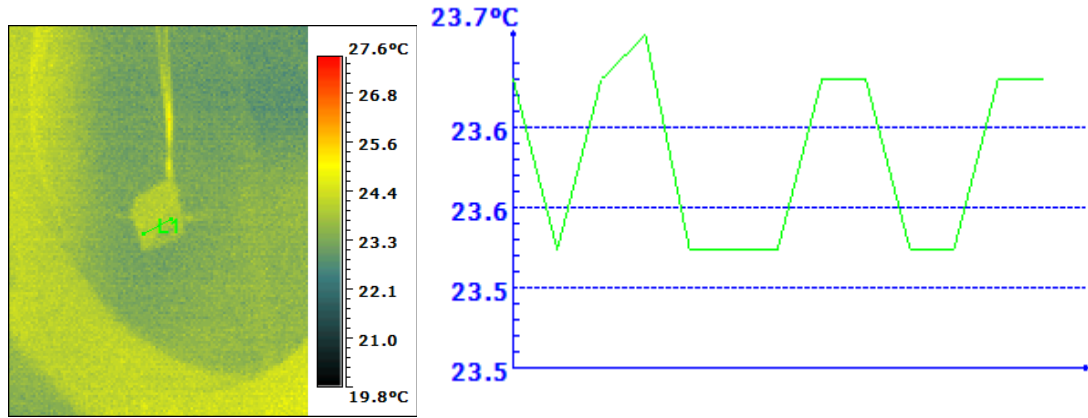


**Figure 79: Thermal image of a lossy unpolished OPGaAs sample glued to a string with a thermocouple attached to it from above. The line profile, L1 (right) is the temperature change across the sample, with a line average of 23.7°C. The image was taken before the laser was started.**

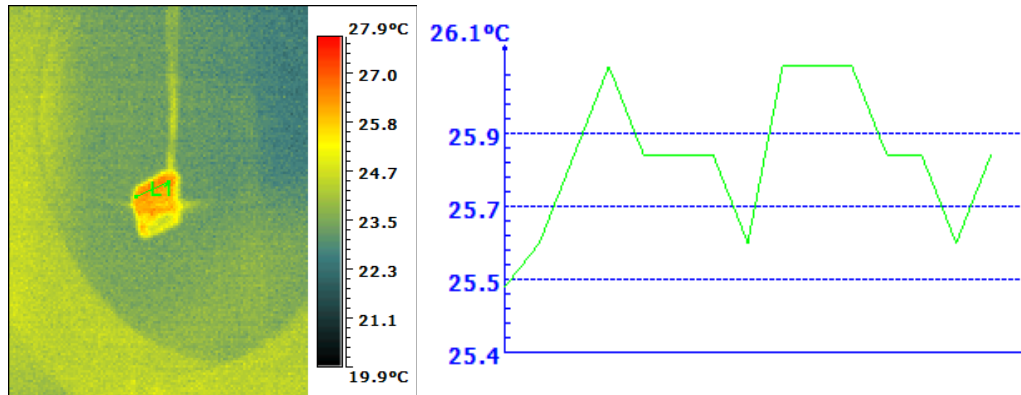


**Figure 80: Thermal image of a lossy unpolished OPGaAs sample during laser saturation stage. The line average temperature is 25.8°C. The bright red part of the sample is the adhesive radiating heat intended for the sample.**

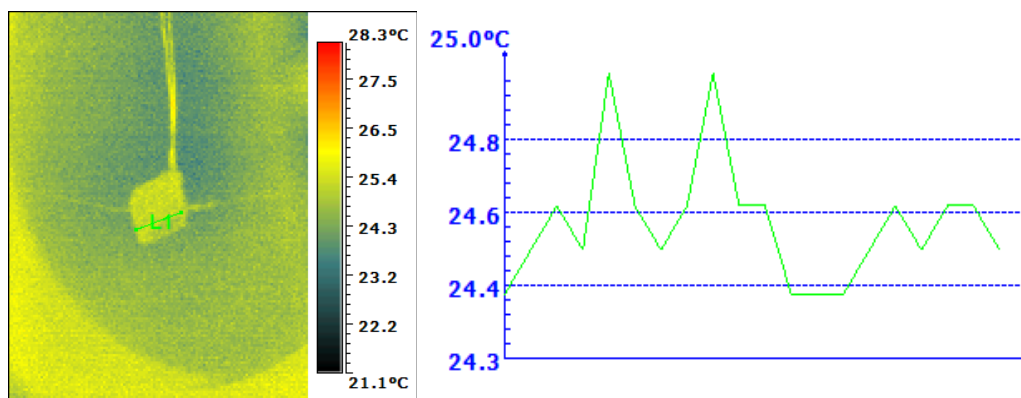


**Figure 81: Thermal image of a lossy unpolished OPGaAs sample after the laser was turned off. The line average temperature is 24.7°C.**

## References

- [1] Titterton, David H. "Requirements for Laser Devices used in Countermeasure Applications," *Proceedings of Technologies for Optical Countermeasures*. 598907-14. Bruges, Belgium: International Society for Optics and Photonics, 2005.
- [2] Kovalchuk, EV, Dekorsy, D., Lvovsky, AI, Braxmaier, C., Mlynek, J., Peters, A. and Schiller, S. "High-resolution Doppler-free molecular spectroscopy with a continuous-wave optical parametric oscillator," *Optics Letters*, 26: 1430-1432 (September 2001).
- [3] Elder, Ian. "Performance Requirements for Countermeasures Lasers," *Proceedings of SPIE Technologies for Optical Countermeasure*. 783605-14. Toulouse, France: SPIE Press, 2010.
- [4] Titterton, David H., "A Review of the Development of Optical Countermeasures," *Proceedings of European Symposium on Optics and Photonics for Defence and Security*. 1-15. London, United Kingdom: International Society for Optics and Photonics, 2004.
- [5] Sticht, Doug. "Electro-Optics and IR," *Atmospheric Transmission in Electronic Warfare and Radar Systems* (1992). 5 November 2013.  
<http://web.archive.org/web/20010913094914/http://ewhdbks.mugu.navy.mil/transmit.gif>.
- [6] Meyer, Joshua. *Optical Characterization of Thick Growth Orientation-Patterned Gallium Arsenide*. MS Thesis, AFIT/GAP/ENP/06-10. Graduate School of Engineering and Management, Air Force Institute of Technology (AU), Wright-Patterson AFB OH, March 2006 (ADA450196).
- [7] Godard, Antoine. "Infrared (2–12  $\mu\text{m}$ ) Solid-State Laser Sources: a Review," *Comptes Rendus Physique*, 8: 1100-1128 (December 2007).
- [8] Schunemann, Peter G., Pomeranz, Leonard A., Young, York E., Mohnkern, Lee and Vera, Alice. "Recent Advances in all-Epitaxial Growth and Properties of Orientation-Patterned Gallium Arsenide (OP-GaAs)," in *Conference on Lasers and Electro-Optics*. CWJ5. Baltimore, MY: Optical Society of America, 2009.
- [9] Mason, Paul D. and Michaille, Laurent F. "Review of the Development of Nonlinear Materials for Mid-IR Generation," in *SPIE Europe Security and Defence*. 71150N-10. Wales, United Kingdom: International Society for Optics and Photonics, 2008.
- [10] "Infrared Nonlinear  $\text{AgGaS}_2$ ,  $\text{AgGaSe}_2$ ,  $\text{GaSe}$ ,  $\text{ZnGeP}_2$  Crystals," *Nonlinear Materials* (2013). 5 November 2013.



<http://eksmaoptics.com/nonlinear-and-laser-crystals/nonlinear-crystals/infrared-nonlinear-aggas2-aggase2-gase-zngep2-crystals/>.

- [11] Schunemann, Peter. "Advances in NLO crystals for infrared parametric sources," *IR sources* (2007). 12 December 2013.  
<http://hathor.onera.fr/jso/opo-2007/pdfs/OPO-IR-ONERA2007-Schunemann.pdf>.
- [12] Snure, M., Jiménez, J., Hortelano, V., Swider, S., Mann, M., Tassev, V., Lynch, C. and Bliss, D. "Impurity Incorporation in Orientation Patterned GaAs Grown by Low Pressure HVPE," *Journal of Crystal Growth*, 352: 258-261 (August 2012).
- [13] Martínez, O., Avella, M., Angulo, H., Jiménez, J., Lynch, C. and Bliss, D. "Properties of Orientation-Patterned GaAs Crystals Studied by Cathodoluminescence Spectroscopy," *Superlattices and Microstructures*, 45: 337-342 (May 2009).
- [14] Faye, D., Grisard, A., Lallier, E., Gérard, B., Avella, M. and Jimenez, J. "Distribution of Point Defects in Orientation-Patterned GaAs Crystals: A cathodoluminescence Study," *Applied Physics Letters*, 93: 151115-3 (October 2008).
- [15] Zens, Timothy. *3-12  $\mu$ m Multi-Spectral Infrared Detector Arrays*. PhD dissertation. Massachusetts Institute of Technology, Cambridge MA, 2011.
- [16] Hordvik, A. "Measurement Techniques for Small Absorption Coefficients: Recent Advances," *Applied Optics*: 2827-2833 (November 1977).
- [17] Li, Bincheng and Welsch, Eberhard. "Configuration Optimization and Sensitivity Comparison among Thermal Lens, Photothermal Deflection, and Interference Detection Techniques," in *Laser-Induced Damage in Optical Materials*. 594-603. Boulder CO: International Society for Optics and Photonics, 1999.
- [18] Power, Joan F. "Pulsed Mode Thermal Lens Effect Detection in the Near Field via Thermally Induced Probe Beam Spatial Phase Modulation: a Theory," *Applied Optics*, 29: 52-63 (January 1990).
- [19] Draggo, Vaughn G., Morton, Richard G., Sawicki, Richard H. and Bissinger, Horst D. "Optical Coating Absorption Measurement for High Power Laser System," *Optical Absorption Measurement System*, 622:186-190 (January 1986).
- [20] Haiyang, Hu, Zhengxiu, Fan and Ye, Liu. "Measuring Weak Absorptance of Thin Film Coatings by Surface Thermal Lensing Technique," *Laser Physics-Lawrence*, 10: 633-639 (November 2000).

- [21] Martin, S., Bock, S., Welsch, Eberhard and Blaschke, Holger. "Optical Measurement of UV Absorption in Dielectric Coatings," in *Laser-Induced Damage in Optical Materials*. 93-101. Boulder CO: International Society for Optics and Photonics, 2001.
- [22] Boyd, Robert W. *Nonlinear Optics*. Burlington, MA: Elsevier, 2008.
- [23] Tassev, Vladimir, Bliss, David, Lynch, Candace, Yapp, Calvin, Goodhue, William and Termkoa, Krongtip. "Low Pressure–Temperature–Gas Flow HVPE Growth of GaP for Nonlinear Optical Frequency Conversion Devices," *Journal of Crystal Growth*, 312: 1146-1149 (April 2010).
- [24] Yariv, Amnon and Yeh, Pochi. *Optical Waves in Crystals*. New York: Wiley, 1984.
- [25] Feaver, Ryan, K. *Longwave-Infrared Optical Parametric Oscillator in Orientation Patterned Gallium Arsenide*. MS thesis. University of Dayton, Dayton OH, December 2011.
- [26] Skauli, T., Kuo, PS, Vodopyanov, KL, Pinguet, TJ, Levi, O., Eyres, LA, Harris, JS, Fejer, MM, Gerard, B. and Becouarn, L. "Improved Dispersion Relations for GaAs and Applications to Nonlinear Optics," *Journal of Applied Physics*, 94: 6447-6455 (October 2003).
- [27] Bass, Michael and others. *Handbook of Optics, volume IV: Optical Properties of Materials, Nonlinear Optics, Quantum Optics* (1st Edition). New York: McGraw Hill Professional, 2000.
- [28] Harm, Michael D. *Development of a Tm:Ho:YLF-Laser-Pumped Orientation-Patterned Gallium Arsenide Optical Parametric Oscillator*. MS thesis, AFIT/GEO/ENP/02-01. Graduate School of Engineering and Management, Air Force Institute of Technology (AU), Wright-Patterson AFB OH, March 2002 (ADA407867).
- [29] Faye, D., Lallier, E., Grisard, A., Gérard, B. and Gil-Lafon, E. "HVPE-Based Orientation-Patterned GaAs: Added-Value for Non-Linear Applications," in *Proceedings of Materials Research Society*. 799. Cambridge University Press, 2003.
- [30] Yu, Xiaojun. *MBE Growth of III-V Materials with Orientation-Patterned Structures for Nonlinear Optics*. PhD dissertation. Stanford University, Stanford CA, 2006.

- [31] Ebert, Christopher B., Eyres, Loren A., Fejer, Martin M. and Harris Jr, James S. "MBE Growth of Antiphase GaAs Films using GaAs/Ge/GaAs Heteroepitaxy," *Journal of Crystal Growth*, 201: 187-193 (May 1999).
- [32] Eyres, Loren A., Ebert, Christopher B., Fejer, Martin M. and Harris Jr, James S. "MBE Growth of Laterally Antiphase-Patterned GaAs Films using Thin Ge Layers for Waveguide Mixing," in *Lasers and Electro-Optics*. 276. New York: IEEE Press, 1998.
- [33] Orchard, David A., Mason, Paul D., McBrearty, Euan J. and Lewis, Keith L. "Laser Calorimetry as a Tool for the Optimization of Mid-Infrared OPO Materials," in *XXXV Annual Symposium on Optical Materials for High Power Lasers*. 379-387. Boulder CO: International Society for Optics and Photonics, 2004.
- [34] Turri, Giorgio, Chen, Ying, Bass, Michael, Orchard, David, Butler, James E., Magana, Sally, Feygelson, Tatyana, Thiel, Derrick, Fourspring, Kevin and Dewees, Randle V. "Optical Absorption, Depolarization, and Scatter of Epitaxial Single-Crystal Chemical-Vapor-Deposited Diamond at 1.064  $\mu\text{m}$ ," *Optical Engineering*, 46: 64002-10 (June 2007).
- [35] Willamowski, Uwe, Ristau, Detlev and Welsch, Eberhard. "Measuring the Absolute Absorptance of Optical Laser Components," *Applied Optics*, 37: 8362-8370 (December 1998).
- [36] Hecht, Eugene. *Optics*. New Jersey: Pearson Education, Inc., 2002.
- [37] Marciniak, Michael. "Spectrally Tunable, Fully Stokes Polarimetric and Fully Angular-Dependent Characterization," Report to Department of Engineering Physics, Air Force Institute of Technology, WPAFB OH, April 2013.
- [38] Nave, Carl. "Normal Reflection Coefficient," *Fresnel Reflection Coefficient* (2012). 12 January 2013. <http://hyperphysics.phy-astr.gsu.edu/hbase/phyopt/reflco.html>.
- [39] Teich, Malvin C. and Saleh, BEA. *Fundamentals of Photonics*. Canada: Wiley Interscience, 1991.
- [40] Schubert, Fred, E. *History of Light Emitting Diodes*. New York: Cambridge University Press, 2006.
- [41] Spitzer, WG and Whelan, JM. "Infrared Absorption and Electron Effective Mass in n-type Gallium Arsenide," *Physical Review*, 114: 59, (April 1959).
- [42] Lamott, Robert B. *Analysis and Application of the Bi-Directional Scatter Distribution Function of Photonic Crystals*. MS thesis, AFIT/GEO/ENP/09-M01.

Graduate School of Engineering and Management, Air Force Institute of Technology (AU), Wright-Patterson AFB OH, March 2009 (ADA497009).

- [43] Herr, Nicholas C. *AFM-Patterned 2-D Thin-Film Photonic Crystal Analyzed by Complete Angle Scatter Instrument*. MS thesis, AFIT/GMS/ENP/10-M01. Graduate School of Engineering and Management, Air Force Institute of Technology (AU), Wright-Patterson AFB OH, March 2010 (ADA516752).
- [44] Radhakrishnan, P. "Photothermal Deflection Setup at ISP," *Photothermal Deflection* (2013). 10 January 2014.  
[http://photonics.cusat.edu/Research\\_PTD\\_Work%20at%20ISP.html](http://photonics.cusat.edu/Research_PTD_Work%20at%20ISP.html).
- [43] Shell, Scot A. *Optical Parametric Oscillation in Orientation-Patterned Gallium Arsenide*. MS thesis, AFIT/GMS/ENP/07-01. Graduate School of Engineering and Management, Air Force Institute of Technology (AU), Wright-Patterson AFB OH, March 2007 (ADA464811).

REPORT DOCUMENTATION PAGE				Form Approved OMB No. 074-0188	
<p>The public reporting burden for this collection of information is estimated to average 1 hour per response, including the time for reviewing instructions, searching existing data sources, gathering and maintaining the data needed, and completing and reviewing the collection of information. Send comments regarding this burden estimate or any other aspect of the collection of information, including suggestions for reducing this burden to Department of Defense, Washington Headquarters Services, Directorate for Information Operations and Reports (0704-0188), 1215 Jefferson Davis Highway, Suite 1204, Arlington, VA 22202-4302. Respondents should be aware that notwithstanding any other provision of law, no person shall be subject to a penalty for failing to comply with a collection of information if it does not display a currently valid OMB control number.</p> <p><b>PLEASE DO NOT RETURN YOUR FORM TO THE ABOVE ADDRESS.</b></p>					
1. REPORT DATE (DD-MM-YYYY) 27-03-2014		2. REPORT TYPE Master's Thesis		3. DATES COVERED (From – To) May 2012 – Mar 2014	
TITLE AND SUBTITLE  Characterizing Optical loss in Orientation Patterned III-V Materials using Laser Calorimetry				5a. CONTRACT NUMBER	
				5b. GRANT NUMBER	
				5c. PROGRAM ELEMENT NUMBER	
6. AUTHOR(S)  Sadhwani, Dushyant A., Second Lieutenant, USAF				5d. PROJECT NUMBER	
				5e. TASK NUMBER	
				5f. WORK UNIT NUMBER	
7. PERFORMING ORGANIZATION NAMES(S) AND ADDRESS(S) Air Force Institute of Technology Graduate School of Engineering and Management (AFIT/ENY) 2950 Hobson Way, Building 640 WPAFB OH 45433-8865				8. PERFORMING ORGANIZATION REPORT NUMBER  AFIT-ENP-14-M-32	
9. SPONSORING/MONITORING AGENCY NAME(S) AND ADDRESS(ES) Air Force Research Lab (SNJW) ATTN: Dr. Rita D. Peterson 2241 Avionics Circle, Building 620 WPAFB OH 45433 DSN: 785-9657 e-mail: Rita.Peterson@wpafb.af.mil				10. SPONSOR/MONITOR'S ACRONYM(S)  AFRL/SNJW \$ AFOSR	
				11. SPONSOR/MONITOR'S REPORT NUMBER(S)	
12. DISTRIBUTION/AVAILABILITY STATEMENT DISTRIBUTION STATEMENT A: APPROVED FOR PUBLIC RELEASE; DISTRIBUTION UNLIMITED.					
13. SUPPLEMENTARY NOTES This material is declared a work of the U.S. Government and is not subject to copyright protection in the United States.					
14. ABSTRACT This research examines the optical loss in orientation patterned III-V materials. Laser calorimetry technique was assembled to measure the absorption loss in GaAs, GaP and Fe <sup>2+</sup> ZnSe samples. Three different methods are explained and utilized to calculate the absorptance value from the calorimetry data. Absorption coefficient values were found for three different samples of GaAs ranging from 0.025±0.009 cm <sup>-1</sup> to 0.80±0.08 cm <sup>-1</sup> , all within the sphere of published values for GaAs. A Complete Angle Scatter Instrument (CASI) was used to determine scatter at incident angles ranging from 0 to 55.5 degrees from two OPGaAs samples using an 8.16 µm, p-polarized incident laser light. Diffraction peaks were observed in the samples with high impurities, with domains in the material acting as diffraction gratings. FTIR measurements were conducted using a wire grid polarizer on the CASI samples to investigate transmission signal variations with change in incident polarization. Both patterned GaAs samples exhibited some polarization effect from the grating material. The amount of transmission detected changed by as much as 20% for both samples as they were rotated to change incident polarization.					
15. SUBJECT TERMS Laser calorimetry, optical loss, absorption coefficient, polarization dependent loss, diffraction from domains of gallium arsenide					
16. SECURITY CLASSIFICATION OF:			17. LIMITATION OF OF ABSTRACT  UU	18. NUMBER OF PAGES  117	19a. NAME OF RESPONSIBLE PERSON Maj. Timothy Zens, AFIT/ENP
a. REPORT  U	b. ABSTRACT  U	c. THIS PAGE  U			19b. TELEPHONE NUMBER (937)-255-3636 Timothy.Zens@afit.edu